Non-linear and non-stationary hydroclimate variability in France and the Euro-Atlantic area

Manuel Fossa

Normandie Université

THESE

Pour obtenir le diplôme de doctorat

Spécialité Sciences de l'Univers

Préparée au sein de l'Université de Rouen

Non-linear and non-stationary hydroclimate variability in France and the Euro-Atlantic area

Présentée et soutenue par
Manuel FOSSA

Thèse soutenue publiquement le (date de soutenance) devant le jury composé de		
David HANNAH	Professor / GEES / University of Birmingham	Rapporteur
Benoit HINGRAY	Chargé de Recherches HDR / IGE / Université de Grenoble	Rapporteur
Michael GHIL	Distinguished Professor / TCL / University of California	Rapporteur
Laurie CAILLOUET	Ingénieure / hydrométéorologue / Compagnie Nationale du Rhône	Examinatrice
Monica IONITA	Research Scientist / Paleo-climate Dynamics / Alfred Wegener Institute	Examinatrice
Nicolas MASSEI	Professeur / M2C/ Université de Rouen Normandie	Directeur de Thèse
Benoit LAIGNEL	Professeur / M2C/ Université de Rouen Normandie	Co-Directeur de Thèse
Matthieu FOURNIER	Maitre de conférences HDR / M2C / Université de Rouen Normandie	Co-Encadrant de Thèse
Claire MAGAND	Chargée de Projet / Office Français pour la Biodiversité	Membre Invitée
Bastien Dieppois	Assistant Professor / CAWR / University of Coventry	Membre Invité

Thèse dirigée par Nicolas MASSEI laboratoire UMR 6143 Morphodynamique Continentale et Côtière

UNIVERSITÉ DE ROUEN NORMANDIE

ED 497 NBISE
Normande de Biologie Intégrative, Santé, Environnement

M2C

AVANT-PROPOS

Cette thèse, réalisée au sein du laboratoire M2C de l'université de Rouen et en cofinancement avec l'Office Français pour la Biodiversité, a bénéficié du financement de la Région Normandie, avec l'appui de la fédération FR3130 SCALE.

Acknowledgements

この論文は、私の母、亡くなった父（毎日欠場する）、そして私の家族や大切な友人に捧げられています。本当に旅行でした,この論文は.最初は速く走りましたが、その後、落ちました.

しかし、私の友人と家族はいつも私を助けてくれました.彼の無限のサポートのために,最初に Nicolas Massei に感謝したい.彼はつらい時でもいつも私を支えてくれました. この男はまだ私が見ているモデルであり、真の科学者です.Nicolas,ありがとう！ 私のもう一人の友人、Bastien Dieppoisに感謝したい. 彼がいなければ、私はこの論文を完成させなかっただろう. 彼の上司は、私を助けてはいけないと言ったが、彼は私と一緒に一日中過ごした。Bastien先輩,心から感謝します！別の非常に重要な人物はKenneth Stephensonさんです.彼がいなければ、私はこのExtremal lengthに取り組むことができなかっただろう.これは私に全く新しい世界を開いた.ありがとう,Stephensonさん!MatthieuとBenoitのサポートに感謝します. Criannのすばらしいサービスに感謝します.Gill MorelとCharles Feibel、私の奇妙な要求に我慢してくれてありがとう! クロススケール相互作用アルゴリズムで私をサポートしてくれたNicola Jajcayにも感謝します.

Claire Magand、私の遅れた仕事に我慢してくれてありがとう,ごめんなさい!

M2Cは家族のようなものです。たくさんの素晴らしい友達に会いました！これらの絆は確かに私たちが苦難に耐えることを助けました, そして私たちのジョークは私たちの記憶に永遠にとどまるでしょう.　私たちは悲しいことについても冗談を言うために使用します.例えば,Jewとtata,BiatchとChoucroutyとAbdel, Flaviereの疲れる屋外キャンペーン. 良いことがたくさんありました: Lycaonsのお尻をなめるとか, 「Président Voleur!」の歌とか, 「Le masque de faire」についてのジョークとか,crossfit girlとMarthe,Clef à moletteと私のFort de caféなContrition,等々…

たくさんの笑いがありました! だから, Jew,Biatch,Clef à Molette,Choucrouty,Louise,Flavière,Senpai,Doudou,Connasse,David,Ruth,Thomas,Antonin,Valentin,Léo,Micheeeeeeeeeeeellllllll,Max,Yoann,Theo,M2Cの科学者、MoussMouss, Maria, Cécile…S

また、STEその後ESEBのクラスメートにも感謝したいと思います,あなたは私を10歳若く感じさせました！だから, Doudou, Laurent, Mathije, Zou des bois, Natacha, Julie, Marion, DoudouのMarion, Tite Aurore, Raph,…. Kathleen, Marie “wild” Lenoir, 47%(冗談!冗談よ!愚痴の束!あなたを平手打ちしたかったねえ!)

みんな……

どうもありがとう!!

天国のJean-paul……….ouiiiiii…..bonnnnnn….effectivement…..みんなあなたに会いたがっている！

Table of contents

INTRODUCTION

1. Background

France is one of the wealthiest countries in Europe and is water-independent as far as water access is concerned (Richard et al. 2010). However, there are topics, pertaining to water resources, which are of significant concern in France. Despite the large supply of water, shortage periods regularly occur during summer, especially in southern France, due to exceeding exploitation (Richard et al. 2010). A large part of this exploitation is tied to energy production and irrigation, fluctuating depending on the needs (Colon et al. 2018). Natural hazards represent another variable source of concern (Richard et al. 2010).For instance, France has experienced significant drought and flood episodes during the last 20 years. The 1999 windstorms and floods caused 140 deaths over France, southern Germany, Switzerland and Italy, while the 2003 heatwaves, accompanied by severe droughts, caused the deaths of 14802 people (Boccard 2018). In the above mentioned example, the natural variability of the hydroclimate system proved to be unpredictable, so that management policies could not anticipate the fore coming issues, which had severe consequences, both on people and economy. A complete understanding of hydroclimate variability is indeed challenging. The hydrosphere is an integral part of the climate system and is in constant interaction with the atmosphere, lithosphere, cryosphere and biosphere (Gettelman and Rood 2016). Figure I.1a-b illustrates the different components impacting hydrological system, as well as their spatial and temporal scales. Any change in one of the compartment may affect the others (Kingston et al. 2020).

a)

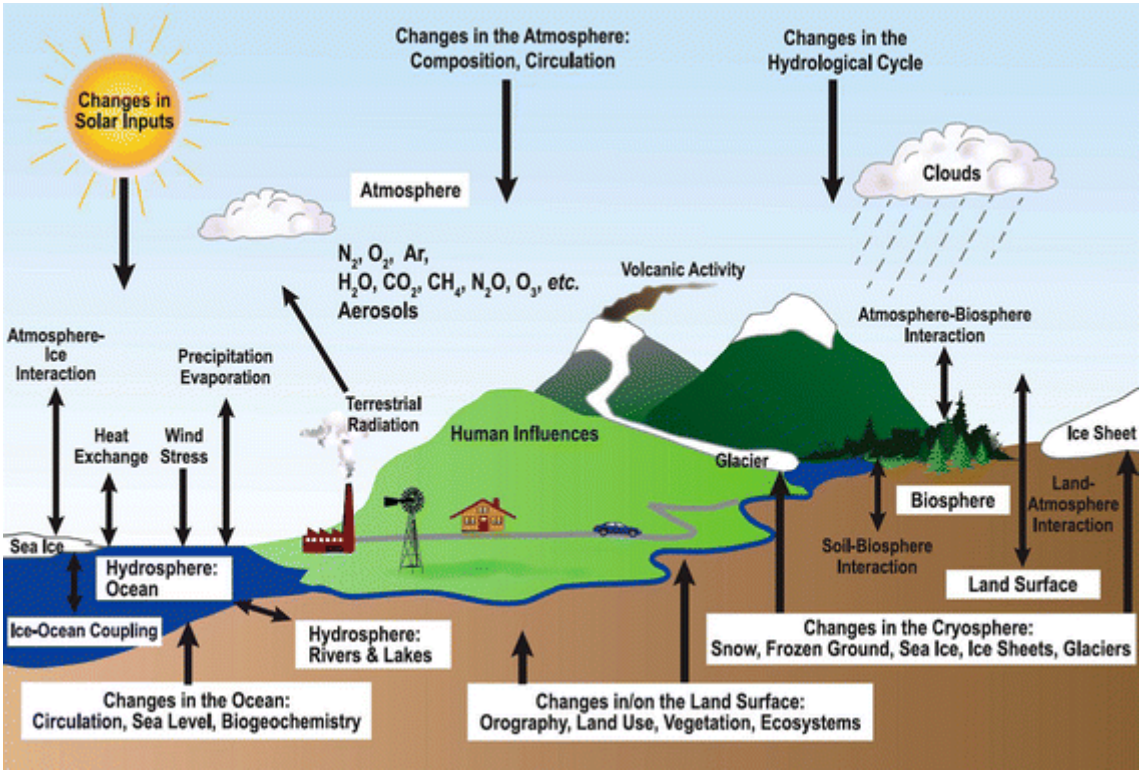

b)

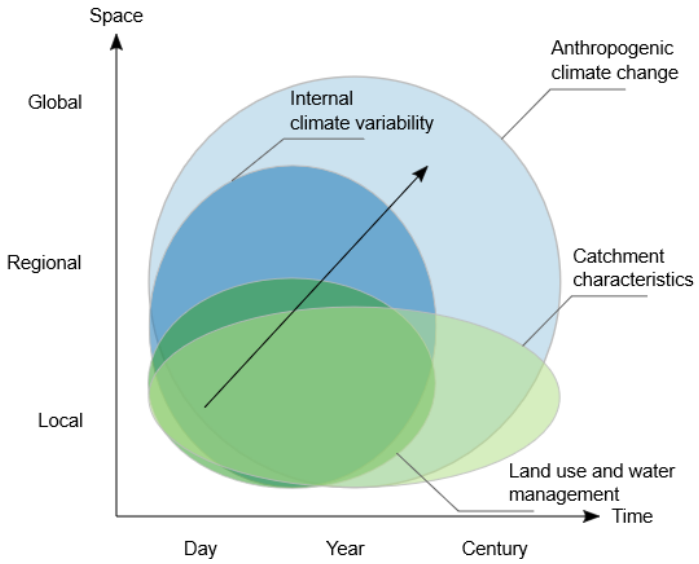

Figure I.1. The spatial and time scales of the Hydroclimate system. *a) The different components of the hydroclimate system and their interactions; b) The spatial and temporal scales of hydroclimate variability. (IPCC 2007;Kingston et al. 2020)*

This results in high degrees of non-linearity, as well as non-stationarity, amplified by human activities, such as changes in land-use, demographic explosion, as well as rising temperature at the global scale in response to an increasing greenhouse release in the atmosphere (IPCC 2007). Even though an increasing number of studies focus on describing non-stationarity, very few link it to non-linearity, which leads to partial understanding of the complex hydroclimate dynamics (Blöschl et al. 2019). In addition, studies examining hydroclimate variability have been scarce in France, and often localized in time scale or space (Sauquet et al. 2008; Boé 2013; Boé and Habets 2014; Caillouet et al. 2016; Dieppois et al. 2016a). This leaves many questions as to how the non-linearity and non-stationarity shapes the temporal and spatial scales of hydrological variability (Blöschl et al. 2019).

2. Literature review

2.1. Hydrological variability in France

At the seasonal scale, discharge variability in France is spatially dependent on the rainfall and/or snowfall type defining the hydrological regime. North-western watersheds are driven by rainfall, with discharge peaking in winter while low discharge occurs in summer. Eastern and South-eastern watersheds are driven by snowfall (or by both rainfall and snowfall), with discharge peaking in spring (due to snow melt; Pardé 1933; Sauquet et al. 2008). Discharge in northern France have also been associated with significant annual, inter-annual (5-8 years' time scales) and decadal variability (Massei et al. 2010; Fritier et al. 2012; Dieppois et al. 2016). Long-term variability, *e.g.* at decadal scales, in discharge have been shown to be a very important in trends detection over France. For instance, positive trends were initially found in northern France regions, *i.e.* in rainfall-driven regions, while negative trends were identified in the southern and eastern regions, *i.e.* regions where discharge is at least partially impacted by snowmelt (Stahl et al. 2010). However, using multi-temporal trend analysis, Hannaford et al. (2013) demonstrated that these spatial dissimilarities were artefact results from decadal

variability. Accounting for decadal variability, Hannaford et al. (2013) identified positive trends in southern and eastern regions, while no significant trends were found in the northern regions.

The spatial homogeneity in discharge variability has been investigated at several time scales, on average, and in high- (flood) and low- (drought) flows. Results from previous studies vary greatly depending on the timescales. For instance, twelve regions were found by Sauquet et al. (2008) for monthly runoff, while, at decadal timescales, Hannaford et al. (2013) found five regions across Europe, where the stations in France represented only one region (Central west). According to Gudmundsson et al. (2011a), high, mean and low discharge also influences the spatial coherence. For instance, at spatial scales lower than 400 km, high-flows were found to be more homogeneous spatially than mean- and low-flows (Gudmundsson et al. 2011a). Reversely, when considering larger spatial scales, greater than 800 kilometres, low flows regions tend to become more homogeneously spatially distributed (Gudmundsson et al. 2011a). The possible reason behind this distinction is the different processes associated with high- and low-flows (Gudmundsson et al. 2011a): high-flow being tied to water input, while low-flows is tied to depletion of storage. Thus, focusing on flood event distribution, Mediero et al. (2015) found five homogenous regions across Europe, with France being characterized by three regions.

2.2 Drivers of discharge variability in France

Discharge is primarily impacted both by watershed characteristics, precipitation and evapotranspiration (mostly driven by temperature; Gudmundsson et al. 2011). While rainfall originated from large-scale climate/weather system beyond the catchment scale, effective precipitation, *i.e.* precipitation minus evapotranspiration, is then modulated by watershed characteristics, hence creating a complex, feedback driven, climate-to-discharge system (Boé 2013).

2.2.1 Watershed characteristics

Morphology of the catchment, soil types, evapotranspiration, land-use and groundwater support are examples of watershed characteristics, commonly associated with driving discharge variability. Three types of ground water support, with decreasing transfer types, are found in France, respectively named as: matrix, fractured matrix, and karstic. Depending on the location, either or both three types can be found, and this is deeply affecting how the precipitation input is transferred to discharge *via* groundwater support. For instance, in the Seine river watershed (northern France), karstic network communication with the fractured matrix have been shown to induce two flow regimes one as a conduit, and other as a storage, while their behavior was being controlled by the hydraulic gradient inside the matrix (El Janyani et al. 2012). According to Labat et al. (2000), the dynamics of the watershed groundwater support is thus catchment specific, non-linear and non-stationary. Such watershed properties were taken into account in previous classification of discharge variability in France by Sauquet et al. (2008). Through complex processes of surface saturation, soil properties variability also impacts the discharge variability in a non-linear way. This was, for instance, demonstrated in regions vulnerable to flash floods, where soil properties control the discharge until surface saturation occurs, after which rainfall becomes the primary driver (Anquetin et al. 2010).

2.2.2 Precipitation-watershed characteristics feedback

Soil moisture in France has been found to have significant impact on local precipitation (Boé 2013; Laaha et al. 2017). However, such feedback depends on the related large-scale climate pattern. As illustrated in Boé (2013), a negative feedback was observed during a negative North Atlantic Oscillation (NAO), while a positive feedback was observed during Atlantic Low conditions. With a higher- than-global temperature increase over France for the last 40

years, the relationship between precipitation, soil moisture and evapotranspiration is thus becoming crucial (OECD 2013).

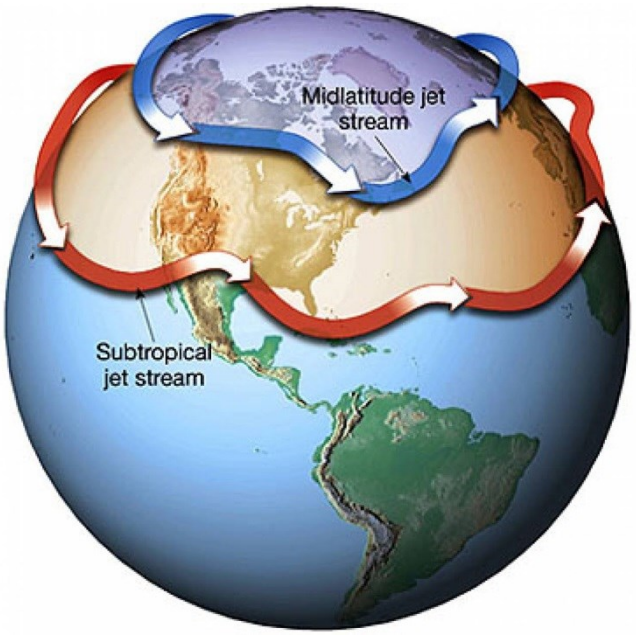

Figure I.2. Position of the polar and subtropical jet streams. *The high altitude jets blow eastward and delimit the zone (orange) of westerlies. (Taken from www.3bmeteo.com/).*

2.2.3 Large-scale climate

The large-scale atmospheric circulation, modulating precipitation and temperature, can be investigated through atmospheric pressure patterns. Under the geostrophic approximation, winds indeed flow parallel to isobar lines, with increasing velocity proportional to the gradient between isobar lines.

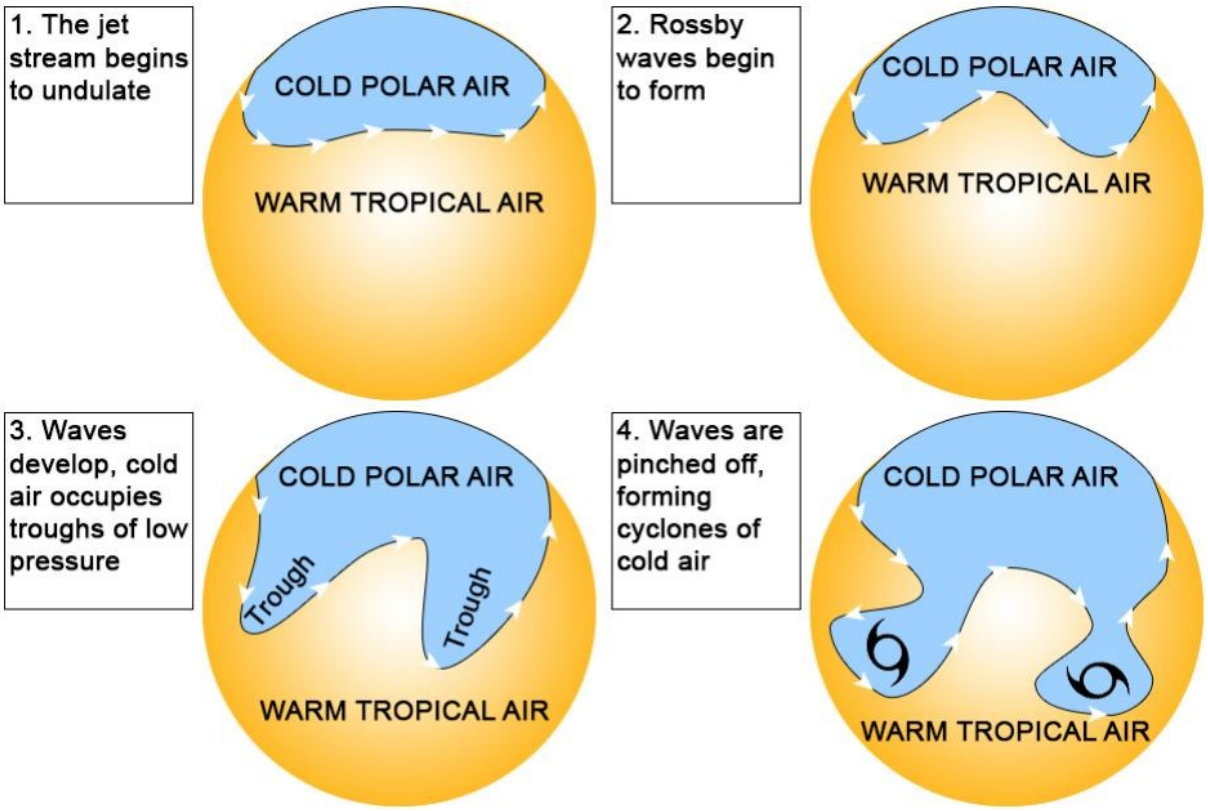

Figure I.3. Formation of the Rossby waves inside the polar jet stream. *1) The jet stream forms around the zone of maximum pressure gradient between the cold polar air, and the warm tropical air. As warm air is less dense than cold air at the same atmospheric pressure, temperature differences starts to form along isobaric lines, i.e. baroclinic situations develops, triggering deviation of the jet from a pure zonal motion. 2) Because the absolute vorticity is conserved, any poleward motion of the jet increases the planetary vorticity, while the relative vorticity decreases, yielding a southward motion. When the jet has reached a certain equatorward position, the situation reverses, relative vorticity increases, planetary vorticity decreases, and the jet has now a northward direction. This process is then repeated, yielding the Rossby waves. 3) Because of the alternate northward and southward motions, troughs become associated with cyclonic conditions, and ridges with anticyclonic conditions. 4) At one point, the wave structure breaks and some troughs get disconnected from the wave train, becoming storms. Source: www.abc.net.au*

2.2.3.1 North Atlantic atmospheric circulation

The North Atlantic is a major source of precipitation and temperature variability, due to the strong westerlies, carrying moisture and heat towards Europe (Ghil and Lucarini 2019).Those westerlies flowing from the high altitude at high speed are associated with the mid-latitude jet streams, mainly (Figure I.2). There is however another jet in the subtropical regions (Figure I.2), which is particularly important for the Mediterranean regions (Lionello et al. 2006). Both jets are due to the Coriolis force. The equator-pole differential heating induces an advection of heat from the equator to the poles, however, due to the Coriolis force (also called the planetary vorticity), this advection is progressively deviated clockwise in the Northern Hemisphere, yielding eastward winds.

The mid-latitude jet, which affects Europe climate the most (Ghil and Lucarini 2019) , arises from the high pressure gradient between the cold air from the pole encountering warm air coming from the equator (Ghil and Lucarini 2019), It has a wave-like structure in response to the strong zonal temperature gradients, which prompts deviation from a pure zonal advection (in addition to orography effects in some regions; Ghil and Lucarini 2019). As the absolute vorticity is preserved, there is a balance between the relative and planetary vorticities, leading to a wave-like pattern. These waves developing inside the jet stream are called Rossby waves (Figure I.3; Ghil and Lucarini 2019). Those waves propagate eastward with the jet stream, but may become stationary or stalled, yielding persistent weather conditions in regions below ridges or troughs (Ghil and Lucarini 2019; Mann 2019). Troughs of the Rossby wave eventually lump apart forming storms, that progress eastward too (Ghil and Lucarini 2019).

2.2.3.2 Weather patterns

Depending on the shape of the mid-latitude jet stream, *i.e.* the development and evolution of Rossby wave trains, three types of North Atlantic atmospheric patterns are commonly found

(Mo and Ghil 1987) zonal, blocking and wave train. Zonal patterns involve isobaric lines being orientated East/West leading to westerlies following a straight-line (Figure I.2). Blocking patterns are associated with a high pressure system blocking the jet stream, forcing it to deviate, forming a ridge and inducing dry conditions south of the ridge (Figure I.5). Wave train patterns are associated with successions of troughs and ridges, forming meridional winds (*i.e.* winds with significant poleward components), and yielding to persistent dry/wet weather when this system is stable, or to fast changing weather if the wave train is not stabled (Petoukhov et al. 2013). Depending on the time scales, those patterns may be observed directly (short term), or as anomalies (longer term; Cassou 2004; Hauser et al. 2015).

The NAO, and its positive and negative phases, have been observed since the early 20th century (Figure I.4a-b, I.5; Visbeck et al. 2001; Cassou et al. 2004; Hurrell and Deser 2014). The positive phase of the NAO triggers a zonal atmospheric circulation (Figure I.5). The negative phase however creates a blocking situation, responsible for the difference in weather found in France (Figure I.4). The dipole structure is not zonally symmetric, in the positive phase, the dipole is titled toward the East, and reversely for the negative phase (Figure I.4a-b; Visbeck et al. 2001; Cassou et al. 2004; Hurrell and Deser 2014).

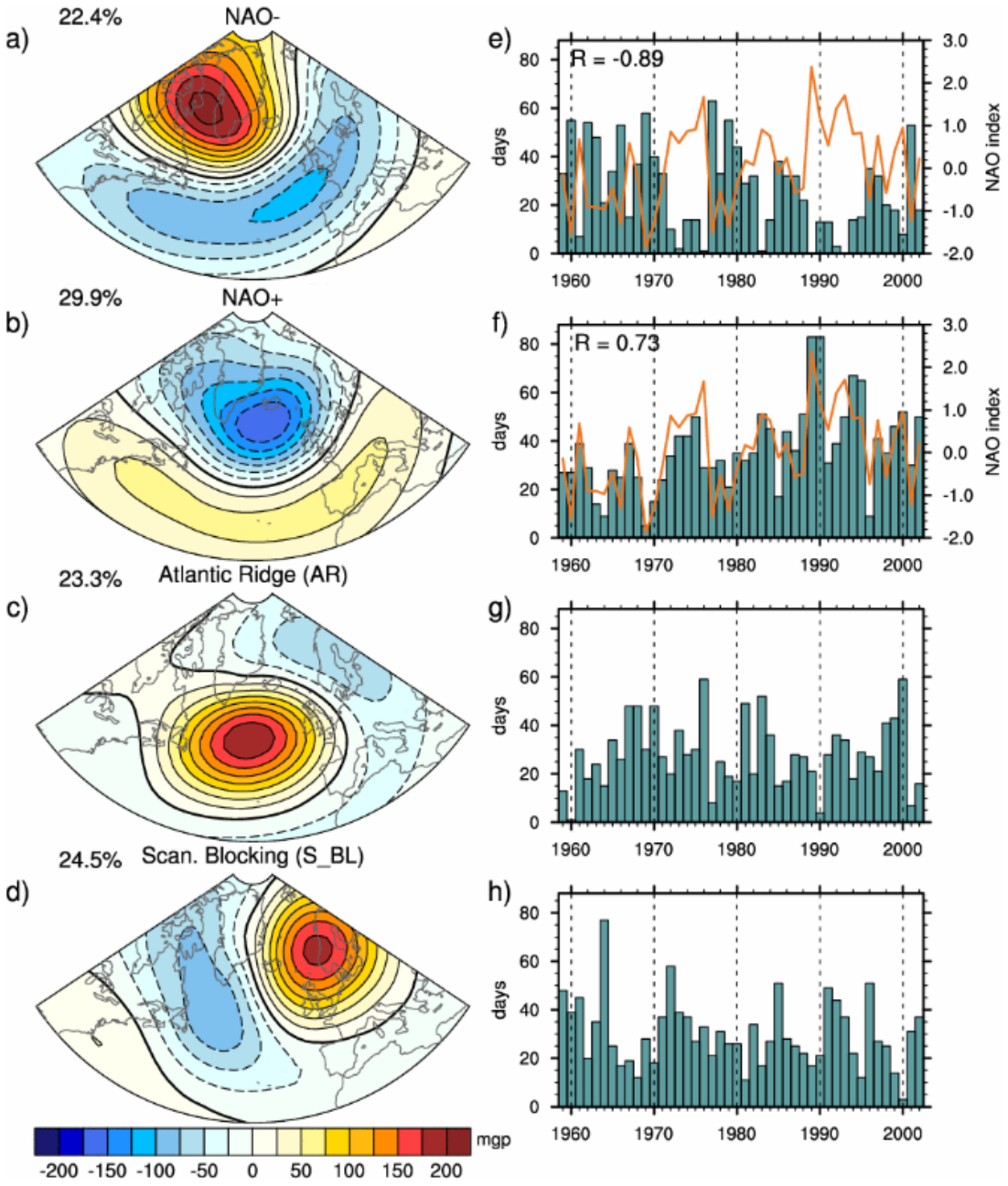

Figure I.4. Statistical weather patterns: *a-d) Pressure anomalies (in mgp) contours, isolines and frequency of occurrence (in %) associated with each statistical weather patterns; e-h) the number of days of occurrence per year (histogram) of each statistical weather patterns, compared to the NAO index (top panels, orange curves).*(Cassou 2010)

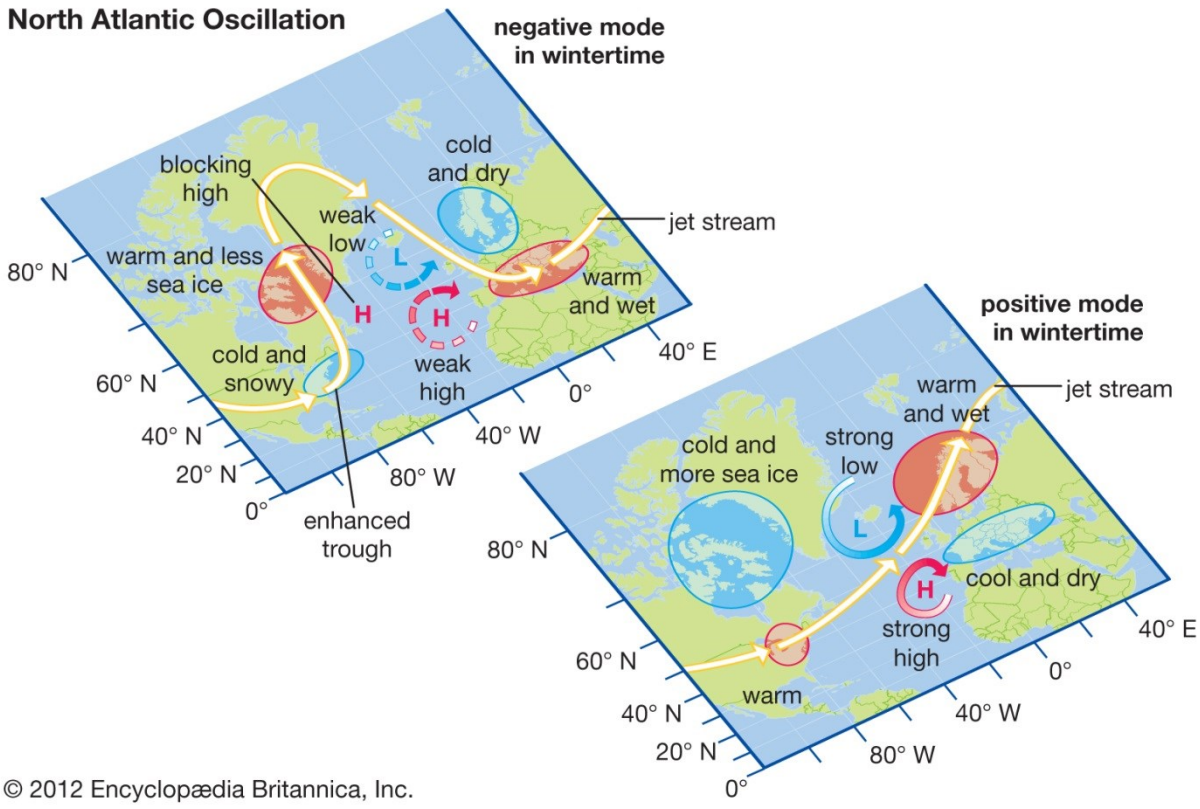

Figure I.5. Positive and negative phases of the North Atlantic Oscillation Encyclopaedia Britannica (2012). *The structure of the North Atlantic Oscillation is the Icelandic low and the Azores high dipole. In the positive phase (lower map), the Icelandic low is strong (i.e. very low pressure), while the Azores high is strong as well (i.e. very high pressure), the jet stream is channeled in between the dipole, resulting in warm and wet winters in Northern Europe, and cool and dry winters in Southern Europe. In the negative phase, the Icelandic low and Azores high are weak, so that overall the dipole disappears, creating a blocking condition in Mid North-Atlantic. The jet stream has to go around that blocking, triggering Rossby waves, and advection of warm air on the American side, and advection of cold air on the European side. In Northern Europe, the winters are cold and dry, in Southern Europe, they are warm and wet*

The link between the NAO and European hydroclimate is clearer in winter (Hurrell et al. 2003), but the NAO has an impact on European hydroclimate even in summer (Mares et al.

2002; Folland and Knight 2009; Bladé et al. 2011; Giuntoli et al. 2013). The relationship between the NAO and hydroclimate over France has been found at multiple timescale from seasonal to multi-decadal time scales (Fritier et al. 2012; Massei and Fournier 2012; Boé 2013; Boé and Habets 2014; Ullmann et al. 2014; Hermida et al. 2015; Dieppois et al. 2016a). This relationship also appears to be modulated by soil moisture (Bladé et al. 2012). The positive phase of the NAO has been dominant from the 1960s to the mid-1990s (Figure I.4f), and has been associated with higher than normal streamflow anomalies (Massei et al. 2010). It has also been to a North-eastward shift in storm tracks near Iceland and the Norwegian Sea (Hurrell and Van Loon 1997), and an increase of river flow in the North, and a decrease in the South of Europe (Shorthouse and Arnell 1997; Ullmann et al. 2014). We also note that the decadal and multi-decadal NAO variability has been increasing since the mid-19th century (Goodkin et al. 2008; Sun et al. 2015) with an associated increased variability of precipitation and streamflow over France (Dieppois et al. 2016a).

The relationship between NAO and hydroclimate depends greatly on the region and the time scale. For instance, even in Northern France, where significant links were found at decadal time scales (Massei and Fournier 2012), the links between hydroclimate variability and NAO, depends on the location (Dieppois et al. 2013). In the Mediterranean, clear links between hydroclimate and the NAO occur at the quasi-decadal time scales (Feliks et al. 2010), but at the monthly time scales, different rainfall patterns are linked to either phase of the NAO, or other weather patterns (Ullmann et al. 2014).

In addition to the NAO, two blocking patterns are also frequently associated with weather in Europe (Cassou 2004). The Atlantic ridge (AR) is characterized by a high pressure system over North Atlantic, just south of Greenland (Figure I.4c). AR patterns are associated with cold, but rainier weather over France, especially in the North (Boé 2013). Since 2001, there has been an increase of the frequency of blocking patterns, which are becoming prominent

compared to the NAO regimes (Hurrell and Deser 2009; Hauser et al. 2015; Hanna et al. 2016). The Scandinavian blocking (SBL) is a large high pressure centre over Scandinavia (Figure I.4d), which brings cold air over Central Europe, and can potentially migrates westward towards France (Cassou 2010; van der Wiel et al. 2019).

2.2.4 Ocean-hydroclimate variability interactions

The North Atlantic atmospheric circulation variability has been shown to significantly interact with North Atlantic sea surface temperature (SST) from monthly to multi-decadal time scales. At monthly timescale, the preferred direction of the interactions is from the atmosphere to the SST. A positive NAO is followed by positive SST anomalies in the western subtropical North Atlantic and negative SST anomalies in the subpolar gyre and off the eastern coast of North Africa, referred to as the SST ‘‘tripole’’, and reversely during a negative NAO (Kushnir et al. 2002)However, In early winter, the NAO also responds to slightly different tripolar SST anomalies, amplifying the NAO and acting as a positive feedback (Czaja and Frankignoul 1999, 2002; Gastineau and Frankignoul 2014). Whether such active ocean–atmosphere coupling has a significant influence on decadal climate variability has been mostly investigated using climate models. Two-way ocean–atmosphere interactions in the North Atlantic can be the dominant players, as suggested in Timmermann et al. (1998). In winter, Gastineau and Frankignoul 2012 showed that AMOC intensification and the associated subpolar warming lead to a negative NAO in winter in six climate models. Meanwhile, a gulf stream like SST front keeps the jet stream stationary, and modifies its shape at different pressure levels (Feliks et al. 2016). In summer, the largest atmospheric response to SST resembles the EA pattern and results from a combination of subpolar and tropical forcing (Gastineau and Frankignoul 2014).

At decadal to multi-decadal time scales, the North SST variability is dominated by the Atlantic Multi-decadal Oscillation (AMO; Gastineau and Frankignoul 2014), which has been found to be linked to the AMOC (Gastineau and Frankignoul 2014). A warm AMO leads to atmospheric warming in summer, but a negative NAO in winter (Gastineau and Frankignoul 2014).

The impact of the SST variability on rainfall and river flows has received significant attention, especially for decadal time scales and higher. For instance, the AMO has been found linked to changes in the frequency of occurrence of extremes events in both North America and western Europe (Sutton and Hodson 2005; Sutton and Dong 2012). In particular, a shift in the AMO during the 1960s may have resulted in a cooler US and European climate, before another shift led to a warming phase (Sutton and Hodson 2005; Sutton and Dong 2012). The relationship between SST and extreme events is not limited to the North Atlantic, as evidence shows that the Mediterranean basin experiences the same type of relationships, a warmer (cooler) Mediterranean Sea leading to changes in the rainfall weather patterns over the Mediterranean regions (Polo and Schiemann 2013). The relationship between AMO and rainfall in northern France has only been observed at the 30-60yr' time scales, while the relationship between AMO and temperature has been observed at all inter-decadal to multi-decadal time scales (i.e. 16 year to 80 year' time scales; Dieppois et al. 2013b). The relationship between SST and temperature has been established for the European drought in 2015, with negative SST anomalies in the central North Atlantic ocean, and positive ones in the Mediterranean (Ionita et al. 2017).

2.2.5 Atmospheric circulation dynamics

The atmospheric circulation variability, *i.e.* the trajectory in the system's phase space, displays multiple equilibria, *i.e.* stationary states, identified physically at monthly time scales,

and statistically at annual time scales, as zonal and blocking patterns (Hauser et al. 2015; Ghil et al. 2018). While the zonal states are identified with the eastward mid-latitude jet stream circulation, the blocking patterns have been tied to slowly moving Rossby waves, although the controlling factors of their persistence is still up to debate (Ghil et al. 2018). According to Ghil et al. (2018, and references therein), Stephenson et al. (2004) explains the slow moving Rossby waves by the interference between slowing Rossby waves, while Hannachi et al. (2017) evokes the creation of topographic Rossby waves of different wavenumber that enter in resonance. An alternative view, is that of energy leaks through a waveguide's boundaries, associated with resonant dynamics, the so called "quasi-resonant amplification" (Mann et al. 2018). This difficulty in understanding the cause of persistent blocking patterns lies in the fact that the mechanisms governing the dynamics of Rossby waves, especially the nature of the restoring force, are still under debate (Cai and Huang 2013). The dynamics about those equilibria are also complex, with known bifurcations, stable and unstable transitions (Michael Ghil and Childress 1987). The approaches about those transitions are either considered non-linear deterministic or linear stochastic (Ghil 2019; Ghil and Lucarini 2019).

The combination of atmospheric models, coupled with topography has allowed to describe, at least at the daily to monthly time scales, that zonal patterns had two-way transitions from/to wave train patterns, and one-way transitions to blocking patterns (Michael Ghil and Childress 1987). Using more realistic topography, the NAO and Atlantic Oscillation phases were found as stationary states, with direct transitions from each other states possible, except from AO+ to AO- and reversely (Kondrashov et al. 2004). At inter-annual scales, only statistical work has been done. The NAO and scandinavian blocking-like phases have been found as stationary states (Hauser et al. 2015). Yet their transitions were only established along a time series, and not from a phase space point of view (Hauser et al. 2015).

3. Research objectives and methods

This thesis aims at better understanding the non-linearity and non-stationarity of hydroclimate variability. Particularly, we aim at studying how the complex interactions between hydrological, local and large-scale climate variables shape the spatiotemporal hydroclimate variability in France.

The main research objectives of this thesis are as follows:

- Determine regions of homogeneous hydroclimate variability in France, based on non-stationary spectral characteristics;
- Study non-linear interactions between the different timescales of hydroclimate variability to unravel their possible causal relationships;
- Study the non-stationary spectral characteristics of the watershed modulation of the local climate input;
- Discover non-linear, non-stationary, statistical and spectral spatiotemporal links between local and large-scale hydroclimate variables;
- Unravel stationary, stable or unstable states of the atmospheric circulation as well as their transitions.

Figure I.6 displays the datasets and methods used throughout this dissertation. The emphasis is given to methods allowing accounting for interactions between components of the hydroclimate system (non-linearity), and abrupt changes in the dynamics of the system (non-stationarity).

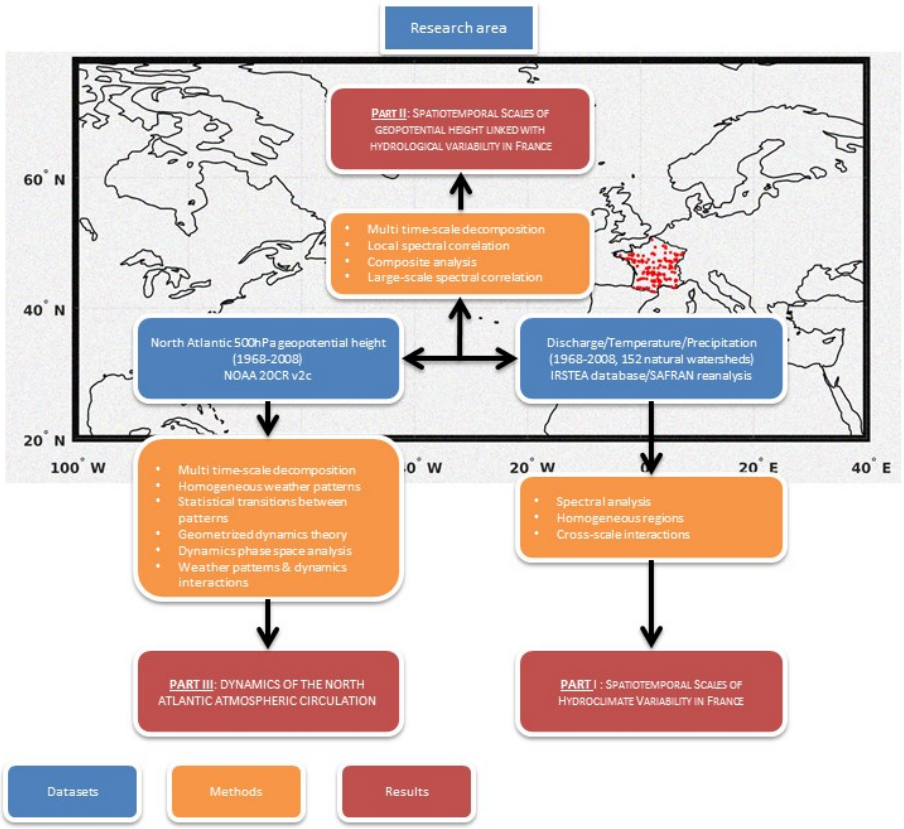

Figure I.6. Datasets and methods used for this thesis. *Red dots show gauging stations. The total atmospheric spatial extent is called the Euro-Atlantic area.*

4. Thesis outline

The **Introduction** provided a general introduction and a review of the current understanding of hydroclimate variability in France. In **Part I**, hydroclimate regions in France of homogeneous spectral variability are computed, then, interaction between their characteristic time scales are investigated. In **Part II**, spectral characteristics of both discharge and local climate variables (*i.e.* precipitation and temperature) are studied to identify potential modulations by the watershed properties on the climate input. Then, spectral characteristics of large-scale climate over the Euro-Atlantic area are compared to those of discharge. In **Part III**, after a theoretical reflection, we study the dynamics of the North Altantic climate

variability using the geometrics-physics correspondence, enabling to decouple the classical vision that associate one pattern with one and only one type of dynamics. Finally, the significance of these findings, their limitations and potential areas of further developments are discussed in the **Conclusion**.

PART I: SPATIOTEMPORAL SCALES OF HYDROCLIMATE VARIABILITY IN FRANCE

Introduction

Hydroclimate variability represents the spatiotemporal evolution of climate variables (*e.g.* precipitation and temperature), which are directly impacting hydrological variability (*e.g.* streamflow, groundwater). Studying how hydrological variables react to climate variability and changes is a major challenge for society, in particular for water resource management and flood and drought mitigation planning (IPCC 2007, 2014).

Hydrological variability fluctuates at multiple timescales (Labat 2006; Schaefli et al. 2007; Massei et al. 2017), which are still poorly characterised and understood in term of driving-mechanisms. As suggested in Blöschl *et al.*, (2019), understanding the spatiotemporal scaling, *i.e.* how the general dynamics driving hydrological variability change at spatial and temporal scales, represent a major challenge (Gentine et al. 2012). The objective is to identify critical scales, *i.e.* the maximum spatiotemporal scale at which the dynamics remain unchanged, also commonly called scaling invariance (Hubert 2001). Critical scales are characteristic of non-linear systems (Hubert 2001). In non-linear system, a slight change in a system parameters can results in large changes in the observed dynamics, as a result of complex interactions between system components, as demonstrated by Lorenz (1963).

Hydrological variability is by definition non-linear (Labat 2000; Lavers et al. 2010; McGregor 2017), as it results from complex interactions between atmospheric dynamics and catchment properties (*e.g.* soil, water table, karstic systems, vegetation; Gudmundsson *et al.*, 2011; Sidibe *et al.*, 2019). However, very little work has hitherto been done to understand how the different drivers of hydrological systems vary at multiple temporal and spatial scales. As suggested in Anishchenko *et al*. (2014), nonlinearity in physical processes is even more likely when time or spatial distance increases. This results in difficulties characterizing the hydrological variability at different spatiotemporal scales (Gentine et al. 2012; Blöschl et al. 2019). Consistently with Blöschl *et al.* (2019), Clark *et al.* (2017) describe scaling, *i.e.* the

transfer of dynamics from small to large scales, and closure, *i.e.* the different couplings between components of a system, as the most important challenges in modelling hydrological variability. However, while different time scales have been identified in hydrological variability at both global and regional scales (Coulibaly and Burn, 2004; Labat, 2006; Dieppois et al. 2016; Massei *et al.*, 2017), very little has been done to explore how coherent are those time scales in space, and therefore in identifying critical scales in which all ranges of variability remain unchanged.

Studying 231 steam gauges throughout the world, Labat (2006) highlighted different time scales of streamflow variability over the different continents. At the regional scale, Smith et al. (1998) established a clustering of 91 US stream gauges based on their global wavelet spectra, *i.e.* dominant time scales, and found five homogeneous regions. Similarly, Anctil & Coulibaly (2004), and Coulibaly & Burn (2004) for Canada, established a clustering of southern Québec streamflow, based on the timing of both the 2-3 and 3-6 year time scales, distinguishing the northern and southern regions. In Europe, Gudmundsson et al. (2011) identified different regions according to their low-frequency fluctuations (defined by the authors as timescale of variability greater than 10 years). In France, such clustering based time-frequency patterns of streamflow variability, as well as its relation to climate variability (e.g. precipitation and temperature), has not yet been explored. In addition, all the studies mentioned above either isolate different time scales or average the variability across time scales (*e.g.* global wavelet spectra), which is equivalent to a linearization of the system (Hubert *et al.*, 1989). In this study, we propose to combine wavelet analysis and a new fuzzy-clustering algorithm to understand the spatial coherence of precipitation, temperature and streamflow variability over France in fully non-linear approach accounting for both time and frequency domains.

The work is divided into the following parts. Data and methods are introduced in Section 1. In Section 2, we cluster precipitation, temperature and discharge variability based on their scale-time patterns. Couplings between the different time scales of variability are then explored in Section 3. Finally conclusion and discussion of the main results are provided in Section 4.

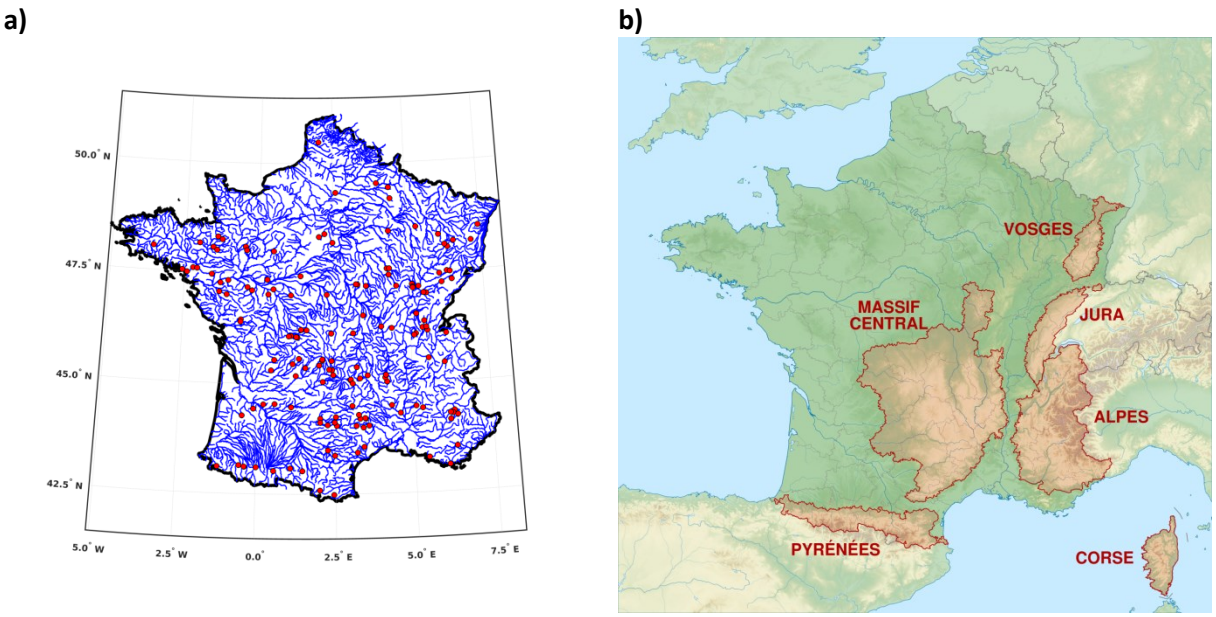

Figure 1.1. Research area. *a) Location of stream gauges (red dots) and their respective hydrographic networks (blue lines); b) Orography over France, and delineation of mountain ranges.*

1. Data and Methods

1.1 Hydrological and Climate Data

Discharge time series were extracted from the observation dataset introduced by Bourgin *et al.* (2010a, b). This data set is composed of 4496 watersheds, their main river daily time series and their hydrologic descriptions. This data set was initially subset to low anthropogenic influenced and low groundwater support watershed, comprising 662 stations. We further

reduced the data to 152 stream gauges, by keeping only continuous time series from January 1968 to December 2008 (Figure 1.1).

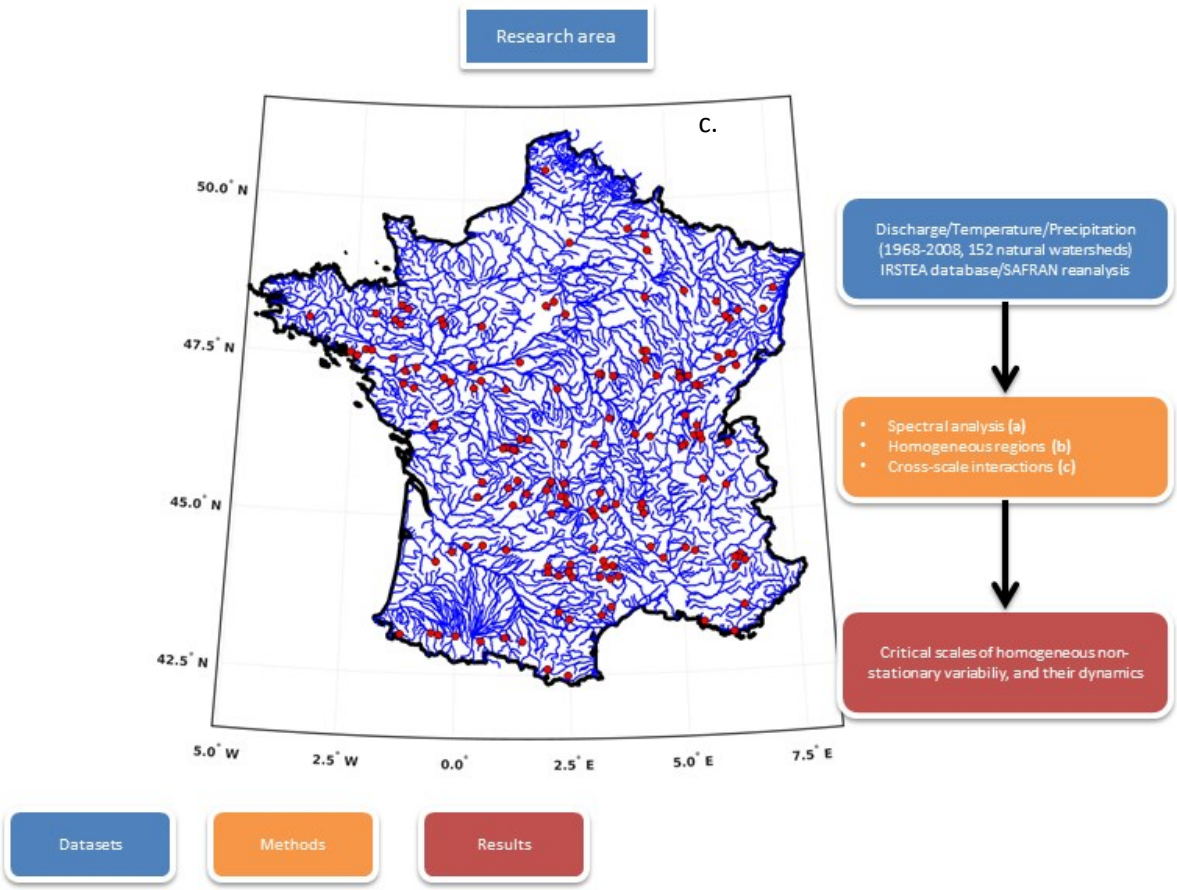

Figure 1.2. Workflow of this study. *a.) 152 monthly precipitation, temperature and discharge time series are extracted from IRSTEA's watershed database. The following steps are applied to each variable; b.) The continuous wavelet spectrum for each watershed is computed; c.) A distance matrix between wavelet spectra is then established; d.) A fuzzy clustering algorithm is used to build a classification map of the watersheds based on their wavelet spectra.*

Precipitation and temperature data have been estimated from the SAFRAN reanalysis data set ("Systeme d'Analyses Fournissant des Renseignements Adaptes a la Nivologie"; Vidal et al. 2010). The data is formatted as a regular rectangular grid of 8 kilometers' spaced nodes that

covers metropolitan France. Data start in August 1958, and are regularly updated. For this study, the precipitation and temperature have been averaged over each watershed.

1.2 Methods

Figure 1.2 sums up the different steps of this study. First we compute the non-stationary spectral characteristics of each watershed precipitation, temperature and discharge, using continuous wavelet transforms (Figure 1.2, (a)). Then we use cluster the wavelet transforms of each watershed's variable, using IEDC and fuzzy clustering techniques, which gives the spatial critical scales of homogeneous variability (Figure 2, (b)). We finally study the non-linear interactions taking place between the different time scales of each homogeneous region (Figure 1.2, (c)).

1.2.1 Continuous wavelet transforms

Scale-Time patterns have first been extracted for each watershed, and each variable, using continuous wavelet transform (cf. Figure 1.2, (a)). For any finite energy signal x, it is possible to obtain a scale-time representation by mapping it to a series of subspaces spawned by a generating function, the mother wavelet, and its scaled versions (Torrence and Compo 1998; Grinsted et al. 2004). The time series is then represented in terms of a given scale and time location. The first subspace is generated by a mother wavelet at scale 1 and its time translations. Then, other subspaces are generated by scaling the mother wavelet up, referring to daughter wavelets, and time translating it. For each scale, one subspace is constructed. Daughter wavelets are usually calculated as:

$$\psi_{a,b} = \frac{1}{\sqrt{a}}\psi\left(\frac{t-b}{a}\right) \qquad (1)$$

The left hand side (LHS) term is the daughter wavelet of scale a and time translation b at time t. The first right hand side (RHS) term is the scaling of the mother wavelet ψ and the last one is the time translation.

The projection of the signal onto each scale a subspace is of the form:

$$WT_{\psi}\{x\}(a,b) = < x.\psi_{a,b} > = \int_{R} x(t)\psi_{a,b}(t)dt \qquad (2)$$

LHS term contains the wavelet coefficients, i.e. the coordinates of the signal in each subspace. If the mother wavelet (and hence the daughter wavelets as well) is complex, wavelet coefficient are complex as well. Wavelet coefficients represent the inner product of the signal and daughter wavelet of scale a and time translation b (Centre Hand Side). The norm of their square is called the wavelet power and represents the amplitude of the oscillation of signal x at scale a and centred on time t. As it is impossible to capture the best resolution in both and time at the same time, here, we used a Morlet mother wavelet (order 6), which offers a good compromise between detection of scales and localisation of the oscillations in time (Torrence and Compo 1998).

1.2.2 Image Euclidean Distance Clustering

As shown in Figure 1.2(b), the similarities between wavelet spectra of each watershed, and, separately, on each variable, have been estimated. Distances between 2-dimensional data, such as maps or wavelet spectra, are commonly estimated using Euclidean distance between pairwise points (pED; i.e computing $f_2(x_1, y_1) - f_1(x_1, y_1)$). However, such a procedure has

no neighborhood notion, making it impossible to account for globally similar shapes (cf. definition of global and local similarity in Wang et al. 2005).

To avoid this issue, Wang et al. (2005) developed the Image Euclidean distance calculation method (hereinafter IEDC). The IEDC method modifies the pED equation in two ways (Wang et al. 2005): i) the distance between pixels values is computed not only pairwise, but for all indices; ii) a Gaussian filter, function of the spatial distance between pixels, is applied. The Gaussian filter then applies less weight to the computed distance between very close and far apart pixels, while emphasizing on medium spaced ones (Wang et al. 2005).

1.2.3 Fuzzy clustering

Fuzzy clustering has then been used to cluster the different watershed based on their similarities (Figure 1.2, (b)). Fuzzy clustering is a soft clustering method (Dunn 1973). While soft clustering spreads membership over all clusters but with varying probability, hard clustering attributes each station one and only one cluster membership. Soft clustering is therefore better-suited when the spatial variability, originating from different stations' characteristics, is smooth, such as in hydroclimatic data.

For instance, precipitation and temperature patterns are unlikely to change suddenly from one station to a neighboring one, and in turn, markedly different from the next neighbor (Moron *et al.*, 2007; Lloyd-Hughes *et al.*, 2009; Rahiz & New, 2012). As such, several stations tend to show transitional or hybrid patterns, and can potentially be member of different clusters, limiting the robustness of hard clustering procedure (Liu and Graham 2018). In this study, we used the FANNY algorithm (Kaufman & Rousseeuw, 1990). Fuzzy clustering performance is determined by the ability of the algorithms to recognize hybrid stations (*i.e.* stations incorporating multiple features from different patterns observed in other coherent regions), while allowing for a clear determination of the membership of stations with unique features (Kaufman & Rousseeuw, 1990). Fanny clustering has been shown to be flexible with the

modification of its exponent r, offering the possibility to adapt the clustering to the data, and to enhance performance (Liu and Graham 2018). A critical part is however the selection of the optimal number of clusters. Rather than setting the number arbitrarily, we use an estimation of the optimum number of clusters by first computing a hard clustering method: the consensus clustering (Monti et al. 2003). Thus, the number of clusters providing the best stability (*i.e.* the minimal changes of membership when new individuals are added) is considered optimal as recommended in Şenbabaoğlu et al. (2014). The different clusters' memberships are then mapped to discuss the spatial coherency of each hydroclimate variable (cf. Figure 1.2).

1.2.4 Cross scales interactions

For each variable and each cluster, cross-scale interactions have also been explored (Figure 1.2, (c)). Cross-scale interactions refer to phase-phase and phase-amplitude couplings between time scales of a given time series (Paluš, 2014; hereinafter PS14). Here, coupling means that the state (either phase or amplitude) of a signal y is dependent on the state of a signal x. Such couplings are non-linear, and, therefore, if the amplitude of y varies with the phase of x, the reverse is not necessarily true. Thus, in the classical setting, for any directional coupling (*e.g.* $x \rightarrow y$), there must be a lag in the relationship between x and y. When both oscillations are synchronized, changes in x affect y in the same way changes in y affect x, and a symmetry takes place. In that case, the $x \rightarrow y$ relationship may either have a lag shorter than the time series time step or be part of a larger system (Pikovsky *et al*., 2001). The different couplings describe causality relationship, such as described in (Granger 1969), referring to information transfer from one part of the signal to another. Granger causality is the potential for improving the prediction of the future of y knowing information about the past of x. Following PS14 and Jajcay et al. (2018), who compares the most used methods when

studying causality, we choose the conditional mutual information (CMI) surrogates method, combined with wavelet transforms.

First, using a Morlet mother wavelet, the instantaneous phase and amplitude at time t and scale s of the signal are obtained. Next, the conditional mutual information, $I\left(\phi_x(t); \phi_y(t+\tau) - \phi_y(t) \middle| \phi_y(t)\right)$ for the phase and $I\left(\phi_x(t); A_y(t+\tau) \middle| A_y(t)), A_y(t-\eta)), A_y(t-2\eta)\right)$ for amplitude is computed. In the case of the phase-phase, the CMI measures how much the present phase of x contains information about the future phase of y knowing the present value of y. For the amplitude, CMI measures how much the present phase of x contains information of the future amplitude of y knowing the present and past values of y. The statistical significance of the CMI measure is assessed using 5000 phase-randomized surrogates, having the same Fourier spectrum, mean and standard deviation as the original time series, as in Ebisuzaki (1997).

2. Spatiotemporal clustering of hydrological variability

The wavelet transforms of each station have been computed and checked for similarities using IEDC fuzzy clustering to identify homogeneous regions and characterize critical scales of hydroclimate variability over France. Cross scale couplings were then investigated for each homogeneous region.

2.1. Precipitation

2.1.1. Scale-time patterns

Seven regions with homogeneous scale-time patterns are identified (Figure 1.3a): North-western (#CL1-Pr, green), North-eastern (#CL2-Pr, blue), Centre-north (#CL3-Pr, red), Centre-western (#CL4-Pr, pink), Centre-eastern (#CL5-Pr, black), South-western (#CL6-Pr,

.

yellow) and South-eastern (#CL7-Pr, dark green). According to the global wavelet spectra (Figure 1.3b), precipitation is fluctuating at different time scales, ranging from seasonal to inter-annual (i.e. 2-8 years). The wavelet spectra (Figure 1.3c) show that those different time scales are non-stationary, with temporal changes in terms of amplitude discriminating the regions.

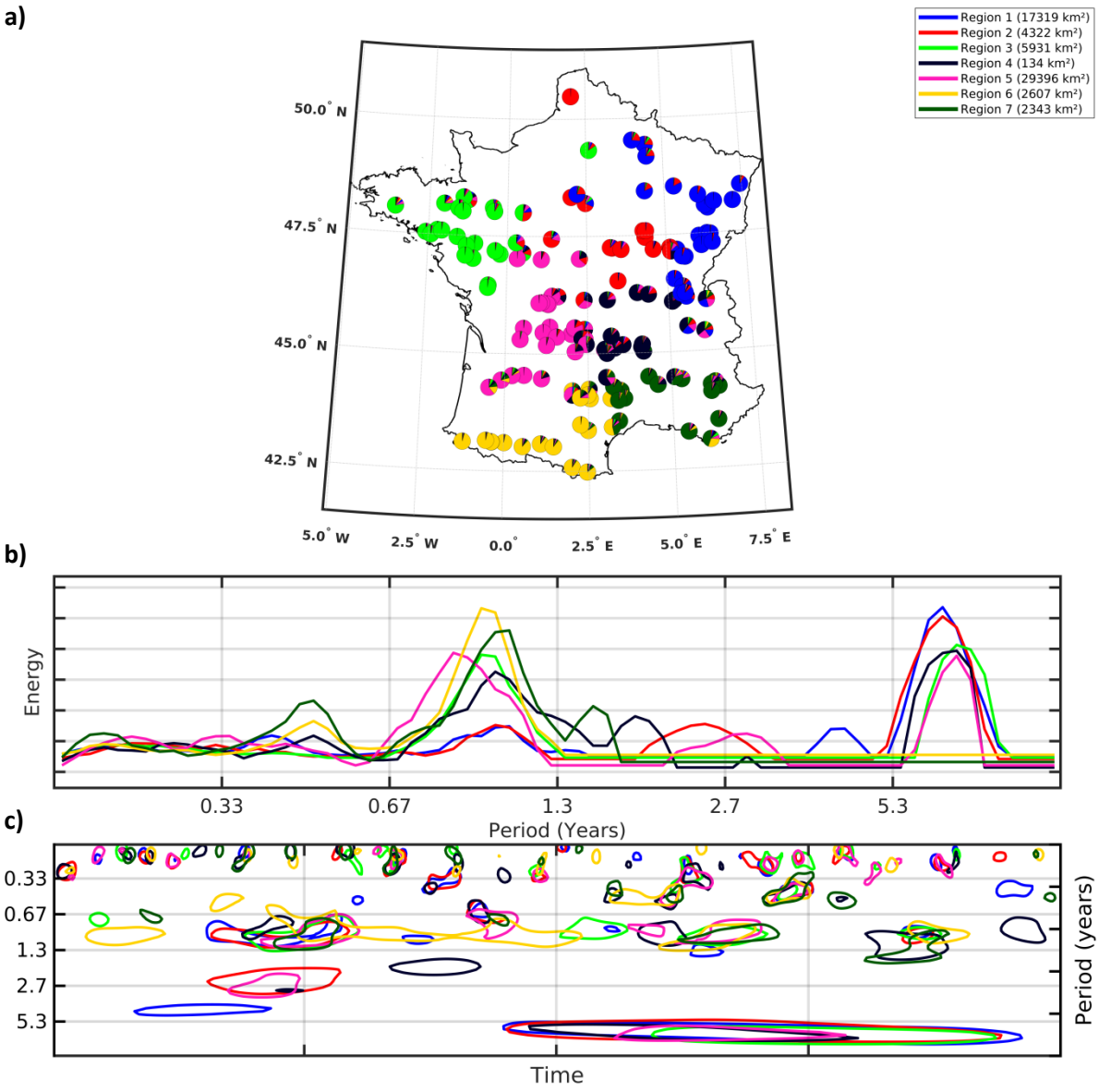

Figure 1.3. Clustering of precipitation scale-time variability in France. *a.)*

Classification map of the watersheds. Pie charts slices show the three highest probability

memberships; b.) Global wavelet spectra for each cluster; c.) Statistically significant wavelet spectra for each cluster.

For instance, while other watersheds show sparsely significant annual variability, south-western watersheds are characterized by quasi-continuous annual variability until the late 1980s (Figure 1.3c). Similarly, although there is significant inter-annual variability in all watersheds from the late 1980s on the monthly wavelet spectrum, there is no significant inter-annual variability over the south-western and south-eastern watersheds (Figure 1.3c). Focusing on inter-annual time scales, however, significant fluctuations at ~4 and 8 years appear for those watersheds, yet, over shorter periods of time (Figure 1.4a-b).

In summary, different regions, coherent in precipitation variability, have been identified, and describe critical scales. The critical scales of homogeneous precipitation variability are significantly different depending on the region, for instance, Centre-eastern region (#CL4-Pr, black) covers 134km², while the Centre-western region covers more than 29000km² (Figure 1.1a). Interestingly, most regions seem delineated by orography (cf. Figure 1.1b), except for north-western watersheds.

2.1.2. Cross-scale interactions

Figure 1.5 shows cross-scale interactions for each cluster of precipitation variability identified in section 2.1.1.

As described in Figure 1.5a, north-western watersheds display bi-directional (i.e. feedback) phase-phase causality between 5-6yr and 6-7yr time scales variability. This suggests different physical processes at play within the 5-8yr variability, as displayed in Figure1. 3-4b. North-eastern watersheds display phase-phase causality from 4-7.5yr to 2-4yr time scales, as well as 3-5yr to 7-8yr time scales (Figure 1.5a). This suggests that the scale extent of the significant patch of inter-annual variability shown in Figure 1.3b-4b is resulting from several interacting

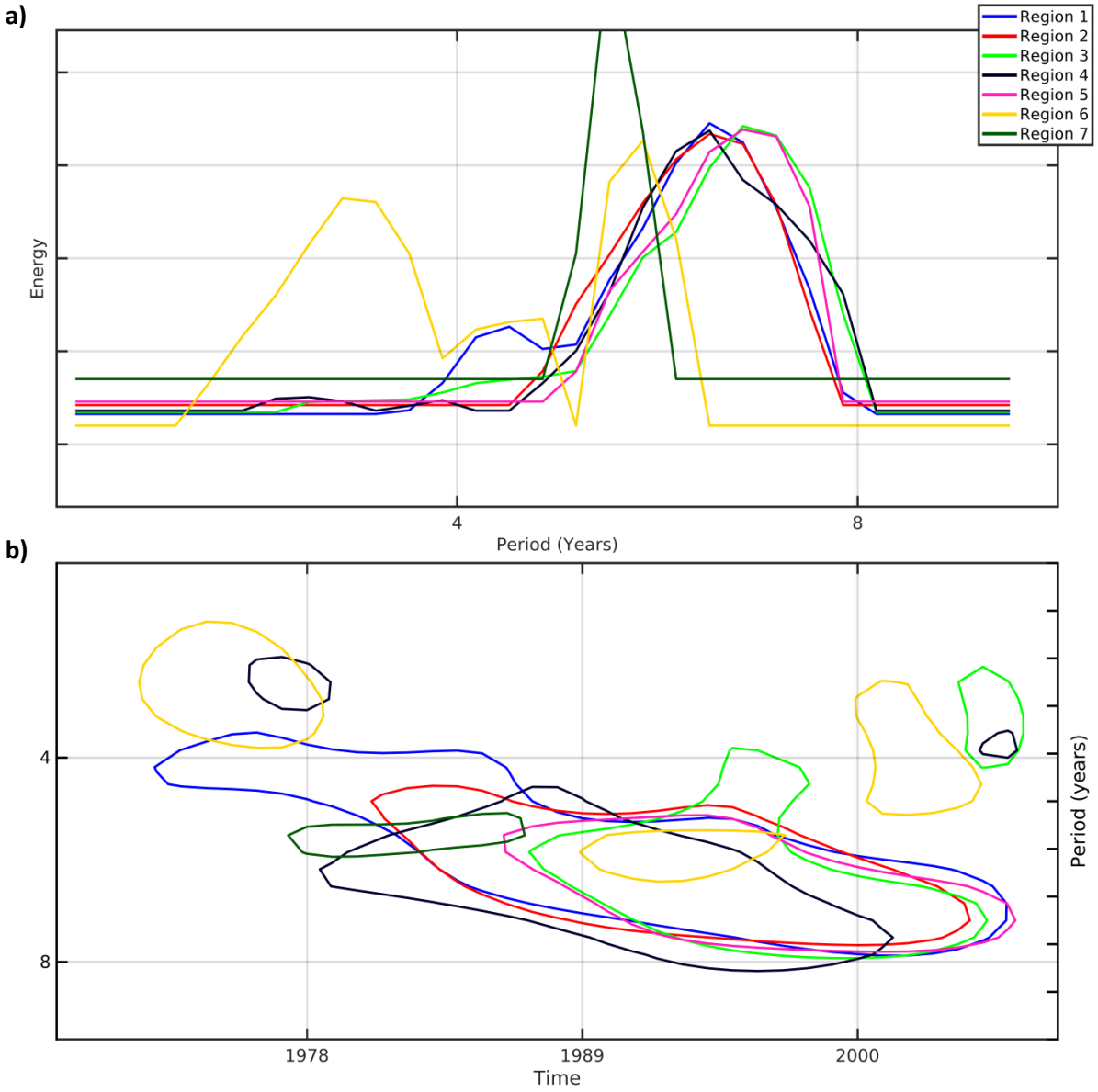

Figure 1.4. Inter-annual precipitation scale-time variability in France. *a.) Global wavelet spectra for each cluster; b.) Statistically significant wavelet spectra for each cluster.*

dynamics. Centre-northern watersheds show phase-phase causality from 2-3 to 3-4yr time scales, explaining the 2-4yr patch in Figure 1.3b. Two additional interactions take place, first from 6-7yr to 4.5-5yr, and from 7-8yr to 5.5-6yr time scales (Figure 1.5a), resulting in the 4-8yr inter-annual patch displayed in Figure 1.4b. Centre-eastern watersheds show phase-phase causality from 4yr to 6.5yr and from 7.5-8yr to 6.5-7yr time scales, resulting in the scale

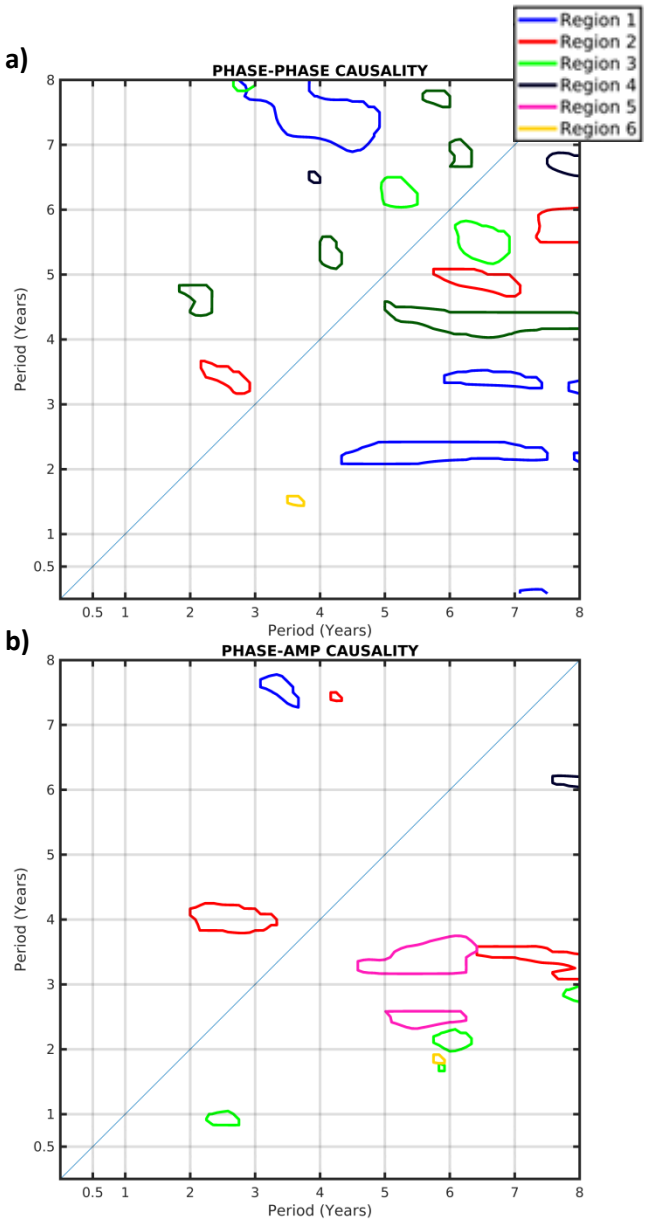

Figure 1.5. Precipitation cross-scale interactions. *The driving scale is on the horizontal axis, the driven on the vertical axis. a.) Phase-phase causality; b.) Phase-amplitude causality.*

extent of the inter-annual patch in Figure 1.4b. South-western watersheds display phase-phase causality from 3.5yr to 1.5yr time scales (Figure 1.5a). Cascade phase-phase causality, i.e. sequential driving/driven relationships from higher (lower) to lower (higher) time scales, are observed in South-eastern watersheds. The phase-phase causality appears from 5-8yr to 4-5yr time scales over the same region (Figure 1.5a). Meanwhile, there is no phase-phase coupling in centre-western watersheds (Figure 1.5a).

Looking at phase-amplitude causality, north-western watersheds display interactions from 2-3yr to 1yr, from 6yr to 2yr, and from 8yr to 3yr time scales (Figure 1.5b). Thus, over this region, there is a link between higher time scales' phases and lower time scales' amplitude, resulting in significant patches in Figures 1.3b, 4a. North-western watersheds show phase-amplitude causality from 3-4yr to 7-8yr timescales (Figure 1.5b). Centre-northern watersheds

display phase-amplitude causality from 2-3yr to 4yr, from 6-8yr to 3-5yr, and from 4yr to 7.5yr time scales (Figure 1.5b). South-western watersheds show isolated phase-amplitude causality from 6yr to 2yr time scales (Figure 1.5b). Centre-eastern watersheds show phase-amplitude causality from 8yr to 6yr time scales (Figure 1.5b). Centre-western regions show phase-amplitude causality from 5-6 to 2-4 years (Figure 1.5b). Meanwhile, there is no phase-amplitude coupling in centre-eastern watersheds (Figure 1.5a).

The precipitation cross-scale interactions can be phase-phase, phase-amplitude, uni- or bi-directional, from lower to higher time scales and vice versa. However, such cross-scale interactions are different in all regions, suggesting different internal dynamics.

2.2. Temperature

2.2.1. Scale-time patterns

In temperature, nine regions with homogeneous scale-time patterns are identified (Figure 1.6a): North-western-high (#CL1-Tp, pink), North-western-low (#CL2-Tp, black), North-eastern (#CL3-Tp, blue), Centre-eastern (#CL4-Tp, red), Centre-western (#CL5-Tp, green), South-eastern-high (#CL6-Tp, yellow), South-eastern-low (#CL7-Tp, brown), South-western-high (#CL8-Tp, dark green) and South-western-low (#CL9-Tp, purple). Using monthly data, temperature is fluctuating only at the annual time scale with very similar amplitudes for all clusters, as shown on the global wavelet spectra (Figure 1.6b). Similarly, continuous wavelet

spectra show significant annual fluctuations throughout the time series in all regions (Figure 1.6c).

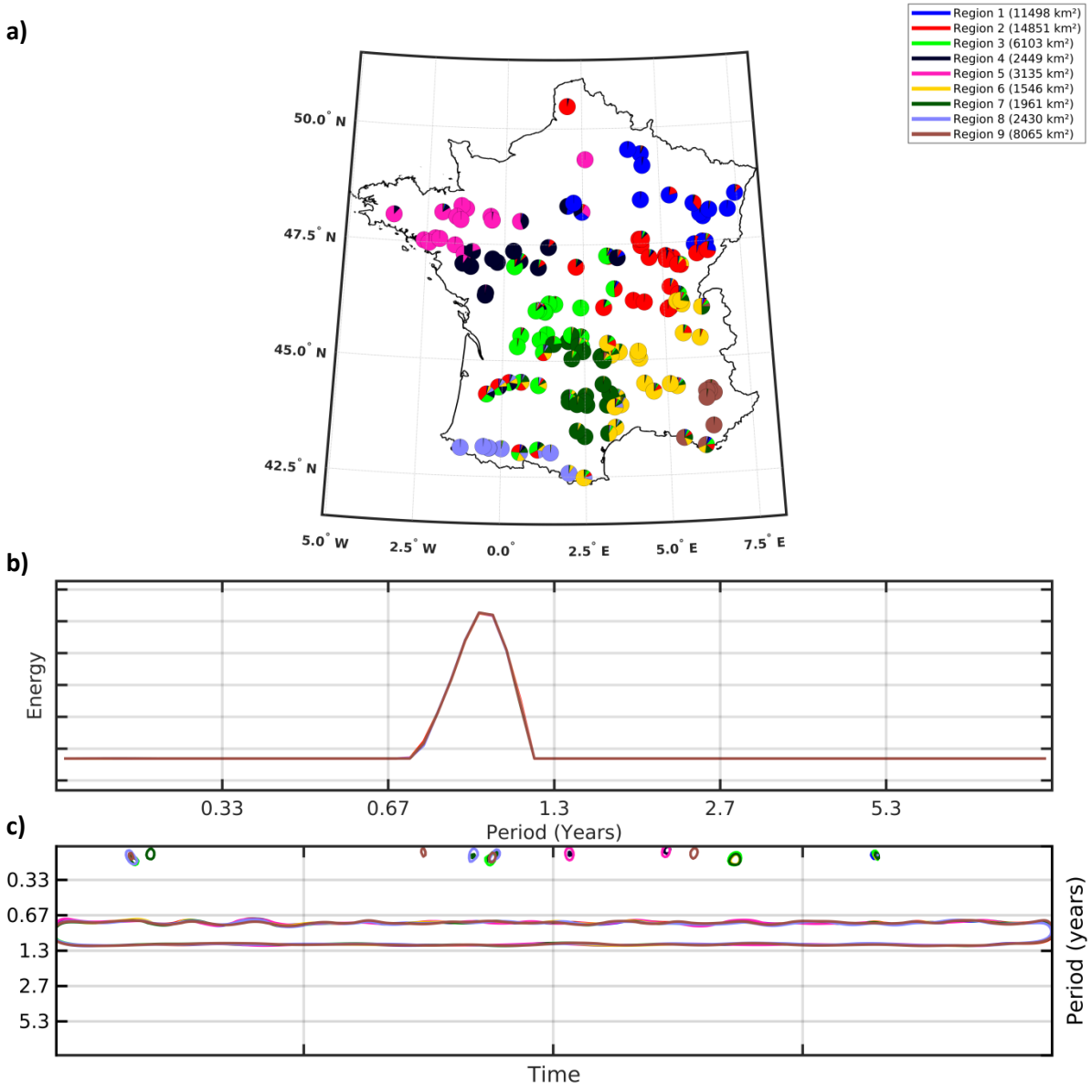

Figure 1.6. Clustering of temperature scale-time variability in France. *a.) Classification map of the watersheds. Pie charts slices show the three highest probability memberships; b.) Global wavelet spectra for each cluster; c.) Statistically significant wavelet spectra for each cluster.*

Focusing on inter-annual time scales, significant fluctuations occur at both 2-4yr and 5-8yr time scales, and lead to discrepancies between the different clusters (Figure 1.7a-b). For instance, South-eastern-low watersheds show variability at ~3yr time scale, while other clusters are centred on ~2yr (Figure 1.7a). 3yr variability in South-eastern-low watershed is more pronounced than in other clusters at ~2yr time scale (Figure 1.7a). The South-western-low watersheds' wavelet spectra also display different timing for the ~3yr time scales than other clusters, with variability in the mid 1980's and mid 1990's, only (Figure 1.7b).

In summary, different coherent regions in temperature variability have been identified, and describe critical scales. At the annual time scale, only amplitudes seem to differentiate regions. At the inter-annual scales, however, differences in time scales and their timings emerge. Critical scales of temperature are less variable than for precipitation, still, there is a factor of ten between the size of South-eastern-high region (#CL6-Tp, yellow,1500km²), and the one of Centre-eastern region (#CL4-Tp, red, 15000km², Figure 1.6a). As in precipitation, topography still seems to be a delineator, but critical scales are smaller, with different clusters detected over the same mountain range.

2.2.2 Cross-scale interactions

Figure 1.8 shows cross-scale interactions for each cluster of temperature variability identified in section 2.2.1.

As shown in Figure 1.8a, north-western-low and north-western-high watersheds show phase-phase causality of the 2-3yr on the 1yr scales, and of the 4yr on 6yr scales. In addition, north-western-high watersheds show 2.5yr on 6yr scales, and 3yr on 7.5yr time scales, phase-phase causality (Figure 1.8a). North-eastern and centre-eastern watersheds display similar phase-phase causality of the 4-5yr on both 6.5-7yr and 7.5-8yr time scales (Figure 1.8a). This suggests that the scale extent of the significant patches of inter-annual variability, as shown in

Figure 1.6b-7b, is resulting from several interacting dynamics. Centre-western watersheds show different phase-phase causality interactions: 0.5yr → 5.5yr , 2.5yr → 4yr, and 1.5yr → 1yr time scales (Figure 1.8a). The phase-phase interactions for centre-western watersheds are thus driven by smaller time scales. South-eastern-high watersheds only show phase-phase causality of the 4yr on 7yr time scales (Figure 1.8a). South-eastern-low watersheds display bi-directional phase-phase causality between 3.5yr and 4.5yr time scales. Thus, this suggests that a complex feedback is at play at those scales, and may explain the specificity of south-western-low watersheds' wavelet spectra in Figure 1.7b. In South-eastern-low regions, phase-phase interaction of the 5yr on 2.5yr time scales is also identified (Figure 1.8a). South-western-high watersheds show phase-phase causality of the 7yr on 6yr time scales, and of the 6 on 7-8 (Figure 1.8a), thus partly bi-directional. South-western-low watersheds show phase-phase causality of the 8yr on 3yr time scales, and of the 8yr on 5.5yr scales (Figure 1.8a).

Looking at phase-amplitude causality, north-western-high watersheds show an interaction between the phase and amplitude of ~3yr time scale (Figure 1.8b). According to the definition of phase-amplitude causality, such an interaction between the phase and amplitude at a single time scale cannot be explained by a single process, and thus suggests that at least two processes are interacting at this time scale. North-western-low watersheds show phase-amplitude causality of the 7yr on 4yr time scales (Figure 1.8b). While, the 4yr time scale have low amplitude (cf. Figure 1.7a), its variability is partly driven by the phase of the 7yr time scales (Figure 1.8b). Centre-eastern cluster show phase-amplitude causality of ~4yr scale on itself, as well as 3yr on ~4yr time scales (Figure 1.8b), suggesting very complex interactions. Centre-western watersheds show bi-directional phase-amplitude causality between 6.5-7yr and 2.5-3yr time scales (Figure 1.8b). South-eastern-high cluster show self-interaction of ~4yr time scales (Figure 1.8b). South-eastern-low watersheds show several phase-amplitude

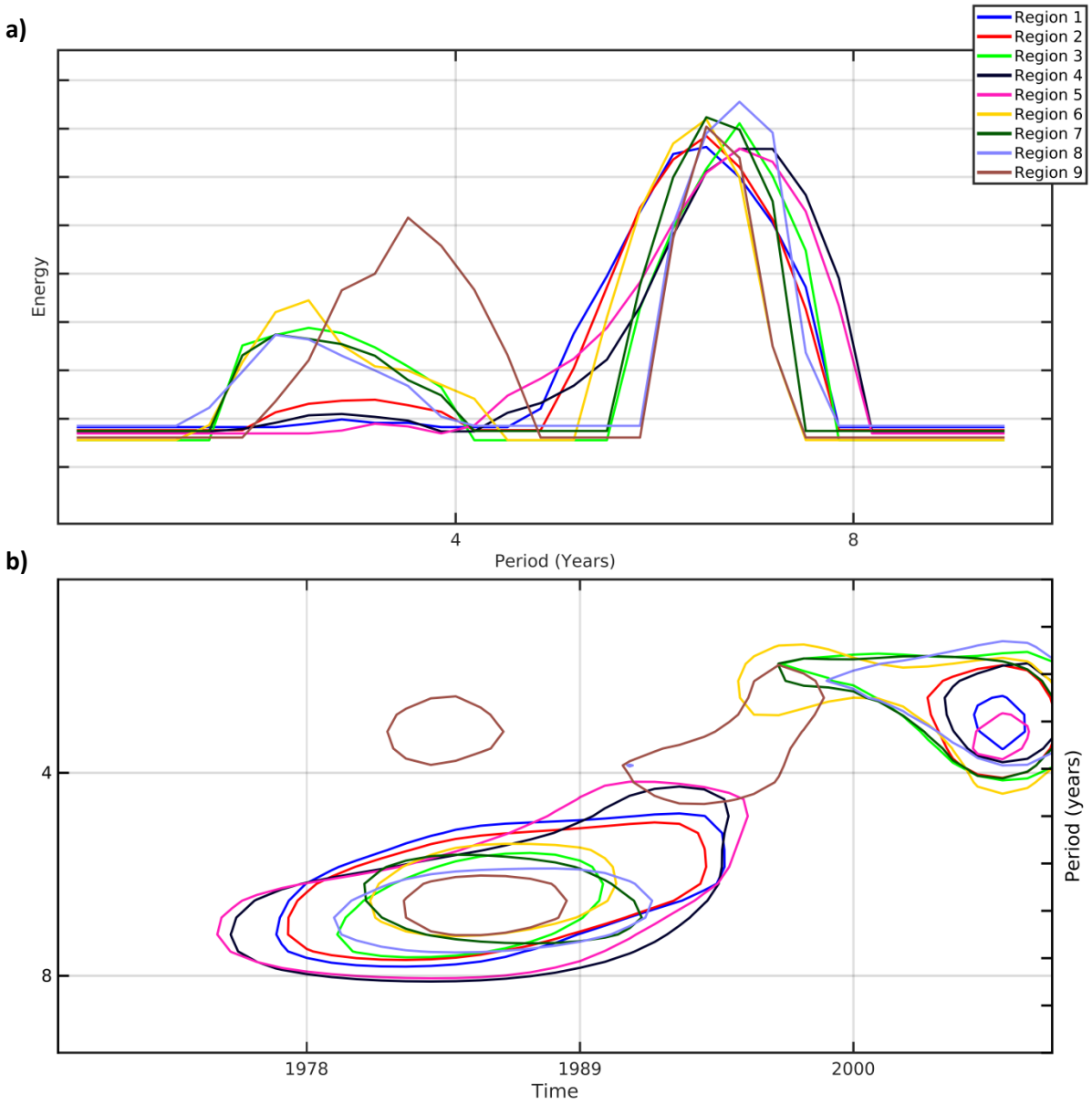

Figure 1.7. Inter-annual temperature scale-time variability in France. *a.) Global wavelet spectra for each cluster; b.) Statistically significant wavelet spectra for each cluster.*

interactions, which can be split into three types (Figure 1.8b). First, quasi-self-interactions occur between 2-3yr and 2yr time scales (Figure 1.8b). Second, phase-amplitude causality of larger time scales on smaller time scales (Figure 1.8b): 5yr → 3.5yr, 5.5yr → 1.5yr, and 8yr →2yr. Third, phase-amplitude causality of smaller time scales on larger time scales, as between 2.5 and 6.5 years scales (Figure 1.8b). The complexity of the phase-phase and phase-

amplitude interactions for the south-eastern-low watersheds may explain the peculiarity of their wavelet spectra (Figure 1.7a-b).

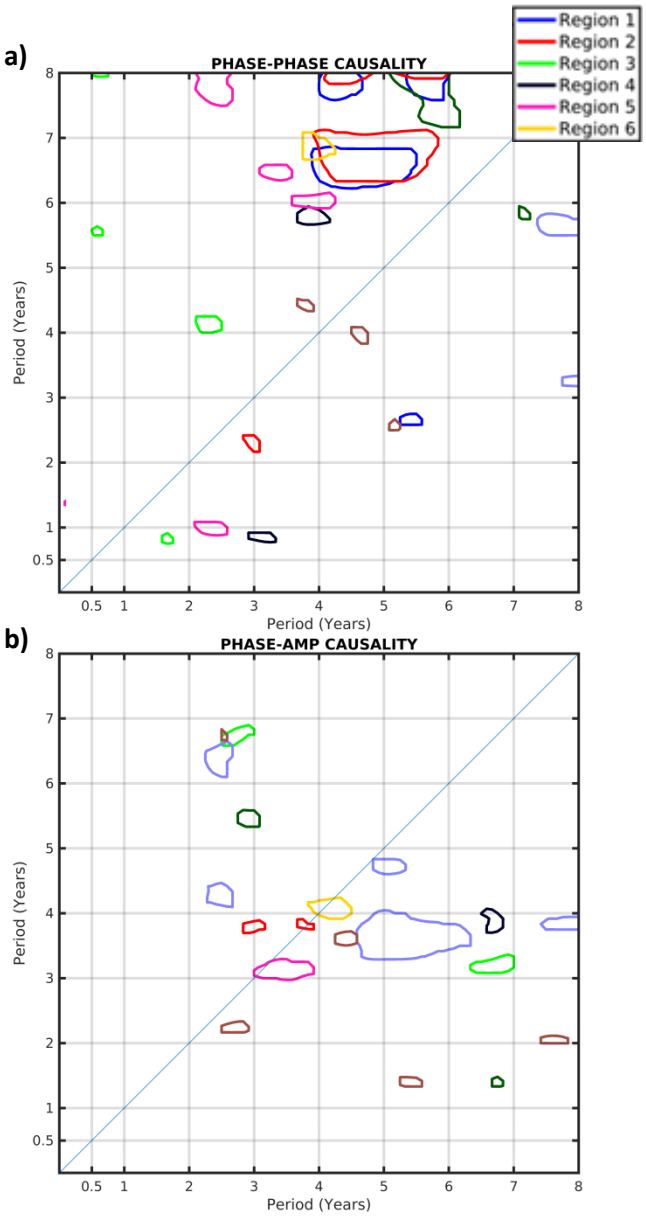

Figure 1.8. Temperature cross-scale interactions. *The driving scale is on the horizontal axis, the driven on the vertical axis. a.) Phase-phase causality; b.) Phase-amplitude causality.*

South-western-high watersheds are characterized by a quasi-bi-directional interaction between 6yr and 7-8yr time scales (Figure 1.8b). South-western-low region is also characterized by different cross-scale interactions (Figure 1.8b): i) ~4yr time scales amplitude being partly

driven by the 2yr and 5-8yr time scales; ii) Self-interactions of the phase and amplitude of the 5yr time; iii) the 5-6yr time scale phase modulating the amplitude of the ~3-4yr time scales.

The temperature cross-scale interactions can be phase-phase, phase-amplitude, uni- or bi-directional, from lower to higher time scales, and vice versa. There are also significant self-interactions (*i.e.* interaction of one time scale on itself), suggesting more than one processes at play at the same time scale. However, such cross-scale interactions are different in all regions, suggesting different internal dynamics.

2.3. Discharge

2.3.1. *Scale-time patterns*

Six regions with homogeneous scale-time patterns are identified (Figure 1.9a): North-western (#CL1-Q, black), North-eastern (#CL2-Q, blue), North-centre (#CL3-Q, red), Centre-western (#CL4-Q, green), South-eastern (#CL5-Q, yellow) and South-western (#CL6-Q, pink). Using monthly data, discharge is mainly fluctuating at annual time scales, as determined through the global wavelet spectra (Figure 1.9b). One cluster, *i.e.* the South-eastern regions, however, shows significant intra-seasonal variability (Figure 1.9b).

Continuous wavelet spectra show that both annual and intra-seasonal variability can be non-stationary, with temporal changes in terms of amplitude discriminating the regions (Figure 1.9c). For instance, while other watersheds show almost continuous significant annual variability, annual variability is only significant for specific periods in South-eastern watersheds (Figure 1.9c). Similarly, South-eastern region, intra-seasonal variability sparsely appears significant from the 1980's (Figure 1.9b).

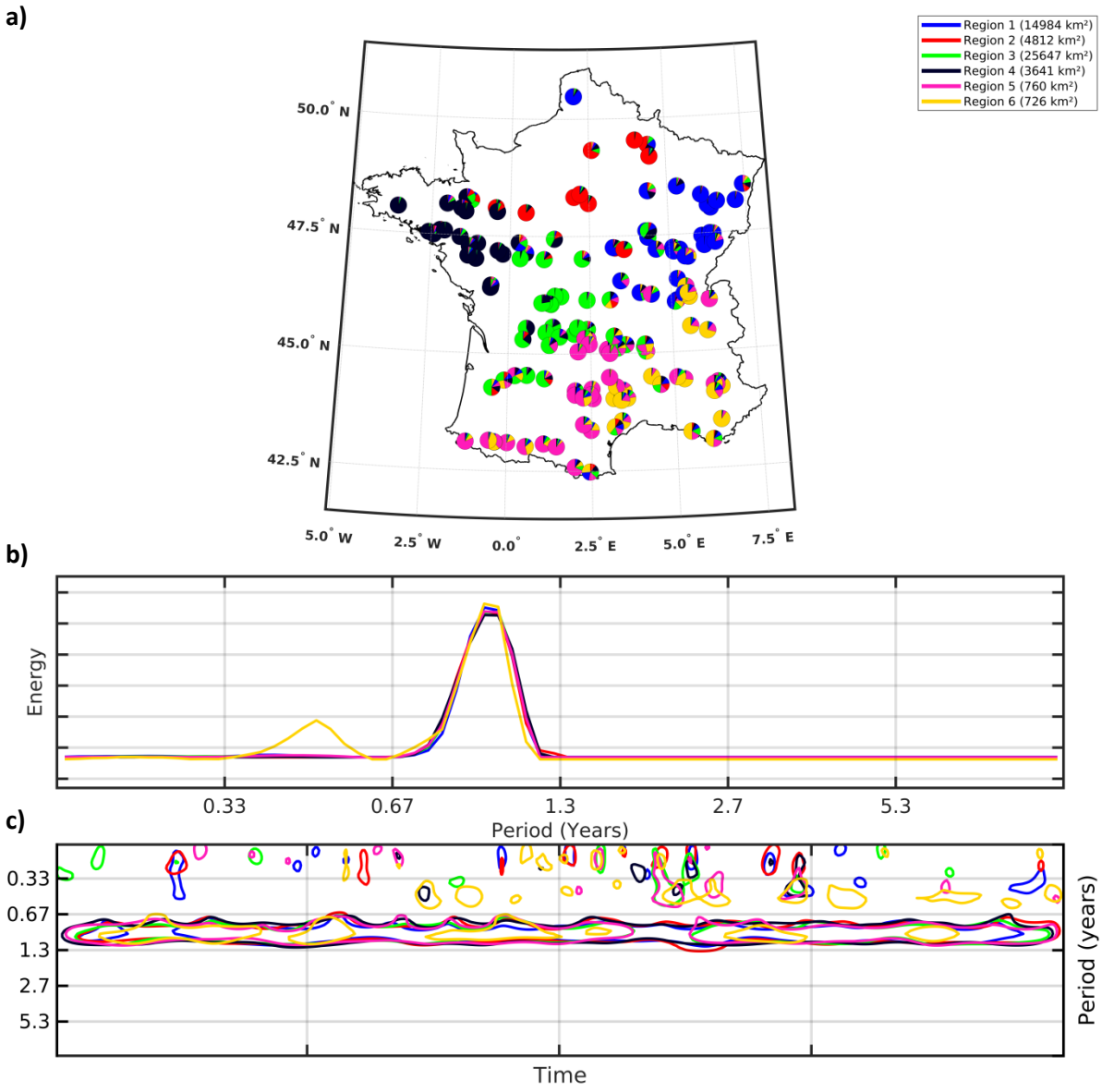

Figure 1.9. Clustering of discharge scale-time variability in France. *a.) Classification map of the watersheds. Pie charts slices show the three highest probability memberships; b.) Global wavelet spectra for each cluster; c.) Statistically significant wavelet spectra for each cluster.*

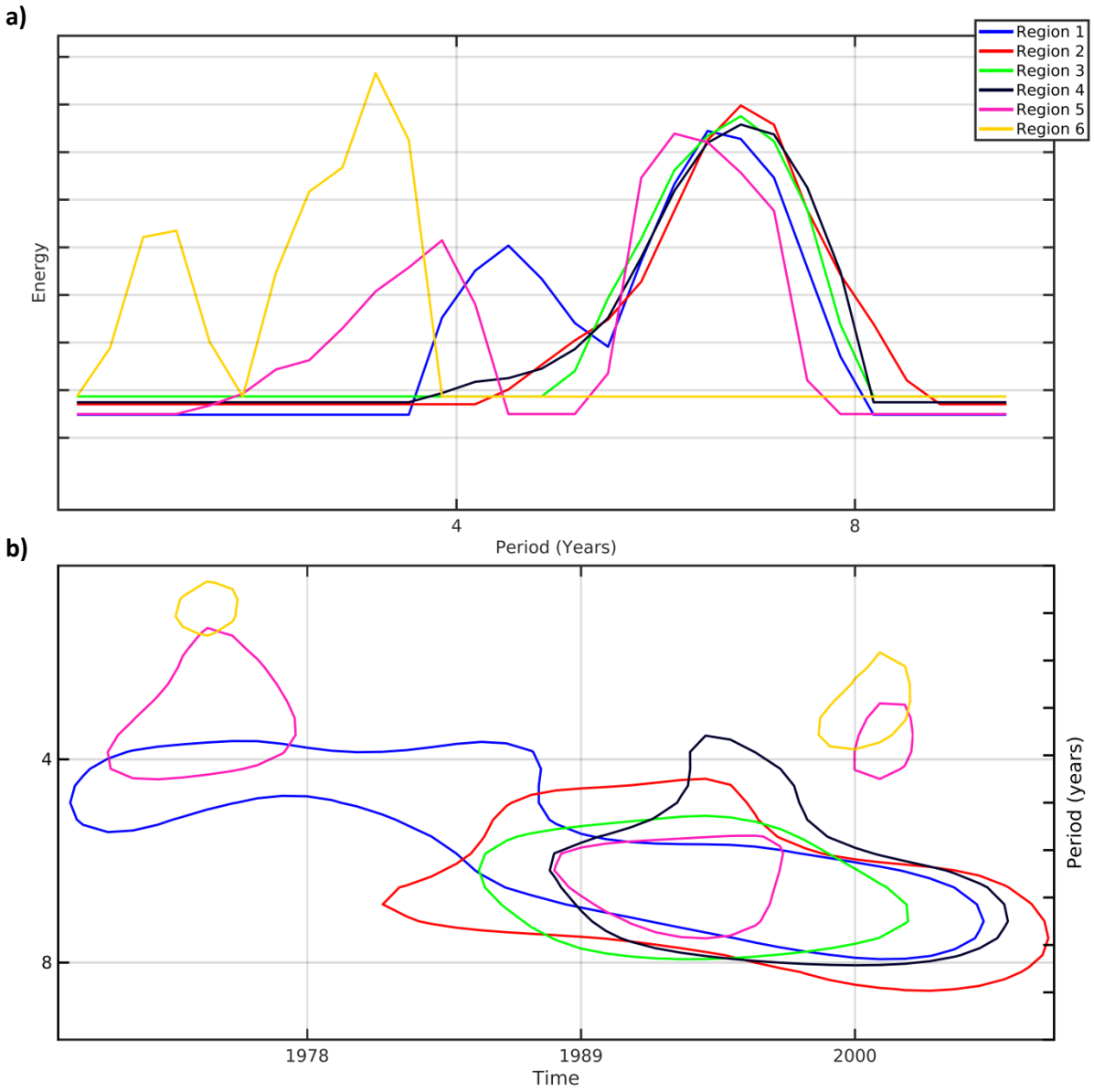

Figure 1.10. inter-annual discharge scale-time variability in France. *a.) Global wavelet spectra for each cluster; b.) Statistically significant wavelet spectra for each cluster.*

Focusing on inter-annual scales, north-eastern watersheds stand out having continuous significant inter-annual variability throughout the time series, with 4-5yr variability before the 1990's, and 5-8yr variability after (Figure 1.10b). South-eastern and -western clusters also stand out, showing 2-4yr variability at the beginning and end the time series (Figure 1.10b). In addition, South-eastern regions do not show significant variability at time scale greater than 4yr (Figure 1.10a-b).

In summary, different regions, coherent in discharge variability, have been identified, and describe critical scales. Critical scales of homogeneous discharge variability have considerably different spatial extension, for instance South-eastern region (#CL5-Q, yellow) covers only 726km² of catchment, while Centre-western region (#CL4-Q, green), covers more than 25000km² (Figure 1.9a). As in precipitation and temperature, most regions seem delineated by orography (cf. Figure 1.1b), except for north-western watersheds.

2.3.2 Cross-scale interactions

Figure 1.11 shows cross-scale interactions for each cluster of discharge variability identified in section 2.1.1.

As shown in Figure 1.11a, North-western watersheds are characterized by a quasi-self-interaction between 6.5-7yr and 6yr time scales (Figure 1.11a). North-eastern watersheds show phase-phase causality of the 4-7yr on the 2-4yr time scales, and of the 3-5yr on 7-8yr time scales (Figure 1.11a), similarly than in precipitation (Figure 1.5a). Bi-direction interaction also occurs between 6-7.5yr and 8yr time scale in the North-eastern regions (Figure 1.11a). The specificity of the north-eastern watersheds' wavelet spectra (cf. Figure 1.10a-b) probably result from the complex phase interactions between the different time scales. Centre-western watersheds displays phase-phase causality of the 4-5yr scale on the 2yr, 3.5yr and 5yr time scales (Figure 1.11a). As in precipitation (Figure 1.5a), south-eastern regions show phase-phase causality of the 2, 4 and 5-8yr scales on the 4-5yr time scale (Figure 1.11a). South-western watersheds show phase-phase causality of the 4yr on the 7-8yr time scales. Meanwhile, north-centre watersheds do not show any phase-phase causality (Figure 1.11a).

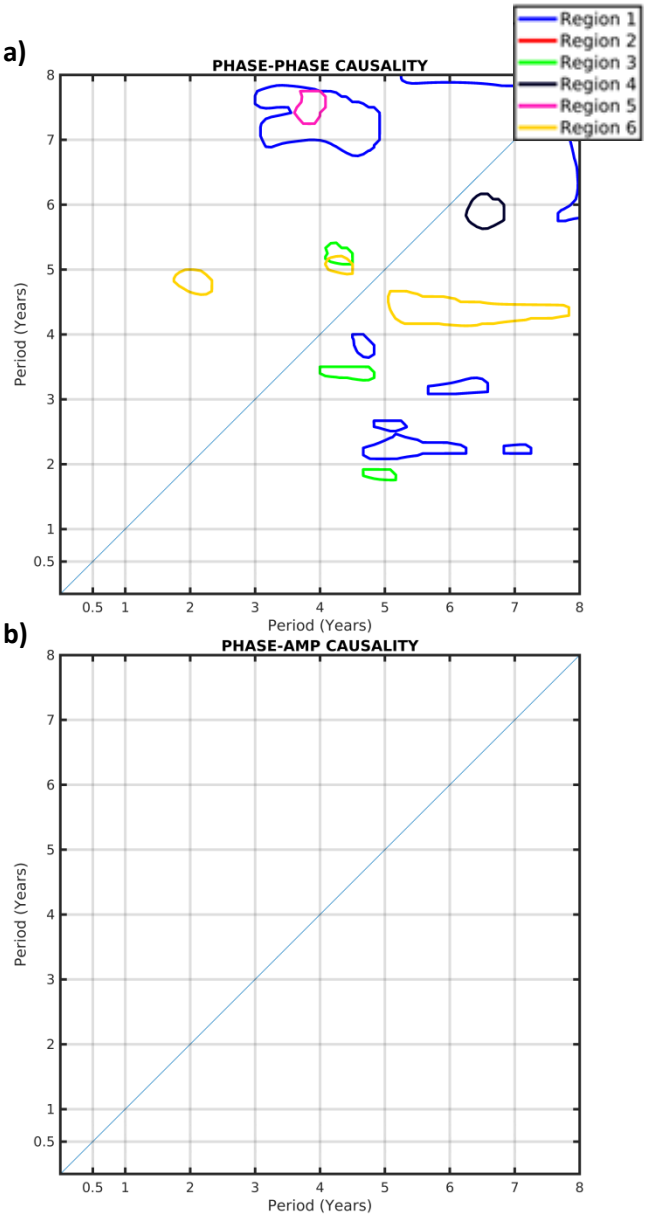

Figure 1.11. Discharge cross-scale interactions. *The driving scale is on the horizontal axis, the driven on the vertical axis. a.) Phase-phase causality; b.) Phase-amplitude causality.*

Interestingly, discharge does not show any phase-amplitude causality, even at lower significance level (Figure 1.11b). The reason why this happens should be further investigated in future studies, but could not be fully addressed here. Nevertheless, as watershed characteristics modulate the incoming climate signal (*i.e.* precipitation and temperature), one could think of a "decoupling" between input precipitation and discharge. However, comparison between Figures 1.8a and 1.11a shows that several phase-phase interactions are

transferred from precipitation to discharge (*e.g.* north-western and south-eastern watersheds). As a consequence, it seems that the selected watersheds, which have very low groundwater support, only modulate the incoming climate signal in amplitude. This modulation will also be different from one time scale to another and, thus, for cross-scale interactions.

The cross-scale interactions are only of phase-phase nature in discharge. Those interactions can be uni- or bi-directional. In addition, as in precipitation and temperature, such cross-scale interactions are different in all regions, suggesting different internal dynamics.

3. Discussion and Conclusion

As recommended in Blöschl et al. (2019), studying spatial, temporal scales and their interactions is one of the most important challenges in hydrology to date. In this study, we unravelled the critical spatial scales of homogeneous non-stationary and non-linear hydroclimate variability in France. We ran a clustering analysis of precipitation, temperature and discharge variability over 152 watersheds in France. The clustering analysis is based on scale-time patterns of each watershed aggregated time series, for each variable. We then studied the spatiotemporal characteristics of each homogeneous region, including an in-depth exploration of the internal dynamic of the system using study cross-scale causality interactions (*i.e.* phase-phase and phase-amplitude couplings).

Our study reveals different critical scales of coherent regions in precipitation, temperature and discharge variability: Precipitation and discharge homogeneous regions' total area are very variable, ranging from the less than a thousand square kilometres, to all most thirty thousand. Temperature on the other hand is more uniform, with scales ranging from a thousand five hundred, to ten thousand five hundred. Overall, discharge variability displays intra-seasonal (<1yr), annual (~1yr) and inter-annual (2-4yr and 5-8yr) timescales, which is consistent with

the study by Labat (2006) over the world's major rivers. Those coherent regions are homogeneously distributed over France in precipitation and discharge, but show large discrepancies in term of spatial extension in temperature. This result contrasts with previous clustering of hydroclimate variability over France, showing more heterogeneous regions in Southern France than in the North (Champeaux and Tamburini 1996; Sauquet et al. 2008; Snelder et al. 2009; Joly et al. 2010). In addition, we show that both the amplitude and timings of the different time scales of variability differentiate clusters. This is thus highlighting the importance of accounting for changes in both amplitude and timing of all time scale when characterising hydroclimate variability.

Looking at the internal dynamic of each coherent region, based on phase-phase and phase-amplitude causality, complex interactions have been identified. Those interactions can be orientated from larger (smaller) to smaller (larger) time scales, uni- or bi-directional (implying feedbacks) and even on themselves. In addition, we have shown that, for very similar scale-time patterns, the cross-scale interactions were very different, implying different internal dynamic.

Interestingly, discharge variability does not show any phase-amplitude causality, while such interactions were significant in precipitation and temperature. In contrast, phase-phase interactions, which were found in precipitation, are identified in discharge. Phase-amplitude couplings are highly dependent on the topology of the different physical components, and is enhanced by indirect connections between those components and other cross-scale interactions (Sotero 2016). Thus, a potential explanation, in the context of our watersheds (with low groundwater support), would be that spatial interactions (here referring to indirect connections) existing in precipitation are either modified or destroyed by the watershed characteristics. This should be further explored in future studies, as it could be crucial for

precipitation-discharge forecasting system. The results from this study are thus directed to both hydrologists and climatologists, focusing on climate change impact on water resources.

PART II: SPATIOTEMPORAL SCALES OF LARGE SCALE HYDROCLIMATE VARIABILITY

Introduction

Human activities are tied to water resources in many sectors (e.g. industrial, energy and food production, natural hazards, recreational). In the context of climate change, it is crucial to understand the driver of hydrological variability at local (*e.g.* precipitation and temperature over the watershed area) and large scales (e.g. ocean-atmospheric dynamics), to improve future water management scenarios (IPCC 2007, 2014).

Previous studies have shown that hydrological variability fluctuates at different spatial and temporal scales (Coulibaly and Burn 2004; Kingston and Hannah 2006; Labat 2006; Fritier et al. 2012). However, local and large-scale climate processes linked to that variability are not well understood (Kavvada et al. 2013; Dieppois et al. 2015, 2019). Because of the complex modulation of the climate input by the catchment properties, the spectral links between precipitation, temperature and discharge have been shown to be both imprinted with non-linearity and non-stationarity (Labat 2006; Massei et al. 2007; Slimani et al. 2009; El Janyani et al. 2012). Nevertheless, in Europe, Gudmundsson et al. (2011) studied the long-term variability of streamflow at time scales (> 1 year), and found consistent links to large-scale atmospheric processes in discharge, precipitation and temperature, but not between fractions of variance expressed in these three variables. Studying southern Africa, Dieppois et al., (2016) show that rainfall fluctuates at three different time scales in response to variations in large-scale sea-surface temperature. In France, Boé and Habets (2014) highlighted multi-decadal variability of river flows linked to climate patterns such as the Atlantic Multidecadal Oscillation, in particular in spring. Those multidecadal fluctuations in River flows, in France, have also been shown to significantly modulate climate change impacts (Boé and Habets 2014; Dieppois et al. 2016a), consistently with the regional impact of internal climate variability (Hawkins and Sutton 2009; Deser et al. 2012; Wills et al. 2018). Similar results were found all over Europe in (Hannaford et al. 2013). In addition, Massei et al. (2017), using

empirical statistical downscaling technique (Benestad et al. 2002) on the Seine River flow, demonstrated better prediction skills when tracking predictors at multiple time scales. Massei et al. (2017) thus highlighted that different time scales in hydrological variability were associated with different atmospheric circulation patterns. Building upon Massei et al. (2017), we aim at further understanding both local and large-scale drivers of the critical scales associated with coherent regions of hydrological variability in France (cf. Part I), as well as how those links are investigated. This study explores non-linear and non-stationary linkages between hydrological and climate variability.

After presenting the data and methods used in this study in section 1, in section 2, we study the links between discharge and local precipitation and temperature over six spatiotemporally coherent regions. In section 3, we identify atmospheric circulation associated with discharge variability at different time scales, using composite analysis. Using a new spatial spectral similarity and coherence analysis, we then explored whether the composite atmospheric patterns were consistent with the regions of greatest spectral similarity, and with the regions of greatest correlations, *i.e.* potential greater predictability skills, at different time scales in sections 4 and 5.

1. Data and methods

1.1. Hydrological Data

Discharge time series come from the observation dataset introduced by Bourgin et al. (2010a; 2010b). This data set is composed of 4496 watersheds and their main river daily time series and is accompanied with hydrologic descriptions of each watershed. This data set was subset to low anthropogenic influenced and low groundwater support watershed which accounts for 662 stations. We further reduce the data by keeping only continuous time series from January

1968 to December 2008. This results in 152 watershed stations. Figure 2.1a shows the locations for the 152 stations with their respective river.

Six regions of homogeneous scale-time variability were identified (Figure 2.1b; cf. Part I, Figure 1.9). We took the average time series of each region as the base data set for this study. The six regions are identified as follows: North-western (#CL1-Q, black), North-eastern (#CL2-Q, blue), North-centre (#CL3-Q, red), Centre-western (#CL4-Q, green), South-eastern (#CL5-Q, yellow) and South-western (#CL6-Q, pink).

a) **b)**

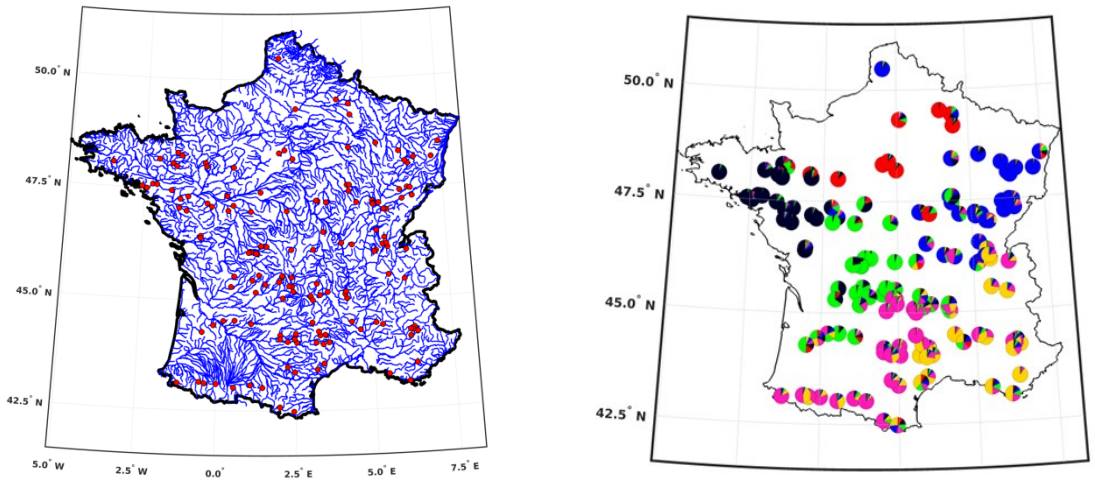

Figure 2.1. Research area and regions of homogenous discharge variability. *a) Location of stream gauges (red dots) and their respective networks (blue lines) stations location; b) Regions of homogeneous discharge variability as defined in Part I, Figure 1.9.*

1.2. Climate Data

Local climate data, *i.e.* precipitation and temperature, were extracted from the SAFRAN reanalysis data set ("Systeme d'Analyses Fournissant des Renseignements Adaptes à la Nivologie"; Vidal et al. 2010). This data set is formatted as a regular grid of 8 kilometers spaced nodes that covers metropolitan France. Data start in August 1958, and are updated as

new data are available. For this study, we averaged the monthly to annual data, subset to the 1968-2008 period and spatially average within each watershed of the six homogeneous regions (cf. Part I).

Large-scale climate data is inferred using annual geopotential height at 500hPa (z500), which were derived from NOAA's 20CR v2c reanalysis ensemble (Compo et al. 2011). Under the geostrophic approximation, winds are parallel to the iso-geopotential height lines, and this is particularly relevant at 500hPa (Norbury and Roulstone 2002). Data are subset to the 1968-2008 period for consistency with the hydrological data set, and to the Euro-North Atlantic regions (100°W-40°E and 5°S- 80°N; Figure 2.1c). The 20CR v2c reanalysis ensemble contains 56 members, which allow for quantifying the model induced dispersion. Prior to this study, we ran a dispersion analysis showing that from 1950's, taking the average member is robust, as the member dispersion greatly decreases from this decade (not shown) While this may not be sufficient to guarantee low model internal variability, it at least guarantees no averaging effects that would lead to biased variability (Hingray et al. 2019).

1.3. Methods

Figure 2.2 shows the generic workflow of our analysis. First, we study the non-stationary spectral correlation between discharge and its local climate drivers, *i.e.* precipitation and temperature, which gives an indication spectral modulation the catchment characteristics exerts on the local climate input (Figure 2.2, (a-b)).We then study discharge and large-scale climate links. First, we reconstruct both precipitation, discharge and large-scale climate data at 2-4, and 5-8 years' time scales, using multiresolution analysis (Figure 2.2, (c)), then, we study what are the climate patterns associated with dry and wet periods of precipitation and discharge (Figure 2.2, (d));

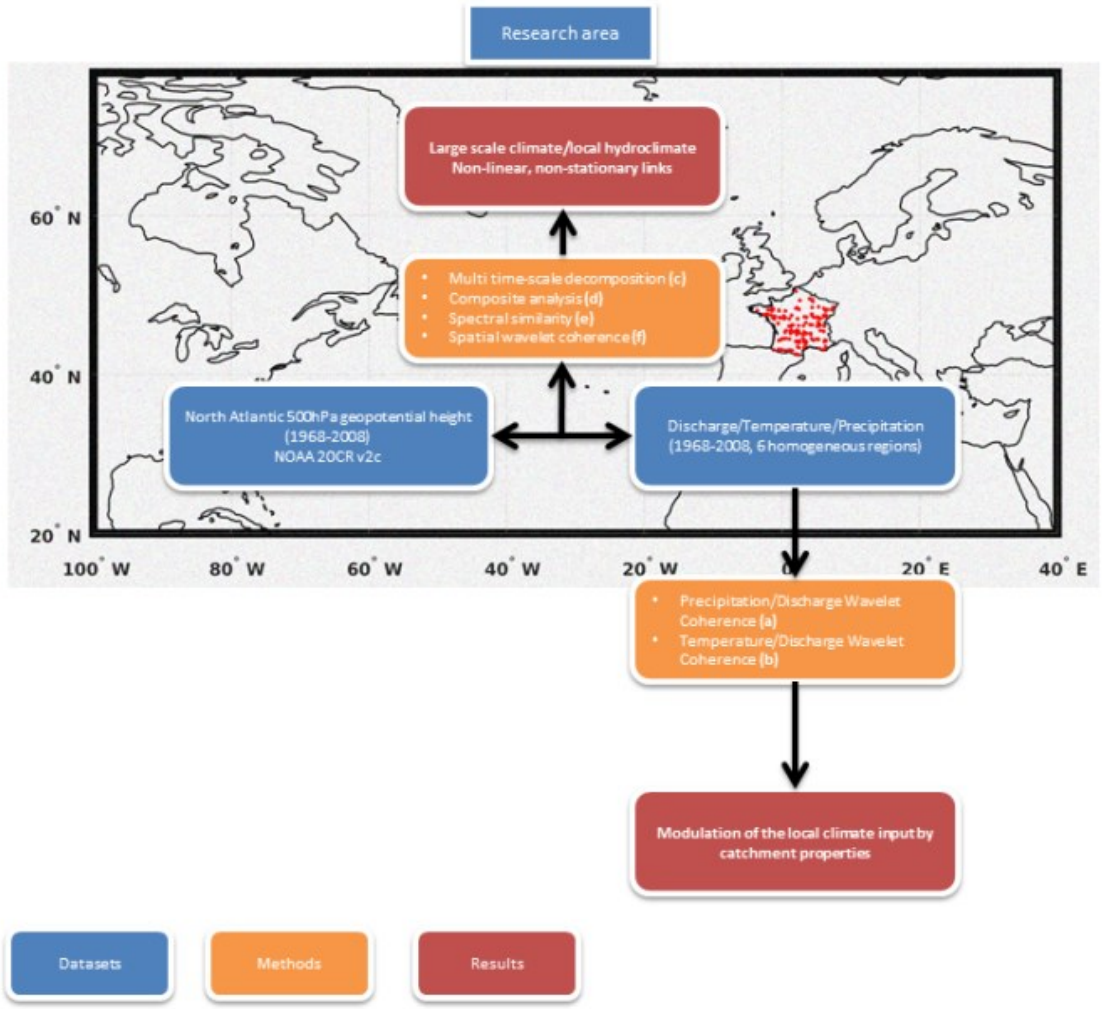

Figure 2.2. Workflow of this study. *a.) The non-stationary spectral correlation between precipitation and discharge is computed; b.) Same as a), but between temperature and discharge; c.) Hydroclimate data is reconstructed at 2-4, and 5-8 years' time scales; d.) The composite analysis of precipitation and discharge, shows the patterns of z500 that are associated with large variations in either precipitation or discharge; e) Location of the z500 showing similar spectral characteristics than precipitation and discharge are computed; f) The non-stationary correlation between z500 patterns and precipitation and discharge are computed.*

Using the non-decomposed precipitation and discharge time series, we search in the large-scale climate data, pattern that present similar spectral characteristics to precipitation and discharge's ones (Figure 2.2, (e)). Finally, we study the, large-scale climate, coordinate dependent, non-stationary spectral correlation between precipitation, discharge, and large-scale climate data (Figure 2.2, (f)).

1.3.1. Continuous Wavelet Transforms and Wavelet coherence

Continuous wavelet transforms, and wavelet coherence, are used to compute the scale-time correlation between discharge and local climate variables (Figure 2.2,(a-b), (e-f)). Both wavelet analyses are also applied to each grid-point of z500. The theory behind continuous wavelet transform has been presented in Part I, section *1.2.1*. Wavelet coherence can be interpreted as a scale-time location correlation coefficient between two wavelet spectra (Torrence and Compo 1998; Labat et al. 2000).

1.3.2. Multiresolution analysis

Multiresolution analysis is used as a first step in the discharge-z500 composite analysis, to reconstruct the discharge and z500 data at selected time scales (Figure 2.2, (c)). Multiresolution analysis is the combination of a discrete wavelet transform analysis (*i.e.* decomposition of the signal into discrete wavelet coefficients) and a synthesis (*i.e.* reconstruction of the signal at each time scale; Percival and Walden 2000). Discrete wavelet transforms are based on Equation 1 (cf. Part I-*1.2.1.*), with a slightly different algorithm. The signal is not decomposed by convolution, but by a series of orthogonal filter banks in dyadic time scales that represent the wavelets (Percival and Walden 2000). Increasing the scales, the signal is downsampled by a factor of two, to prevent shift overlap. The downsampling can however lead to a loss of shift invariance. Since translated filters are placed at scale spaced locations (to prevent overlap), oscillations from the signal may not be aligned with each filter

location, leading to under or overestimate the variability (Percival and Walden 2000). For this reason, we decided to use the Maximum Overlap Discrete Wavelet Transform (MODWT), with a base wavelet 'sym4' (Percival and Walden 2000). The main difference is that the signal is not downsampled as the scales increase, so the initial time step of the signal is used for all scales. Naturally, the shift independence is lost, but shift invariance is preserved.

1.3.3. Image Euclidean Distance Calculation

Image Euclidean Distance Calculation (IEDC) is used to compute the similarity between discharge scale-time patterns, and those of z500 (Figure 2.2, (e)). It has been detailed in Part I, section *1.2.2.*

1.3.4. Composite analysis

The composite analyses are used to construct mean-state of the North Atlantic atmospheric circulation associated with streamflow variability (Figure 2.2, (d)), as in (Dieppois et al. 2016b, 2019; Massei et al. 2017; Sidibe et al. 2019). Two sets of z500 are produced for each timescale (*i.e.* 2-4 and 5-8 years), where streamflow fluctuations exceed ± 0.8 standard deviation (*i.e.* wet and dry conditions); the resulting composites thus describe the difference in z500 between hydrological wet and dry conditions. Statistical significance has been estimated by testing the difference in mean between wet and dry z500 conditions using a two-sided Student's t test at $p = 0.05$. However, we elected to remove the significance contours of plots, due to energy biases in statistical significance tests when the signal has been reconstructed by wavelets (Maraun et al. 2007). For readability, we will talk of in-phase (anti-phase) composite, when positive (negative) z500 are associated with wet hydrological conditions.

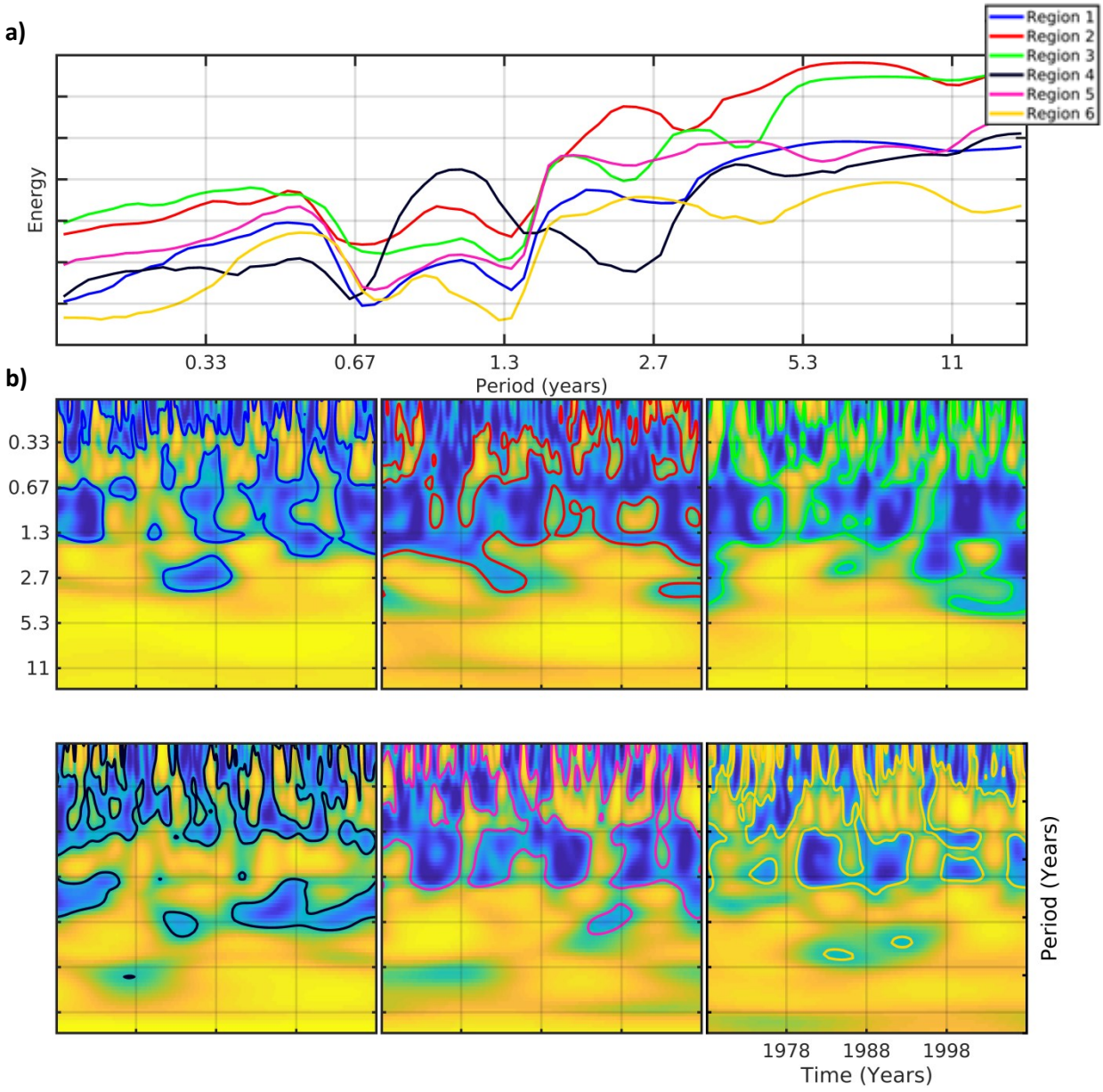

Figure 2.3. Precipitation-discharge wavelet coherence. *a) Global wavelet coherence spectra for each region shows the energy associated with each time scales' correlation; b) Wavelet coherence spectra for each regions, iso-lines colours are those of regions.*

2. Links between discharge and local climate variables

Wavelet coherence of discharge with precipitation and temperature has been computed for each region, as defined in Figure 2.1b.

2.1. Discharge-precipitation

Global discharge-precipitation wavelet coherence spectra show significant relationships over time scales ranging from intra-seasonal to inter-annual (6 months to >2yrs; Figure 2.3a). While all clusters display significant correlation from ~2 to 8yr time scales (5-8yr time scale in North-western regions), large differences emerge at shorter time scales in terms of amplitude and timing (Figure 2.3a). For instance, while for most regions coherence is sparse at the annual time scale, north-western watersheds show continuous significant relationship between discharge and precipitation (Figure 2.3b). South-eastern watersheds are characterized by almost continuous and strong correlation at intra-seasonal scale (Figure 2.2a). Impact of precipitation on streamflow variability thus appears homogeneous for all regions at inter-annual scale. At shorter time scales, however, links between discharge and precipitation are region-dependant.

2.2. Discharge-temperature

Global discharge-temperature wavelet coherence spectra are displayed in Figure 2.4a. Correlations span intra-seasonal to inter-annual time scales (Figure 2.4a). Clusters however differ both by the occurrence of significant correlation at certain time scales, and certain periods of time (Figure 2.4b). For instance, at the annual time scale, while continuous significant links are found in north-eastern, north-western and centre-eastern regions, no significant correlations are identified in the mid 1990's over the centre-western, south-eastern and south-western watersheds (Figure 2.4b).

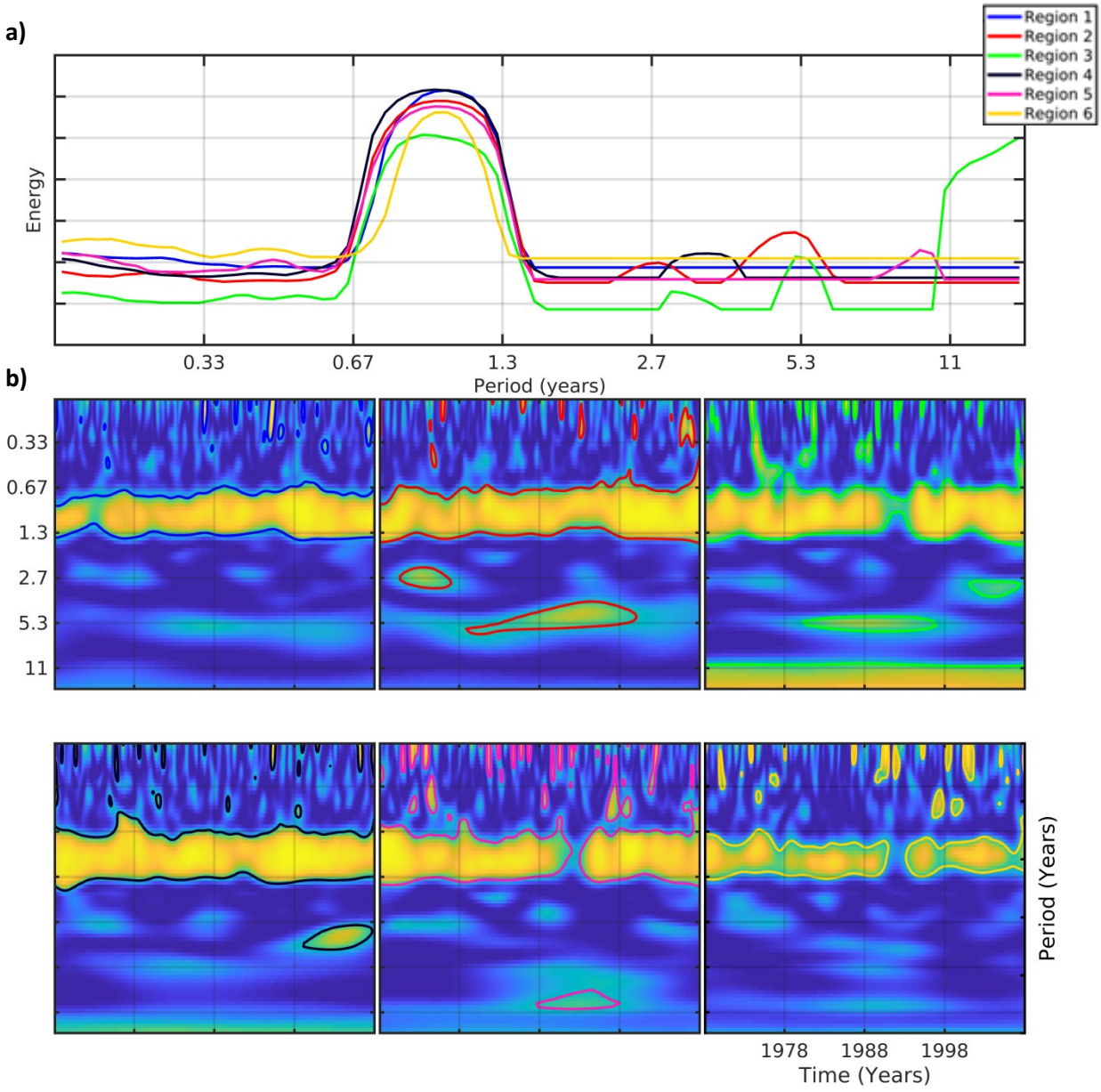

Figure 2.4. Same as Figure 2.3 but for temperature-discharge.

North-eastern and south-eastern regions do not show significant correlation at inter-annual scale (Figure 2.4b). North-western and Centre-western watersheds show significant correlation to temperature at the 2-4yr' time scales at the end of the time series, while correlation at the same time scale only occur in North-centre regions, but at the beginning of the time series (Figure 2.4b). Significant correlations are also found at 5-8yr' time scales between the 1980's and 1990's, over the North-centre, Centre-western, South-Western regions (Figure 2.4a).

In summary, differences in the links between discharge and temperature are identified at annual and inter-annual time scales. Those discrepancies also split the country in two areas: North-South at annual time scales, and E-W at inter-annual time scales. Comparing both the discharge relationship with precipitation and temperature, the more important contribution of precipitation variability to inter-annual fluctuations in discharge over France, at least at certain period of time, is suggested.

3. Links with large-scale climate variability

Section 3 shows the composite states of z500 associated with precipitation and then with discharge variability at both 2-4yr and 5-8yr time scales. For each scale, we computed the composite maps of each cluster with geopotential height.

The mean North Atlantic atmospheric circulation is largely influenced by the interface between poleward warm air and equatorward cold air, about the eastward mid-latitude jet. This place of exchanges, as well as the influence of baroclinic conditions, and topography, shapes the anomalous patterns that can be observed at time scales, ranging from daily to millennia (Ghil and Lucarini 2019). Some types of patterns seem more stationary than other (more details in Part III), among them, two types: zonal and blocking. Zonal patterns describe westerly winds patterns with limited waviness in the path of the mild-latitude jet, while blocking refers to zone of high pressure that forces the jet to turn around. The most common examples of zonal and blocking patterns are the positive phase of the North Atlantic Oscillation, and the Atlantic ridge, respectively (Cassou et al. 2004).

3.1. Z500 composite at 2-4yr time scale

Figure 2.5 shows z500 composite maps associated with precipitation variability at the 2-4yr time scales. Except for South-eastern watersheds, 2-4yr precipitation variability is associated with four centres of actions (Figure 2.5): two in-phase centres South of Greenland and over

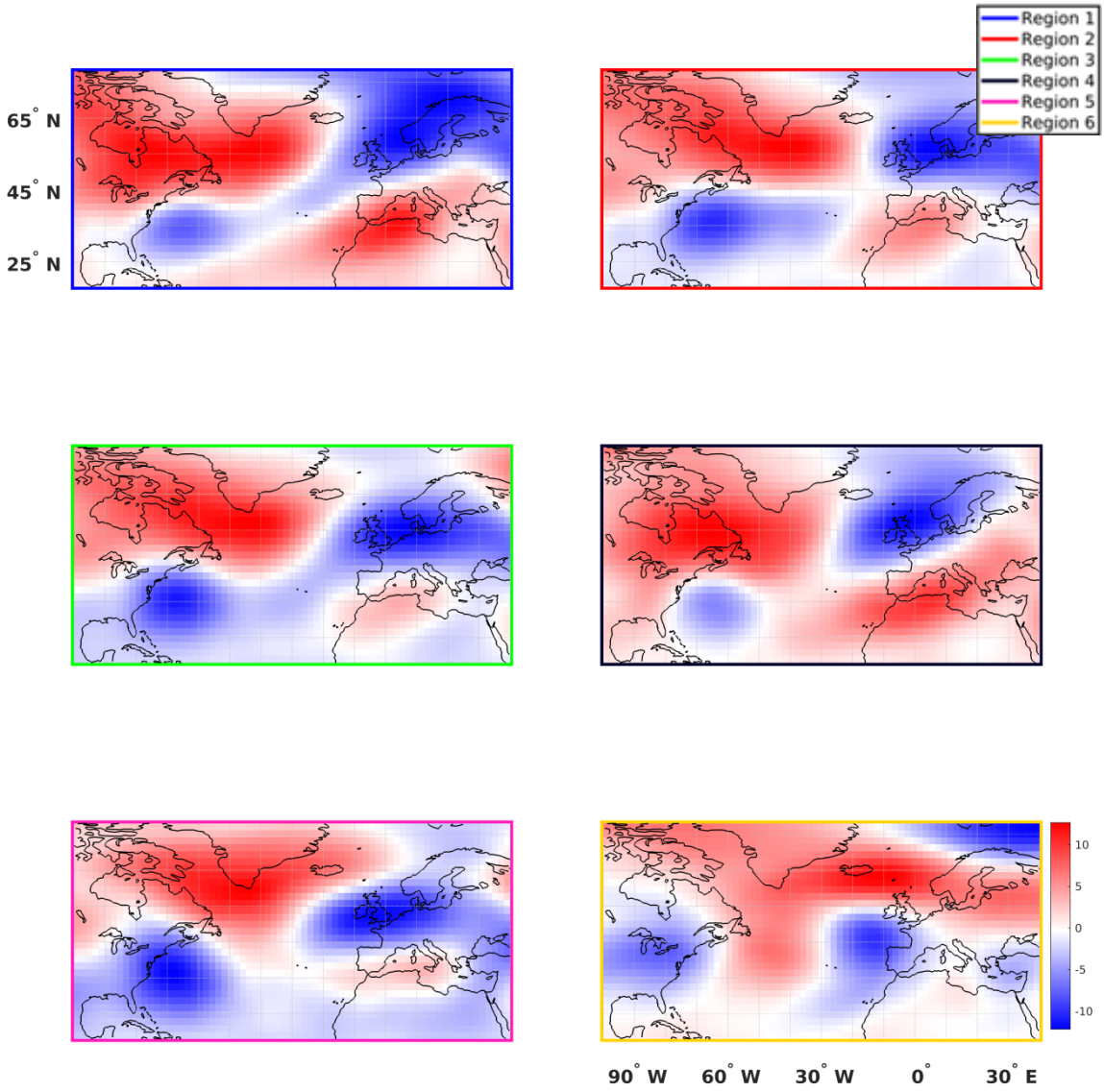

Figure 2.5. 2-4yr' time scales composite precipitation analysis. *Colours show how much z500 patterns differ between wet and dry precipitation periods.*

the Mediterranean Sea, and two out-of-phase centres off North American east coast and over northern Europe. This atmospheric pattern describes eastward shift of the Icelandic Low and the Azores High, as well as an enhancement in the meridional atmospheric pressure gradient over Europe (Figure 2.5), which is consistent with a northward shift and an enhancement of the westerlies favouring wet conditions there. This enhanced meridional atmospheric pressure gradient is however more (less) pronounced in the Northern (Southern regions; Figure 2.5). In the South-East cluster, weaker meridional atmospheric pressure gradients are detected between northern Europe and the Mediterranean (Figure 2.5). Weaker meridional z500 gradients are consistent with a southward shift of the westerly track, favouring wet conditions in southern Europe (Hurrell 1995; Cassou et al. 2004; Deser et al. 2017).

Very similar atmospheric circulation patterns are associated with discharge variability (Figure 2.6), suggesting than both precipitation and discharge variability at 2-4yr time scale derive from the same large-scale atmospheric processes. Some modulations of the intensity of the different centre of actions are however identified (Figure 2.6), and highlight watershed characteristics to filter some part of the incoming climate signal. North-centre region shows more modulation between precipitation and discharge, than other regions (Figure 2.5, 2.7, #CL3-Q, red).

3.2.Z500 composite at 5-8yr time scale

Figure 2.7 displays z500 composite maps associated with precipitation variability at the 5-8yr time scales. Four centres of actions are also associated with 5-8yr precipitation variability in North-centre clusters (Figure 2.7), and describe an eastward shift of the Icelandic Low and the Azores High, as well as an enhancement in the meridional pressure gradient over Europe. The centre of action centred on the Mediterranean Sea is much weaker in the North-eastern regions, and disappears in North-western, Centre-western and South Western clusters (Figure

2.7). A weakening of the atmospheric pressure gradient over the western North Atlantic is then associated with eastward shift of the Icelandic Low clusters (Figure 2.7), promoting low pressure and wet conditions over those regions. In the South-East cluster, weaker meridional atmospheric pressure gradients are detected over the entire Euro-North Atlantic region (Figure 2.5), in accordance with a southward shift of the westerly track, and wet conditions in southern Europe (Hurrell 1995; Cassou et al. 2004; Deser et al. 2017).

In discharge, very similar atmospheric circulation patterns are identified (Figure 2.8), suggesting than both precipitation and discharge variability at 5-8yr time scale derive from the same large-scale atmospheric processes.

Interestingly, these atmospheric circulation patterns are slightly different at 5-8yr time scale than at 2-4yr time scale (Figures 2.5-8). For instance, in most clusters, the impact of the Mediterranean centre of action is much less pronounced at the 5-8yr than at the 2-4yr scales. The weakening of the North Atlantic meridional pressure gradient is also more important at the 5-8yr than at the 2-4yr scales Figures 2.5-8). Compared to 2-4yr' time scales, there is no significant modulation between precipitation and discharge' composites.

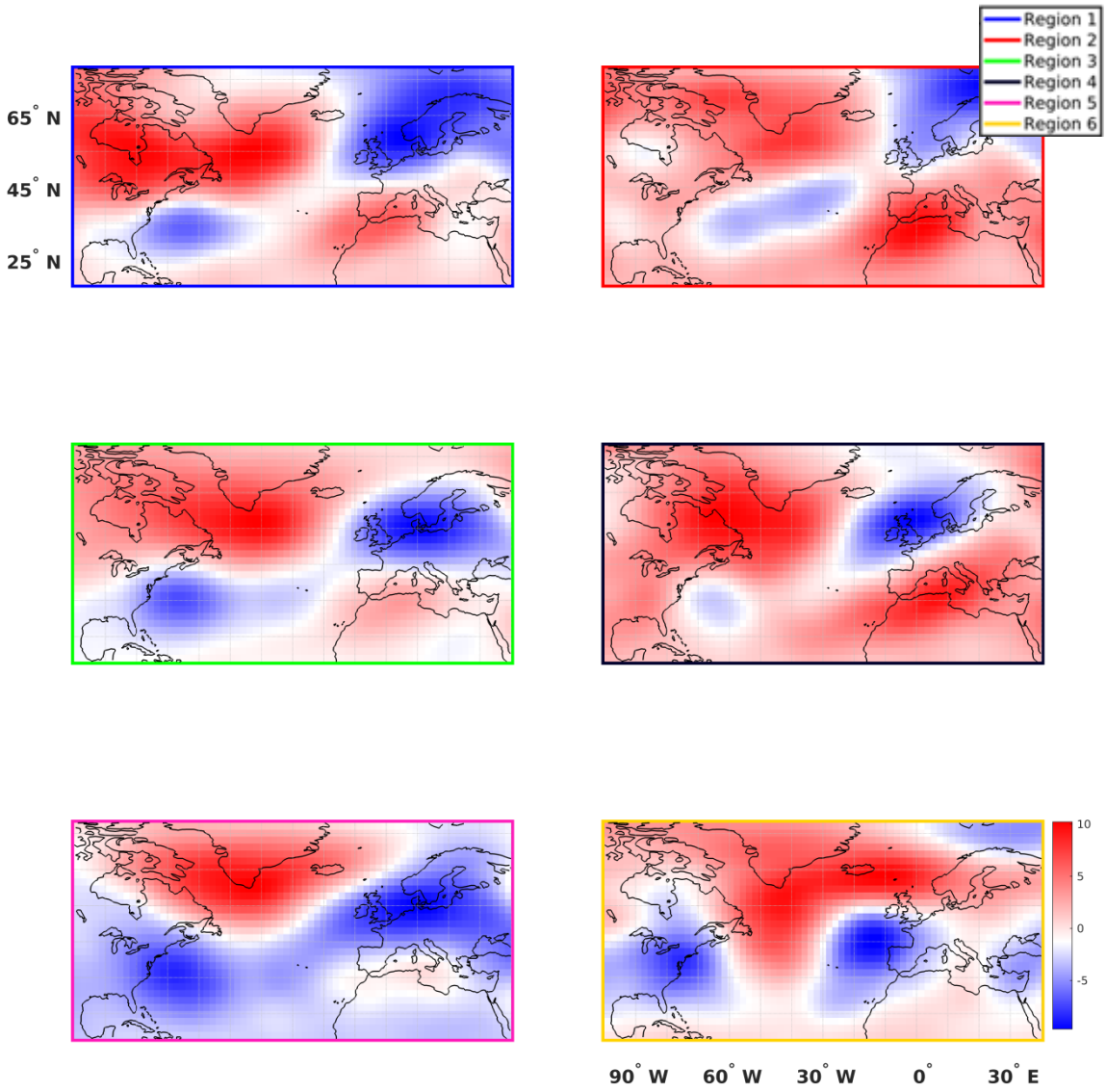

Figure 2.6. Composite analysis. Same as Figure 2.5 but for discharge.

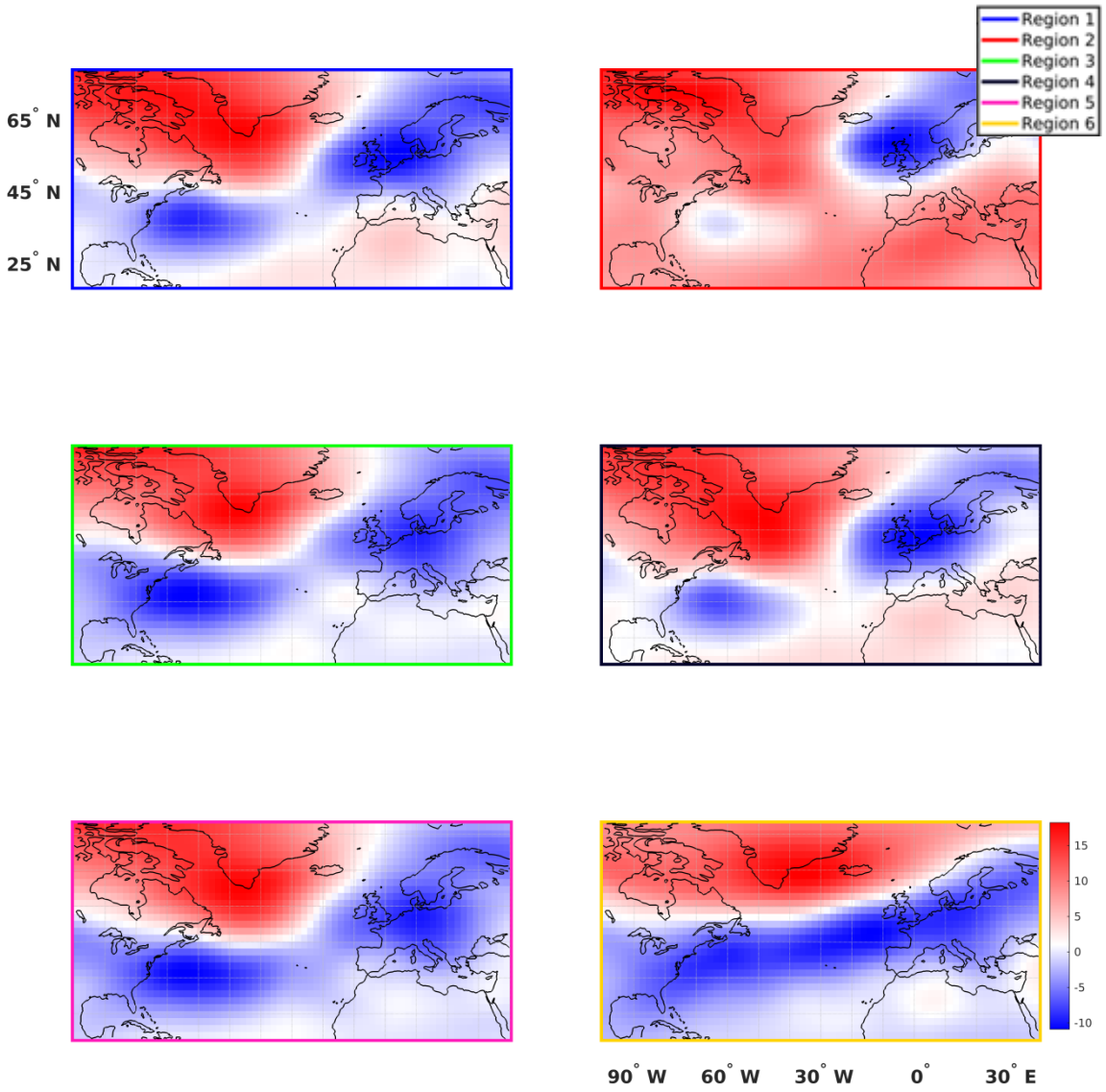

Figure 2.7. Composite analysis. Same as Figure 2. 5 but for 5-8yr' time scales.

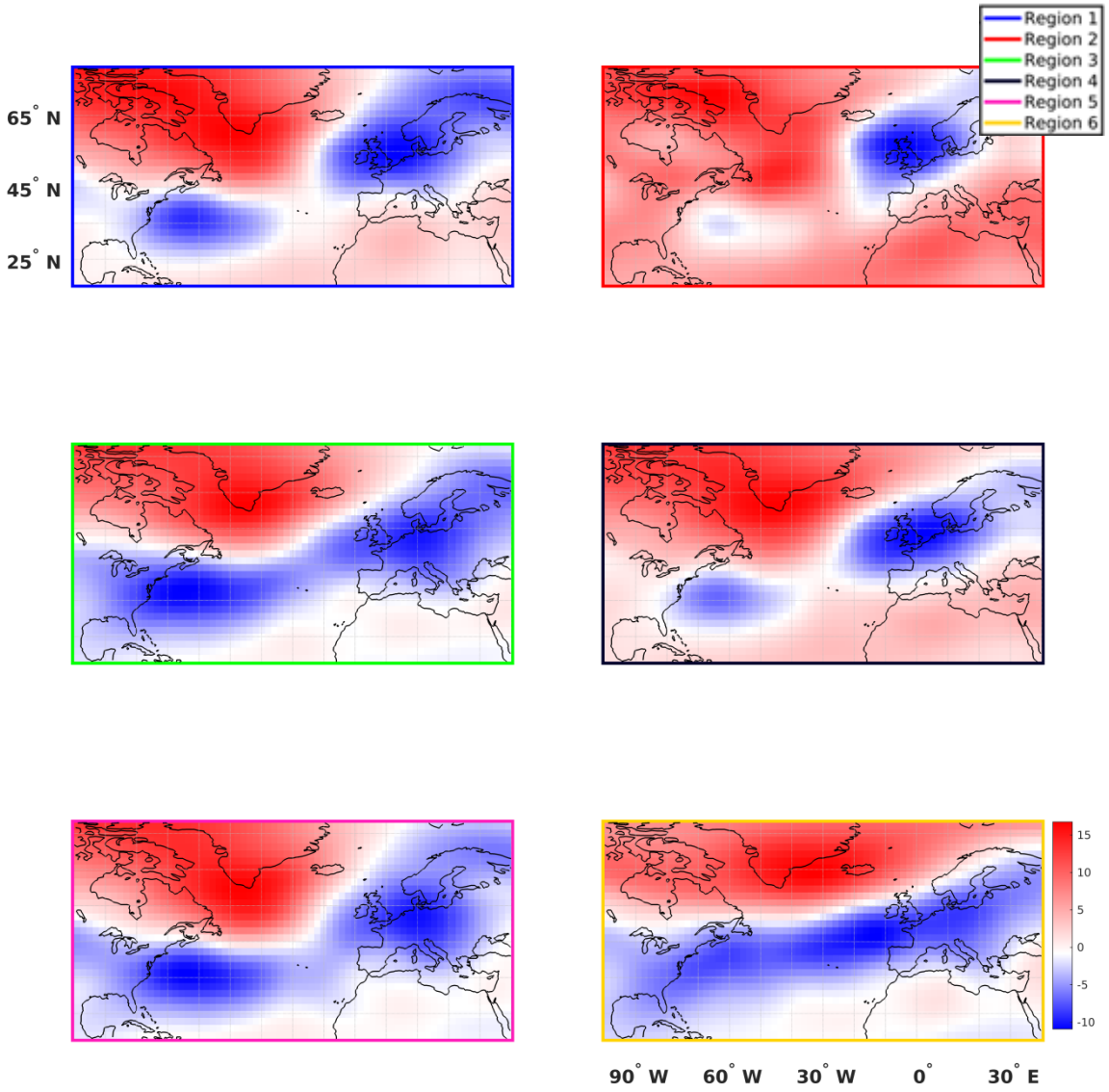

Figure 2.8. Composite analysis. Same as Figure 2.7 but for discharge.

4. Precipitation-Discharge spectral similarity with z500

In this section, we aim at identifying the regions in which atmospheric circulation show similar spectral characteristics (*i.e.* variance, timing at different time scales) to precipitation and discharge variability over the different coherent regions (cf. Figure 2.1b). Similar spectral characteristics in z500 could then be interpreted as potential source of precipitation or discharge variability at all time scales, with quasi-linear relationship. Meanwhile dissimilar spectral characteristics in z500 would relate to non-linear interactions: i) relationship restricted to a single time scale; or ii) non-linear interactions across time scale.

Figure 2.9 shows z500 spectral similarity maps associated with precipitation variability. Precipitation variability in the North-western, North-eastern, North-centre and Centre-western shows strong spectral similarity in z500 over the North Sea, off North America east coast and the great Lakes region (Figure 2.8). Spectral similarity between precipitation and z500 are however more pronounced over the North Sea for the North-centre and -eastern clusters (Figure 2.9). This is consistent with the low pressure centred on the North Sea, favouring wet conditions over those regions (Figures 2.5-8). Precipitation-z500 spectral similarities tend to span over a larger area, including the North Atlantic Ocean, for North-western regions (Figure 2.9). In this region, precipitation-z500 spectral similarities are consistent with the low pressure areas identified over the North Seas and off North America east coast, but not over the Great Lakes, the Atlantic Ocean, the Mediterranean Sea (Figures 2.5-9). Spectral similarity patterns are different in the southern Clusters (South-western and –eastern watersheds), which are particularly pronounced between the sub-tropical North Atlantic and Western Europe regions (Figure 2.9). South-western watersheds also show strong spectral similarities with z500 South of Greenland, while strong spectral similarities are found over Greenland for South-eastern watersheds (Figure 2.9). In South-western regions, precipitation-z500 spectral similarities are consistent with the low pressure located over the sub-tropical

North Atlantic and Western Europe, as well as with the high pressure area identified South of Greenland (Figures 2.5-9). There are however no clear consistency between the z500-precipitation spectral similarity and the associated composite circulation pattern for South-eastern patterns (Figures 2.5-9), suggesting more complex relationships over this region.

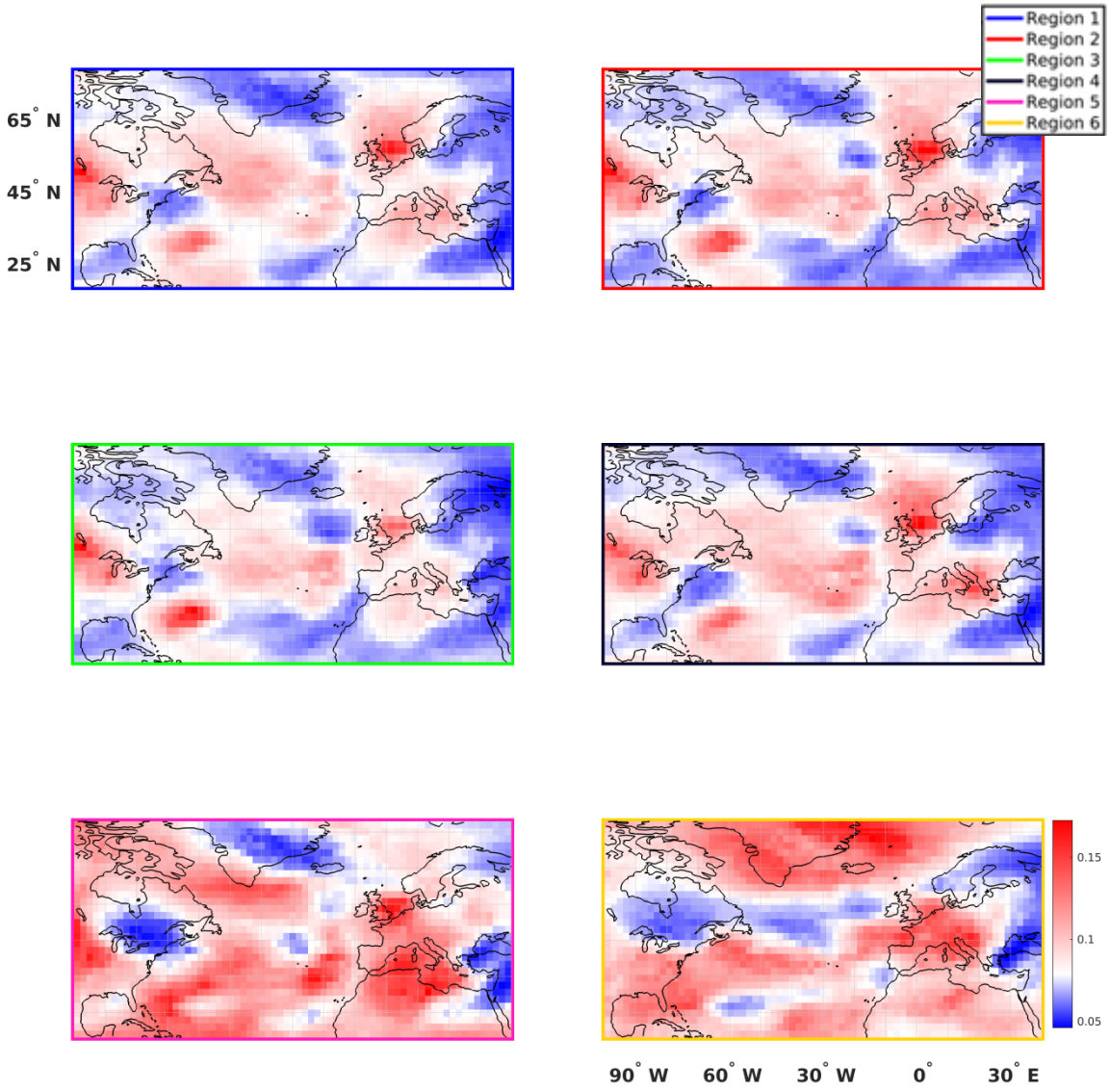

Figure 2.9. Precipitation-z500 spectral similarity. *Patterns' colours show how similar each z500 coordinate's wavelet spectrum, is to each regions' precipitation one.*

As illustrated on Figure 2.10, z500 spectral similarity patterns are very similar in discharge, but with modulations in amplitude differing from one region to another. For instance, in North-western watersheds z500, spectral similarities are more pronounced in discharge than in precipitation (Figures 2.9-10). In South-eastern regions, z500 spectral similarities are less pronounced in discharge than in precipitation over the entire area (Figures 2.9-10).

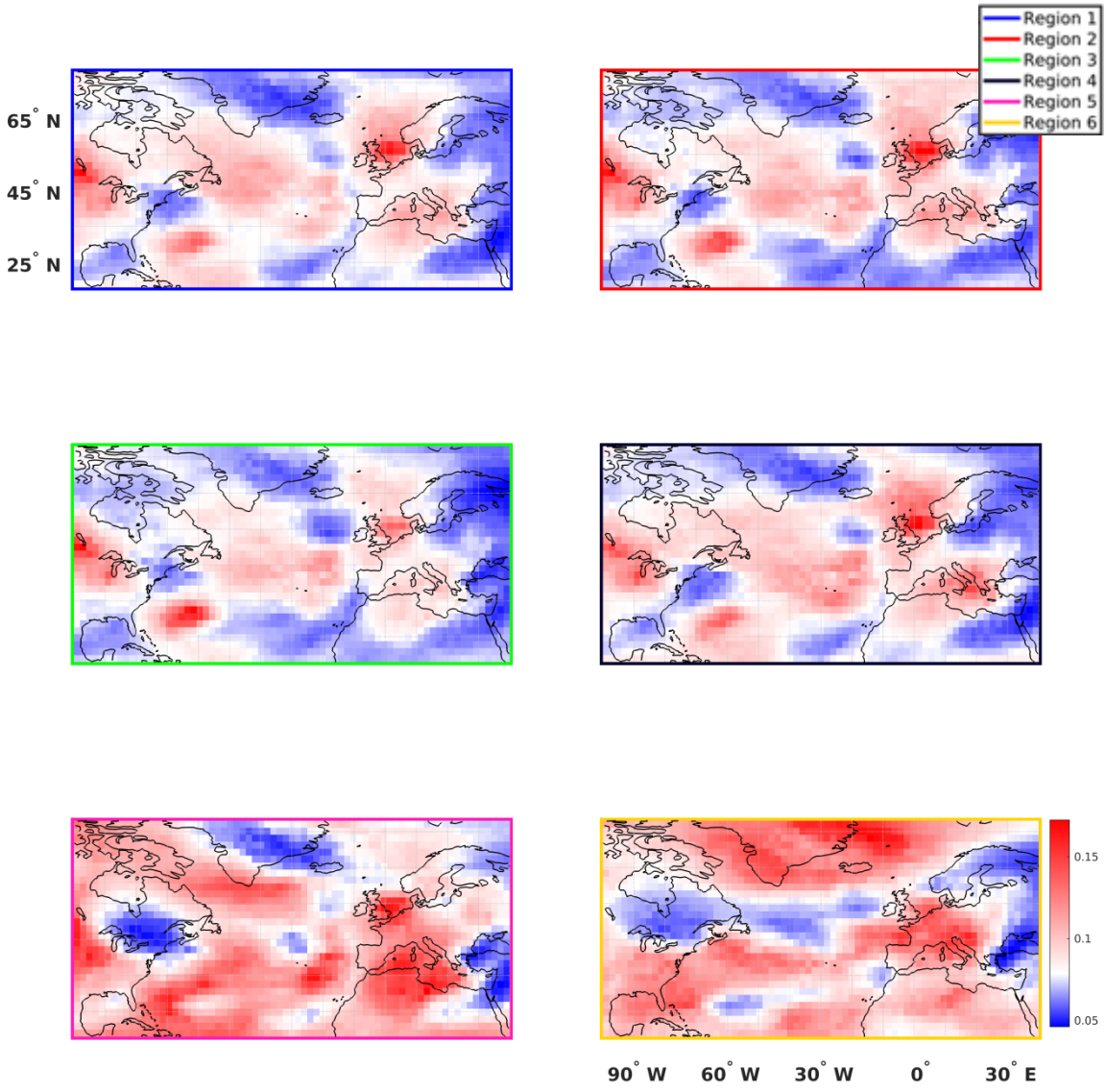

Figure 2.10. Spectral Similarity. Same as Figure 2.9, but for discharge.

Similarly, South-western regions display a decrease (increase) in z500 spectral similarity over Europe (sub-tropical North Atlantic). North-centre and -eastern regions however do not show any modulations (Figures 2.9-10), suggesting weaker impact of the watershed properties.

In summary, hydroclimate variability in northern regions (North-centre and -east) is potentially associated with smaller-scale source of variability than southern and western regions (North-west, Centre-east, south-west and -east). In addition, the impact of watershed properties in modulating the climate signal seem to be greater in North-western and southern regions.

5. **Precipitation-discharge wavelet coherence with z500**

To further explore the links between hydroclimate and the Euro-North Atlantic circulation, this section identifies the region of highest correlation, as well as the contribution of both 2-4yr and 5-8yr time scales. It is also an opportunity to quantitatively identify how much the climate signal is modulated by the watershed properties at both time scales.

Figure 2.11 displays precipitation-z500 wavelet coherence maps. North-centre, North-eastern regions show strong correlation over the North, Norwegian and Mediterranean Seas, and especially over the Atlantic around 50°N (Figure 2.10). These correlations result from both time scales equally in North-centre regions, but are dominant at 5-8yr time scale in North-eastern regions (Figure 2.11). Compared to the composite circulation patterns (Figures 2.5-8), high-correlation areas appear located over the centre of action centred over northern and southern Europe, and in the regions of greatest meridional atmospheric pressure gradient between North America and Europe. Therefore, while spectral similarity patterns suggested smaller-scale source of variability in northern regions, this does not appear to be true in spatial wavelet coherences, which seem to capture the westerly tracks (Hurrell 1995; Cassou

et al. 2004; Deser et al. 2017). Similar patterns are identified for North-western and Centre-western, but with smaller amplitude over the Atlantic (Figure 2.11).

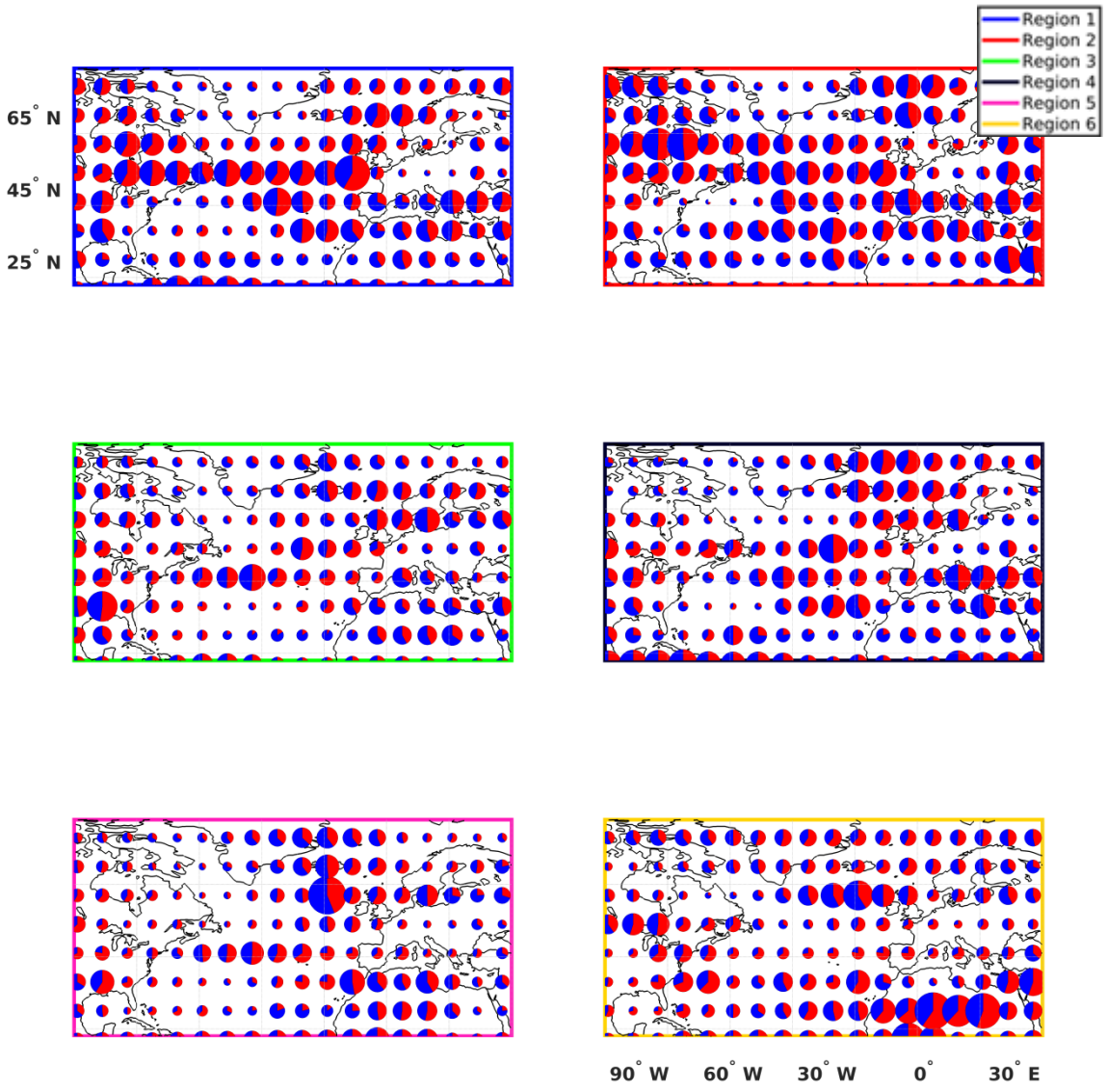

Figure 2.11. Precipitation-z500 wavelet coherence. *Pie charts show the fraction of 2-4 (blue) and 5-8 (red) years' time scales wavelet coherence with each region's precipitation.*

As in the previous section, patterns of discharge-z500 wavelet coherence are very similar than for precipitation (Figures 2.11-12). However, clear modulations of dominant time scales

driving the correlations between the different watersheds and the North Atlantic atmospheric circulation (Figures 2.11-12).

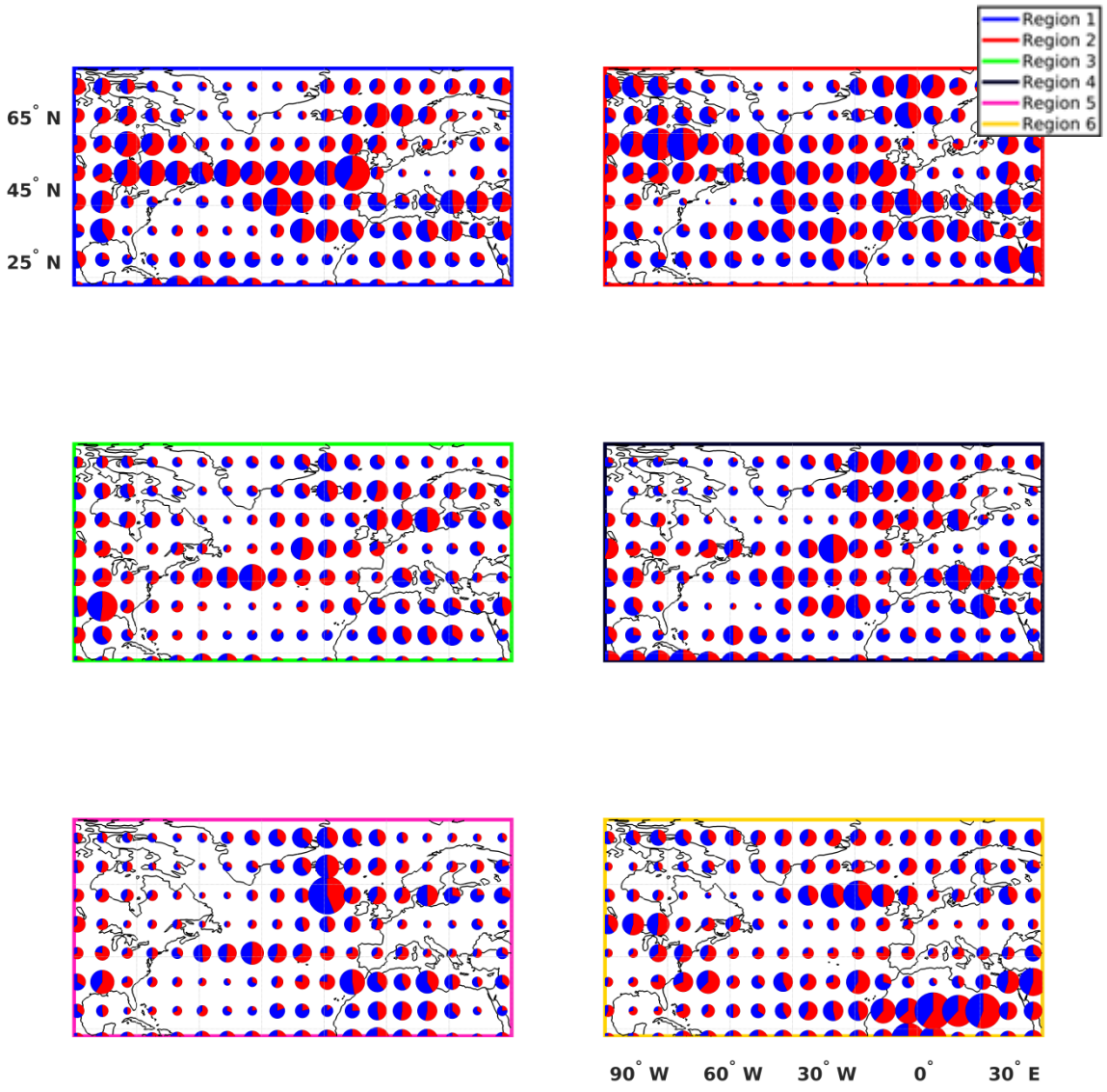

Figure 2.12. Wavelet Coherence. Same as Figure 2.11 but for discharge.

In Southern Clusters, strong correlations are detected, as well as between the sub-tropical Atlantic and North Africa (but slightly further North for the South-eastern than South-western clusters; Figure 2.11). These correlations between Greenland and the British Isles are dominant at 2-4yr time scale for both Southern regions (Figure 2.11), consistently with the regions of greatest meridional atmospheric pressure gradient in the area (Figures 2.5-8). Correlations identified over North Africa are clearly dominant at 5-8yr time scale in South-eastern regions, where significant signal was detected in the composite analysis (Figures 2.5-8), but this is unclear for South-western regions (Figure 2.11).

These modulations are heterogeneous on the different regions of the Euro-North Atlantic atmospheric circulation, and across the watersheds (Figures 2.11-12). In Northern watersheds, z500-discharge correlation shifts toward dominant 5-8yr time scales over the North Atlantic around 50°N (Figures 2.11-12). In Southern regions, z500-discharge correlation shifts towards 2-4yr time scales from 20°N to 50°N (Figures 2.11-12). Compared to precipitation, there are no modulations north of 60°N in northern regions (North-centre and east; Figures 2.11-12).

6. Conclusion

We studied the links between hydrological variability (*i.e*. discharge) and climate at local (*i.e*. precipitation and temperature) and large scales (*i.e*. North Atlantic atmospheric circulation), using non-linear and non-stationary statistical methods.

At the local scale, temperature is the main driver of discharge annual variability (~1yr), while inter-annual discharge variability (>2 yr) is primarily linked to precipitation. Linkages between precipitation and discharge are therefore more stable at inter-annual scale than at annual and intra-seasonal scales (<1yr), and reversely for temperature. Especially, at inter-annual scale, the relationship between precipitation and discharge shows significant

correlations, which are particularly strong at 2-4yr (except for North-western regions) and 5-8yr time scale. Thus, over France, even if the proportions of inter-annual variance between precipitation, temperature and discharge are not correlated, as proposed over Europe in (Gudmundsson et al. 2011b), the fluctuations themselves are. This is consistent with Szolgayova et al. (2014) who suggested that long-term hydrological variability was primarily linked to precipitation over the Danube River watershed. This is also complementing similar results suggested in Massei et al. (2017) over the Seine River watershed, which was over removed from this study due to its large dependence to groundwater support and human activities.

This led us to investigate how the North Atlantic atmospheric circulation (here infered through z500) was linked to precipitation and discharge. According to Gudmundsson et al. (2011), large-scale atmospheric circulation associated with precipitation and discharge variability were similar at 2-4yr and 5-8yr time scales. These linkages between France hydroclimate and large-scale atmospheric patterns however are complex, and differ from one region to another. In the South-East cluster, at both time scales, weaker meridional atmospheric pressure gradients are detected between northern Europe and the Mediterranean Sea, consistently with a southward shift of the westerly track and wet conditions there (Hurrell 1995; Cassou et al. 2004; Deser et al. 2017). In all other regions, atmospheric pattern associated with precipitation and discharge variability are different at both time scales. At 2-4yr' time scales, atmospheric patterns relate to eastward shifts of the Icelandic Low and the Azores High, as well as an enhancement in the meridional atmospheric pressure gradient over Europe, favouring wet conditions there in response to a northward shift and an increase of the westerlies (Hurrell 1995; Cassou et al. 2004; Deser et al. 2017). At 5-8yr time scale, we found a weakening of the atmospheric pressure gradient over the western North Atlantic associated with eastward shift of the Icelandic Low, promoting low pressure and wet conditions over

those regions. Similar results were found in Massei et al. (2017), but over the Seine River watershed.

We then further explored the potential source of precipitation and discharge variability using spectral similarity and wavelet coherence with the North Atlantic z500. Looking at spectral similarity between atmospheric circulation and hydrological variability, we show that, in northern regions, only selected areas, such as the North Sea, show similar scale-time patterns, which, at first, suggested potential smaller-scale source of variability. Wavelet coherence analysis however demonstrates that correlations between z500 and precipitation/discharge could be found at larger spatial scale, but resulting from varying contributions between 2-4 and 5-8yr time scales to the total correlations along the regions of greatest meridional atmospheric pressure gradient between North America and Europe. In southern regions, precipitation/discharge-z500 spectral similarities are found at large spatial scales, consistently with the composite atmospheric patterns. However, for the same regions, using wavelet coherence analysis, regions of greatest correlations at both time scales do not perfectly match. This therefore demonstrates that identifying spectral similarity between discharge, precipitation and large scale climate does not always lead to links between those variables. Similarly, this study also highlights that while composite analysis can help understanding the atmospheric dynamics associated with multiple time scales of variability in precipitation and discharge, greater correlations, *i.e.* predictability skills, are not systematically centred on the centres of actions identified in the composite analysis.

In addition, when comparing results for precipitation and discharge, clear modulations of the climate signals have been identified, and can explain why proportions of inter-annual variance between precipitation, temperature and discharge are not correlated (Gudmundsson et al. 2011b). Such watershed modulations of the climate signals have already been suggested to be linked to the size of the catchment area over Europe (Szolgayova et al. 2014a), and to the

morpho-structual characteristic (shape, geological formation, groundwater support) of the watersheds over the Seine River watershed (El Janyani et al. 2012), and over West and central Africa (Sidibe et al. 2019). These modulations are however heterogeneous on the different regions of the Euro-North Atlantic atmospheric circulation, and across the watersheds.

PART III: DYNAMICS OF THE NORTH ATLANTIC ATMOSPHERIC CIRCULATION, AND HYDROCLIMATE VARIABILITY

Foreword

In previous sections, we have seen that non-linearity could lead to non-unicity of a problem's solution, *i.e.* the same outcome can have different causes. For instance, in Part I, we have shown that while several clusters had similar scale-time patterns, their cross-scale interactions were markedly different. Similarly, in Part II, we have shown that while precipitation, discharge and local climate drivers' scale-time patterns were sometimes similar between clusters, the timing and amplitudes of their correlation were different. The present part will extend that idea by showing that similar North Atlantic atmospheric circulation patterns (so-called "weather patterns"), can result from different dynamics.

In the following, we refer to "dynamics" as the time evolution of a system, the latter being, for the purpose of our study, being defined as a set of N independent generic particles. The evolution in time of the system is described by its equations of motion, which are composed of parameters (dependent on time or not), coordinates, and can have various forms, such as linear or non-linear, first order or higher, ordinary differential or partial differential and so on. The evolution in time of the d-dimensional coordinates of the system's particles is represented in a configuration space, a dN-dimensional manifold. The phase space adds to the configuration space, the velocities associated with each particle at each point in the configuration space. Thus, the evolution in time of the system, its dynamics, can be represented by a function (a trajectory) function of position, velocity, and, implicitly, time. Under this formalism, the equations of motion are described in a purely geometric way, and a bridge between physical laws and geometrical objects is created, a bridge pioneered by the

works of Noether (1971). In a N particles system, the degrees of freedom equals the number of particles, *i.e.* there are N degrees of freedom, which makes description of the dynamics very complex, with the necessity to resort to statistical techniques to describe them. However, if m constraints are applied on the equations of motion, the number of degrees of freedom is reduced to $N - m$ degrees of freedom. A powerful constraint applied on dynamics is that of conserved quantities such as total energy, momentum, angular momentum and so on. When such constraint is enforced on the equation of motion, we get conservation laws. In the geometrical setting, conservation laws are analogue to geometrical symmetries, *i.e.* geometrical transformations that leave a geometrical object invariant (up to some parameter).

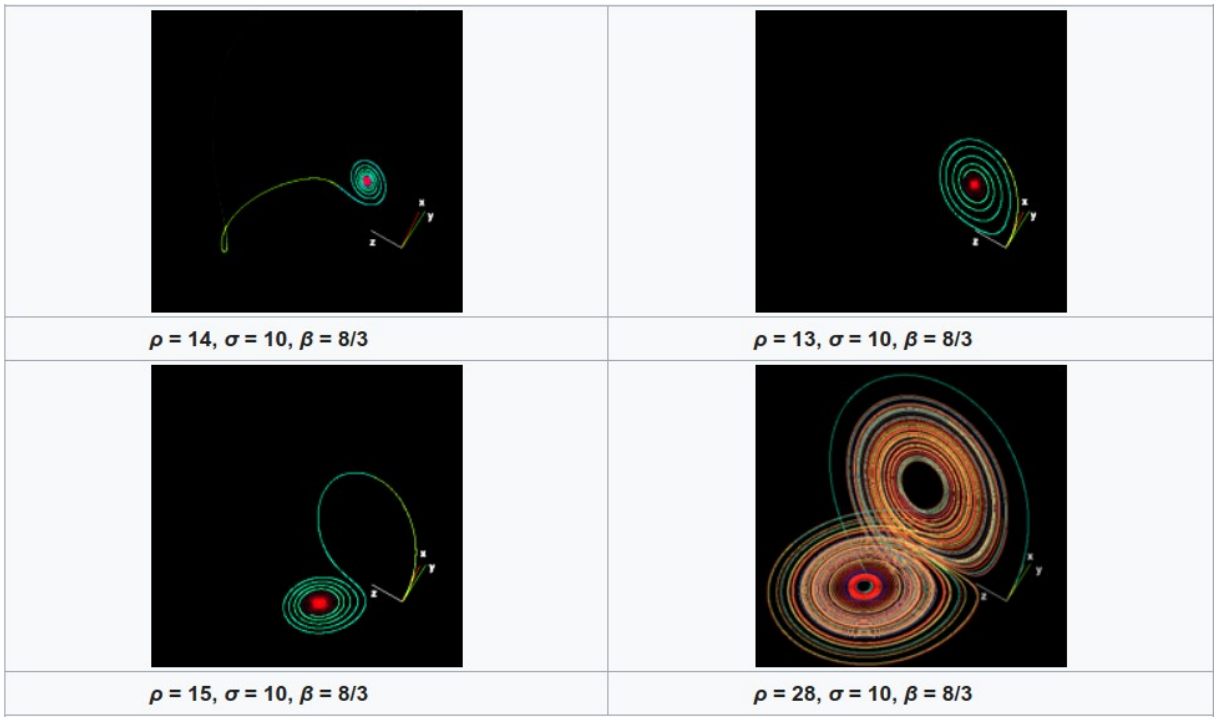

Figure i3.1. Trajectories (solutions) of the Lorenz model for different values of ρ. *Altering only one parameter out of three changes drastically the dynamics of the system, from stable (top left), to unstable with chaotic behaviour (bottom right). (Adapted from Wikipedia, retrieved 2020-01-20)*

The consequence is that when the equations of motion are conservations laws, the dynamics are invariant, *i.e.* they do not change in time.

However, proving the existence of conservations laws in complex systems such as the atmospheric circulation is a challenge. The system's configuration and phase spaces are complex, and many fundamental properties such as the number of stationary points, the stability of the system away from those points, the probability of visiting a region of the system's phase space, can be dramatically altered by a slight change in the equations of motion' parameters or initial conditions (Figure i3.1, 2).

The Lorenz model is a simple example of the complexity of the atmospheric circulation. It represents the motion of an unique air particle in the context of ocean-atmosphere interactions as a function of convection, temperature difference between up and downward currents and non-linearity of the vertical temperature gradient (Lorenz 1963). The model is a system of three differential equations with x, y, z as the unknowns and three parameters ρ, β, σ fixing the couplings between the unknown variables. Altering the coupling parameters will change the dynamics, transitioning from stable, to unstable (Figure i3.1).

Similarly, changing the initial conditions can lead to dramatic divergence in two different trajectories (Figure i3.2). Applying such model to N particles with $N \gg 1$ is intractable unless some heavy constraint is imposed of the equation of motions.

In this study, we apply a global constraint of the dynamics, that of extremal length invariance (Lars V. ahlfors 1973). This conformal invariant is a measure of shortest distance between two boundaries of a $d-$dimensional smooth manifold that is constant under conformal transformations. Conformal transformations have been shown, in some specified setting, to preserve dynamics. Thus, systems showing a constant (through time) extremal length, have constant dynamics, and thus, are characterized by conservation laws.

So far, we are not aware of any study exploiting the extremal length constraint on dynamics, even less on atmospheric circulation's.

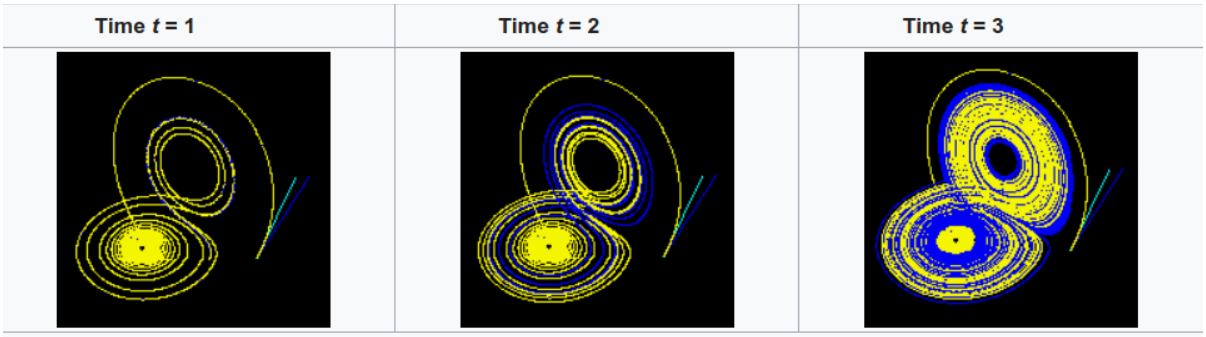

Figure i3.2. Sensitivity to initial conditions. *Two trajectories with the same parameters (blue and yellow), start with points only* 10^{-5} *apart in the phase space. Initially (t=1), the two trajectories are superimposed, but they soon start to diverge considerably after some time (t=2). (Adapted from Wikipedia, retrieved 2020-01-20)*

In this Part III, we first undertake some theoretical work, presented in supplementary work, to characterize this extremal length constraint on dynamics, then, we will apply our theoretical results to the North Atlantic atmospheric circulation variability, to unravel its possible symmetry breaking, that is, when conservation laws do not hold anymore, and dynamics change.

NB: *This study relies on a theoretical section (see supplementary material S1-S3), which demonstrates the different dynamical consequences of the constraints imposed by the extremal length. This reasoning represents a base of discussion and should not be considered as an attempted demonstration. Reading this theoretical section is not needed to understand the following chapter, however, we strongly encourage the readers to delve into the theoretical reasoning behind the advocated properties of the conformal structure presented below.*

Introduction

A striking characteristic about mid-latitudes atmospheric circulation is that fundamental characteristics of its dynamics, such as the number of equilibria, the stationary and transition states, and the stability/instability of those states, are still debated (Ghil 2019). Several approaches have been tried to model the mid-latitudes atmospheric circulation: linear, nonlinear, deterministic, stochastic, or combined models, however, so far, any of those models only partially matches with observations (Ghil et al. 2018). In any of those approaches however, the combined role of Rossby waves and westerly Jet streams is omnipresent (Shutts 1983; Michael Ghil and Childress 1987; Nakamura et al. 1997; Ghil and Lucarini 2019). An interesting feature of non-linear dynamics is the bifurcation in the state-space of a system, *i.e.* when a small variation in the control parameters leads to abrupt, often reverse, effects in the response of the system; when such a bifurcation exists, the system hosts several equilibria (c.f. Fig 1 in Ghil et al. 2019). Bifurcation in mid-latitude atmospheric circulation, giving rise to the so-called zonal and blocking equilibria, has long been studied (Lorenz 1963; Charney and DeVore 1979; Benzi et al. 1986; Mo and Ghil 1987), and been observed as solutions for simple, barotropic models on rotating annuli (Legras and Ghil 1985; Weeks et al. 1997). The statistical studies also provided evidence for those two stationary states (Cassou et al. 2004; Hauser et al. 2015; Table 1 in Ghil et al. 2018). The transitions between those regimes being of prime importance, it is natural that numerous studies are devoted to the topic (Robertson

and Vitart 2019, and refrences therein). While most studies focus on intra-seasonal time scales, there is an increasing focus on bimodality (and hence, transitions between regimes) at time scales greater than the synoptic scale (Hannachi et al. 2017). The literature on the topic is therefore rich; however, there still is a possibility for fresh approaches. For instance, dynamical models bring the possibility of quantifying the dynamics, but the very nature of those is still dependent on the underlying assumptions of the models (*e.g.* deterministic, stochastic, linear, non-linear, faithful representation of topography, topology of the subspace for computations and so on.). Statistical analyses are less dependent on assumptions, but provide little dynamical picture.

In this study, we offer a different approach based on the correspondence between dynamics, differential geometry, and complex analysis. We use the Lagrangian formalism in the phase space to demonstrate that the non-vanishing time derivative of a conformal invariant, the extremal length (Lars V. ahlfors 1973), represents a change in dynamics in the phase space of atmospheric circulation, trading momentum for thermal energy. We also show that the extremal length conditions the possible shapes of the atmospheric circulation patterns. Our methodology is significantly different from those highlighted above. The usual dynamical model framework is to try and find stationary solutions (in our context, stationary patterns) within certain dynamics. In our study, we do not make assumptions on the dynamics, but a range of them and how they transition to each other. In a way, our approach is study the non-stationarity of the North Atlantic atmospheric circulation dynamics. We think the topic of geometrical physics, as seen through the extremal length paradigm, is of significant interest in the study of atmospheric circulation dynamics because of its weak assumptions, and connection with fundamental characteristics such as space-time and energy density. The present work focuses on inter-annual (2 to 8 years' time scales) Euro-North Atlantic atmospheric circulation variability.

This study relies on a theoretical reflection on the dynamical properties of extremal length, as well as a conjecture by Kenneth Stephenson on random geometric triangulations, which led to the development of a new method to compute the extremal length of a hypersurface. Theoretical works and supporting experiments are available in supplementary material S1-3.

In Section 1, we introduce the data and methodology, as well as the notion of extremal length, and we summarize the theoretical results obtained in supplementary material S1-3. Different North Atlantic atmospheric patterns are extracted using fuzzy clustering, and their statistical transitions are presented, in Section 2. In Section 3, we first compare how the time-evolution of those atmospheric patterns links to temporal changes in extremal length. In Section 4, we further examine the extremal length dynamics using phase-space reconstruction and probability density functions, and how they link to the weather patterns. We explore links between the phase space of North Atlantic circulation's extremal length and precipitation over France in Section 6. Finally, we discuss our main result and their wider implications in Section 7.

1. Data and methodology

1.1. Climate Data

The North Atlantic atmospheric circulation is here inferred using annual geopotential height at 500hPa (z500), which were derived from NOAA's 20CR v2c reanalysis ensemble (Compo et al. 2011). Under the geostrophic approximation, winds are parallel to the iso-geopotential height lines, and this is particularly relevant at 500hPa (Norbury and Roulstone 2002). Data are subset to the 1968-2008 period for consistency with the hydrological data set, and to the Euro-North Atlantic regions (100°W-40°E and 5°S-80°N; Figure 3.1c). The 20CR v2c reanalysis ensemble contains 56 members, which allow for quantifying the model induced dispersion. Prior to this study, we ran a dispersion analysis showing that from 1950's, taking

the average member is robust, as the member dispersion greatly decreases from this decade (not shown), indicating that the results should not be driven by the model over this period.

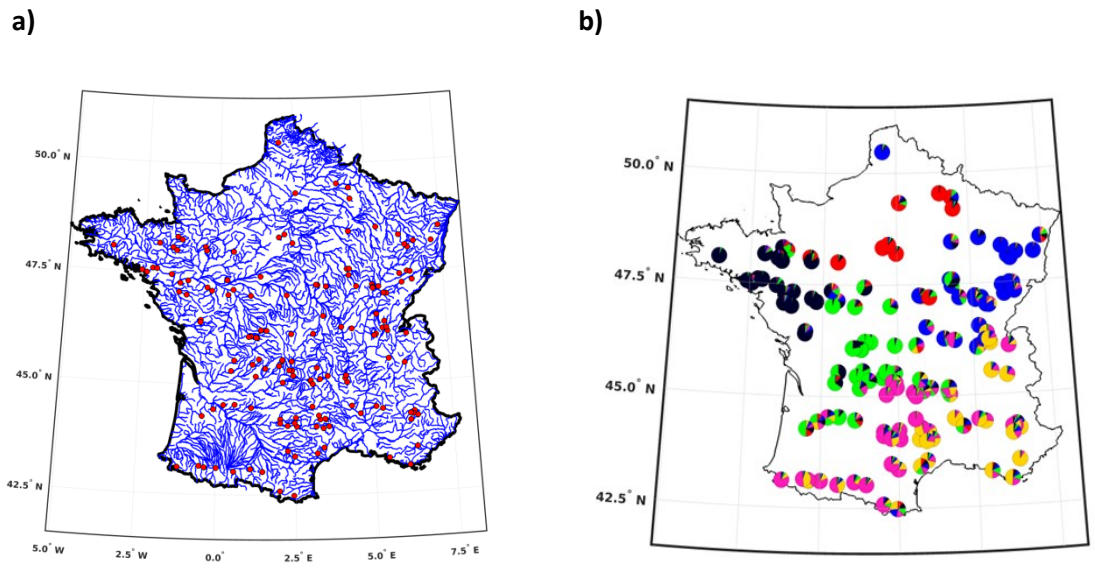

Figure 3.1. Research area and regions of homogenous discharge variability. *a) Location of stream gauges (red dots) and their respective networks (blue lines) stations location; b) Regions of homogeneous discharge variability as defined in Part I, Figure 1.9.*

1.2. Hydrological Data

In Part I, we identified six regions of homogeneous scale-time discharge variability. For this study, we compared the extremal length phase space with periods of wet and dry precipitation averaged over the North-eastern cluster (blue region, Figure 3.1b).

Precipitation data was extracted from the SAFRAN reanalysis data set ("Systeme d'Analyses Fournissant des Renseignements Adaptes a la Nivologie"; Vidal et al. 2010). This data set is formatted as a regular grid of 8 kilometers spaced nodes that covers metropolitan France. Data start in August 1958, and is updated as new data are available. For this study, we averaged the monthly data to annual, subset to the 1968-2008 period, and spatially average within each watershed of the six homogeneous regions (cf. Part I).

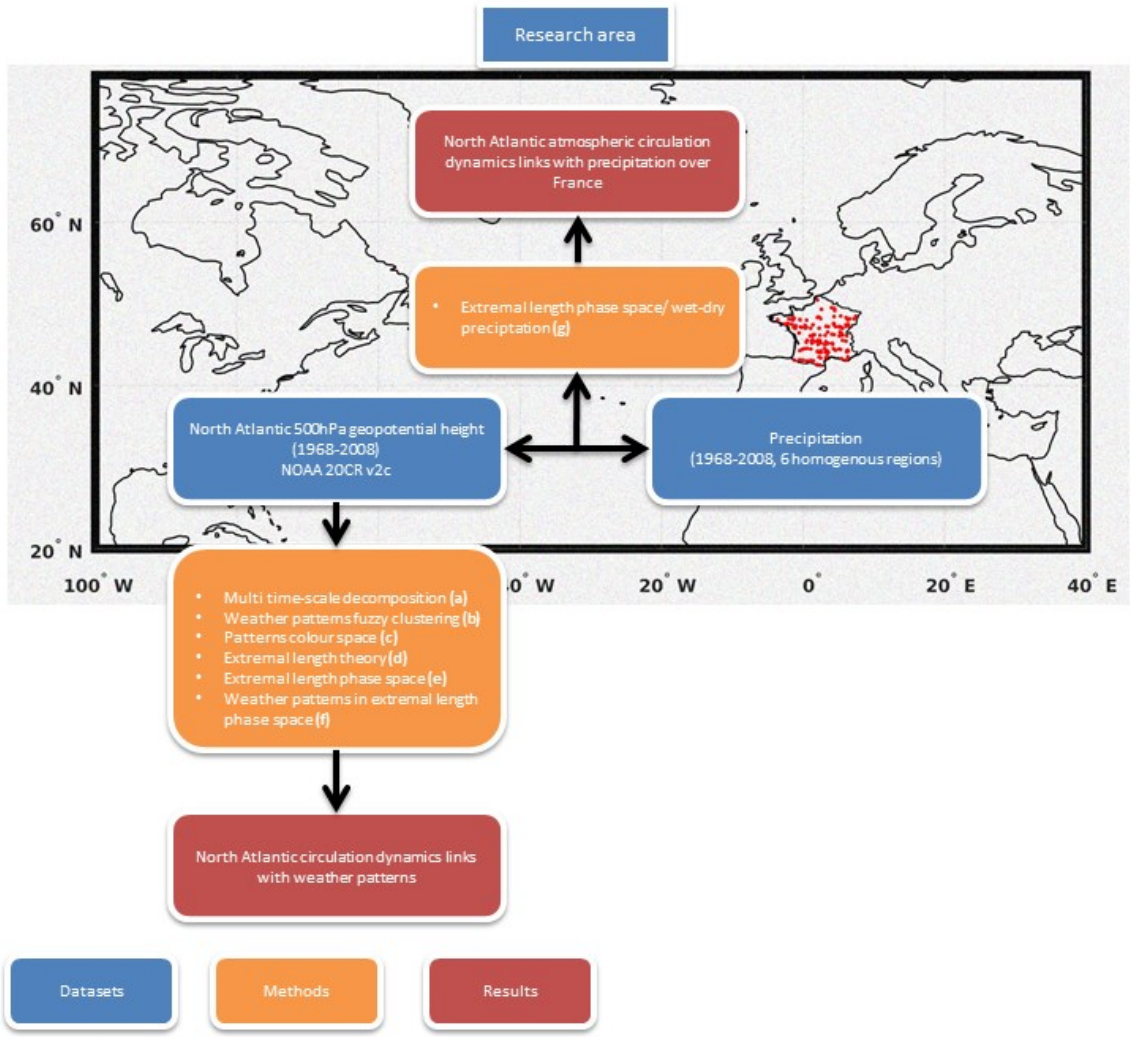

Figure 3.2. Workflow of this study. *a.)Precipitation and z500 data are reconstructed at 2-4, 5-8 years, and climatological time scales (i.e. anomalies); b.)Weather patterns are computed through fuzzy clustering; c.) Transitions between patterns are studied; d.) Dynamical properties of extremal length are researched; e) The changes in z500 conservation laws are explored through extremal length's phase space; f) The statistically extracted weather patterns are compared to each dynamical state in extremal length's phase space; g)Wet and dry precipitation periods are associated with extremal length phase space's states.*

1.3. Methodology

As preliminary step, we reconstruct both precipitation and large-scale climate data at 2-4, 5-8 years, and climatological time scales, using multiresolution analysis (Figure 3.2, (a)). The methodology is split into two approaches, which are compared. The first one is the statistical approach the dynamics of the climate data. We use Fuzzy clustering (See 1.3.1) to infer stationary regimes Figure 3.2, (b)), and then their transitions by projecting each type of pattern on an RGB colour space (Figure 3.2, (c)). This approach is based on the occurrences, and transitions, of patterns identified by their shape. The second approach is based on using the dynamical properties of extremal length, explored in supplementary material S1-3 (Figure 3.2, (d)), to investigate the change of dynamics in the large scale climate data (Figure 3.2, (e)). Within this approach, the changes in dynamics are tied to changes in extremal length with time, and not tied to precise shapes but to a conformal equivalence class of shapes. Thus, exploring the extremal length phase-space gives important information about the stability and stationarity of the climate data's dynamics. We bridge both approaches by comparing the phase-space of extremal length and the weather patterns extracted by the statistical techniques (Figure 3.2 (f)). Finally, we compare the phase-space of extremal length with dry and wet periods of precipitation over North-eastern France (Figure 3.1, blue), to investigate possible links between the climate data dynamics (*i.e.* stationarity, stability) and precipitation over (Figure 3.2, (g)).

1.3.1. Extracting North Atlantic circulation patterns using statistical techniques

Fuzzy clustering (Dunn 1973) is used to cluster the different North Atlantic circulation patterns based on their similarities, the representative patterns of each cluster are called weather patterns (Figure 3.2, (b)). The procedure is broken into two steps. First we compute the distance between each pattern using Image Euclidean distance calculation (IEDC), which

emphasizes more on global than local similarities (Wang et al. 2005). Then, we cluster atmospheric patterns that are similar, using FANNY clustering, which allows for a flexible clustering of hybrid patterns, *i.e.* patterns sharing multiple features with others (Kaufman & Rousseeuw, 1990). For more information about this procedure, see Chapter 1.

We visually classify weather patterns as either of zonal, blocking or wave train type, with colors red, green and blue respectively. We then compute the transitions between clusters by projecting each time step on a chromaticity diagram (Figure 3.2, (c)). Each time step coordinates (*i.e.* color) is computed as:

$$rgb_{t_j} = \sum_{c_1}^{c_N} p_{c_i}(t_j) * rgb_{c_i} \quad (1)$$

Where rgb_{t_j} is the color at time stept_j, $c_{i..N}$ is the cluster i identified by the fuzzy clustering, $p_{c_i}(t_j)$ is the probability of membership to cluster c_i of the time step t_j, and rgb_{c_i} is the color of the cluster c_i, with the color being either red, green or blue, depending on the type of the weather pattern (*i.e.* zonal, blocking or wave train).

The color of each time step's pattern is then projected into the RGB gamut, the coordinates (RGB) determining where the pattern lies compared the three types of weather patterns.

1.3.2. Extracting the dynamics of the North Atlantic atmospheric circulation

1.3.2.1 Representation of a system's dynamics

The phase-space of a dynamical system is the space of all its possible parametrized configurations (Figure 3.2, (e)). A path, or trajectory, in the phase-space represents the successive configurations taken by the system along time. Phase-space analysis is critical in non-linear system dynamics, as it enables the description of attractors and bifurcations (see for instance, Michael Ghil and Childress (1987)). However, phase-space representation needs

an underlying model so that the space is spanned by the parameters of the model. When the data is a time series, *i.e.* when the model is unknown, owing to Taken's theorem (*in* Rand and Young 1980), the dynamics of a system can be topologically reconstructed by embedding the time series in a space, of embedding dimension D_{emb} , whose basis vectors are the time series' value at a time t and time $t - n\tau$ (where τ is a time lag). The dimension D_{emb} is chosen using a false nearest neighbour algorithm (Kennel et al. 1992), and the lag is 2^{j-1}, with j being the discrete wavelet dyadic time scale at which the time series is reconstructed. Instead of plotting the trajectory of the extremal length, we estimate the kernel density of the trajectory, (*i.e.* the probability of the system to visit some regions of the phase-space), which allows for more easily identifying stationary points and bifurcations. The kernel density is estimated using diffusion (Botev et al. 2010). It can be argued that the number of data points in our study (41) is too low for a correct estimation of the kernel density of the system. However, we note that our phase-space is that of extremal length, which is, in itself, a marker of dynamics change. Thus, even if the kernel density estimation is too biased by our sample, we argue it still is a valid representation of the dynamics. Our results are presented with a 4-view phase space reconstruction of extremal length (cf. Figure 3.6a). The diagonals represent coordinates where the τ order derivatives of the extremal length vanish, *i.e.* where the dynamics are constant. The probability density function (PDF) estimation for each visited region of the phase space is shown by the iso-surfaces, and high PDF represent basins of attraction. Because the centres of those basins represent constant dynamics, we consider them as critical points of our phase space. In order to compare with the statistical clustering, the statistically extracted patterns are plotted against the extremal length phase space. We associate to each pattern, a unit-vector showing the direction it is headed into at the next time step; the vectors are coloured from blue to red as a function of time (*i.e.* vectors in blue are associated to early patterns, vectors in red, to later patterns). If, as time goes to infinity, the

vectors point toward the critical point, then the system is said to asymptotically stable, otherwise it is unstable. A special case is that of periodic trajectories, which are considered stable, but not asymptotically. We also use the information provided by recurrence plots (Eckmann et al. 1987). The plot takes the form of a an almost symmetric matrix with indices times i, j. The distance between the position of the trajectory at time i and at time j is computed. If the distance is small, then the trajectory at time j is located close to the position it was at time i, and reversely. The general shape of a recurrence plot thus allows for an estimation of the divergence of the trajectory, that is, if it tends to move away from its initial values or, to the contrary, always stays within a certain region of the phase-space. The topology of recurrence plots can be complex, however, as a rule of thumb, ridges (high distance coordinates) materialize non-stationarity or abrupt local changes, and troughs are associated with cyclicity (Yang 2011).

In table 1, we provide a general rule of thumb for the interpretation of recurrence plots depending on the texture, the general shape, of the plot.

1.3.2.2 The notion of Extremal length and its approximation

This study relies on the theoretical works presented in supplementary material S1-3 (Figure 3.2, (d)). For more detail, see supplementary material.

The notion of extremal length follows the pioneering works by Ahlfors (1973). Extremal length is the minimum length of a family of curves that go from one point to another. This definition seems similar to that of a geodesic. However, extremal length is conformal invariant, which means that under global conformal transformations, extremal length is constant. This generalizes the idea of geodesic to conformal transformations.

Observation	Interpretation
Homogeneity (uniformly distributed red and blue points)	the process is stationary
More ridges to the upper left and lower right corners	nonstationarity; the process contains a trend or drift
Disruptions (ridges bands) occur	nonstationarity; some states are rare or far from the normal; transitions may have occurred
Periodic/ quasi-periodic patterns	cyclicities in the process; the time distance between periodic patterns (e.g. lines) corresponds to the period; long diagonal lines with different distances to each other reveal a quasi-periodic process
Single isolated points	heavy fluctuation in the process; if only single isolated points occur, the process may be an uncorrelated random or even anti-correlated process
Diagonal lines (parallel to the line of interest)	the evolution of states is similar at different times; the process could be deterministic; if these diagonal lines occur beside single isolated points, the process could be chaotic (if these diagonal lines are periodic, unstable periodic orbits can be retrieved)
Diagonal lines (orthogonal to the line of interest)	the evolution of states is similar at different times but with reverse time; sometimes this is a sign for an insufficient embedding
Vertical and horizontal lines/clusters	some states do not change or change slowly for some time; indication for laminar states
Long bowed line structures	the evolution of states is similar at different epochs but with different velocity; the dynamics of the system could be changing (but note: this is not fully valid for short bowed line structures)

Table 1. Recurrence plot interpretation overview. *(http://www.recurrence-plot.tk/glance.php)*

In two-dimensions, there are possibly infinitely many local conformal transformations between surfaces, however, only finitely many surfaces may be globally transformed, and

those must have the same extremal length. In addition, this extremal length corresponds to specific geometrical characteristics, which all surfaces in the equivalency class (*i.e.* with the same extremal length) share. Those characteristics determine how those surfaces can transform into another of the equivalency class. Using the geometry-physics equivalence (Noether 1971), we conjecture that two surfaces, of constant extremal length share the same dynamics,, and that any change in extremal length is attributed to loss of conservation for either thermal energy of momentum.

In addition to the changes in dynamics associated with extremal length, we summarize the results of theoretical study, in terms of North Atlantic atmospheric circulation characteristics associated with and increase or decrease in extremal length:

- For both the geostrophic tendency and geostrophic wind equations' solutions to be stationary, the first order derivative of extremal length should vanish (S1, Proposition 1).
- With respect to the map boundary's corners, which are fixed points, the deformation of the interior, that is, of geopotential height iso-lines, is proportional to extremal length. Decreasing extremal length will tend to zonal patterns, increasing extremal lengths to Rossby waves with high wave numbers (Proposition 2).
- Increasing extremal length is associated with momentum loss to the profit of thermal energy. This induces slow or stalled Rossby waves, blocking patterns for geopotential height tendency solutions, and low momentum, high curl geostrophic wind equation solutions. (Propositions 3-6)
- The computation of extremal length is explained in detail in S1 (Section 6). Briefly, the computation relies on the conjecture that if a surface is triangulated randomly, and that N random triangulations are performed, the conformal structure of the surface will emerge as $N \to \infty$. The extremal length is then computed by projecting this conformal

structure to a rectangle, the conformal rectangle. The extremal length a conformal rectangle is simply its width divided by its height (Stephenson 2007).

1.3.3. Testing time-scale dependency

To test the time-scale dependency of the North Atlantic atmospheric dynamics and its links to hydrological variability, multiresolution analysis has been used to reconstruct climate and hydrological variability at two selected time scales (Figure 3.2, (a)): 2-4 and 5-8 years' time scale. Multiresolution analysis is the combination of a discrete wavelet transform analysis (*i.e.* decomposition of the signal into discrete wavelet coefficients) and a synthesis (*i.e.* reconstruction of the signal at each time scale; Percival and Walden 2000). The signal is decomposed by a series of orthogonal filter banks in dyadic time scales that represent the wavelets (Percival and Walden 2000).

Here, we use the Maximum Overlap Discrete Wavelet Transform (MODWT), with a base wavelet 'sym4' (Percival and Walden 2000). The main difference compared to other methods, such as the Discrete Wavelet Transform, is that the signal is not downsampled as the scales increase, so the initial time step of the signal is used for all scales. Naturally, the translation independence is lost, but shift invariance is preserved. More information about the wavelet decompositions and reconstructions are available in Chapters 1 and 2.

3. Statistically-extracted North Atlantic circulation patterns

North Atlantic circulation weather patterns have been statistically extracted using fuzzy clustering, at two different timescales, and using the raw z500 climatological anomalies. For ease of description, we categorized the weather patterns as either zonal, blocking or wave train, as described in, Mo and Ghil (1988); Cassou et al. (2004); Hauser et al. (2015); Park et al. (2014). Note that, because of the subjectivity in classifying each weather pattern into a

category, our definition of zonal, blocking and wave train patterns may slightly differ from previous authors. The criteria for each type are as follows:

- Zonal weather pattern: Two centres, one ridge and one trough, are parallel to each other and the iso-height lines are aligned along the west-east direction. There are very little North-South geostrophic winds. Westerlies arising from the Positive phase of the North Atlantic Oscillation are an example of zonal flows.
- Blocking: A centre of action, usually a ridge, forces the geostrophic wind to locally adopt a North-South direction, thus blocking the West-east direction of the flow. Two types of blocking are recognized, the Rex block, when one ridge is to the north of one trough, and the Omega block, when a ridge to the north stands in between two troughs to the south, upstream and downstream of the ridge, respectively. Blocking systems are associated with persistent weather, as the eastward progression of the centres is greatly slowed down. The Atlantic ridge and the Scandinavian blocking are two examples of blocking weather patterns.
- Wave train: A highly meridional flow, with a fast succession of trough and ridges, triggered by Rossby waves. Storm tracks are typically the result of wave trains.

The blocking weather pattern is the most difficult to characterize because, when using anomalies as data, one can find patterns that have the spatial characteristics of a blocking pattern, but with opposite phases (*i.e.* the low pressure centre is to the north, the high pressure to the south). We rather classify a blocking pattern depending on the deformation of the iso-lines, and by elimination with wave trains, that is, if the geopotential height lines are highly deformed at one location but that the pattern is not coherent with a wave train one, then, it is a blocking pattern.

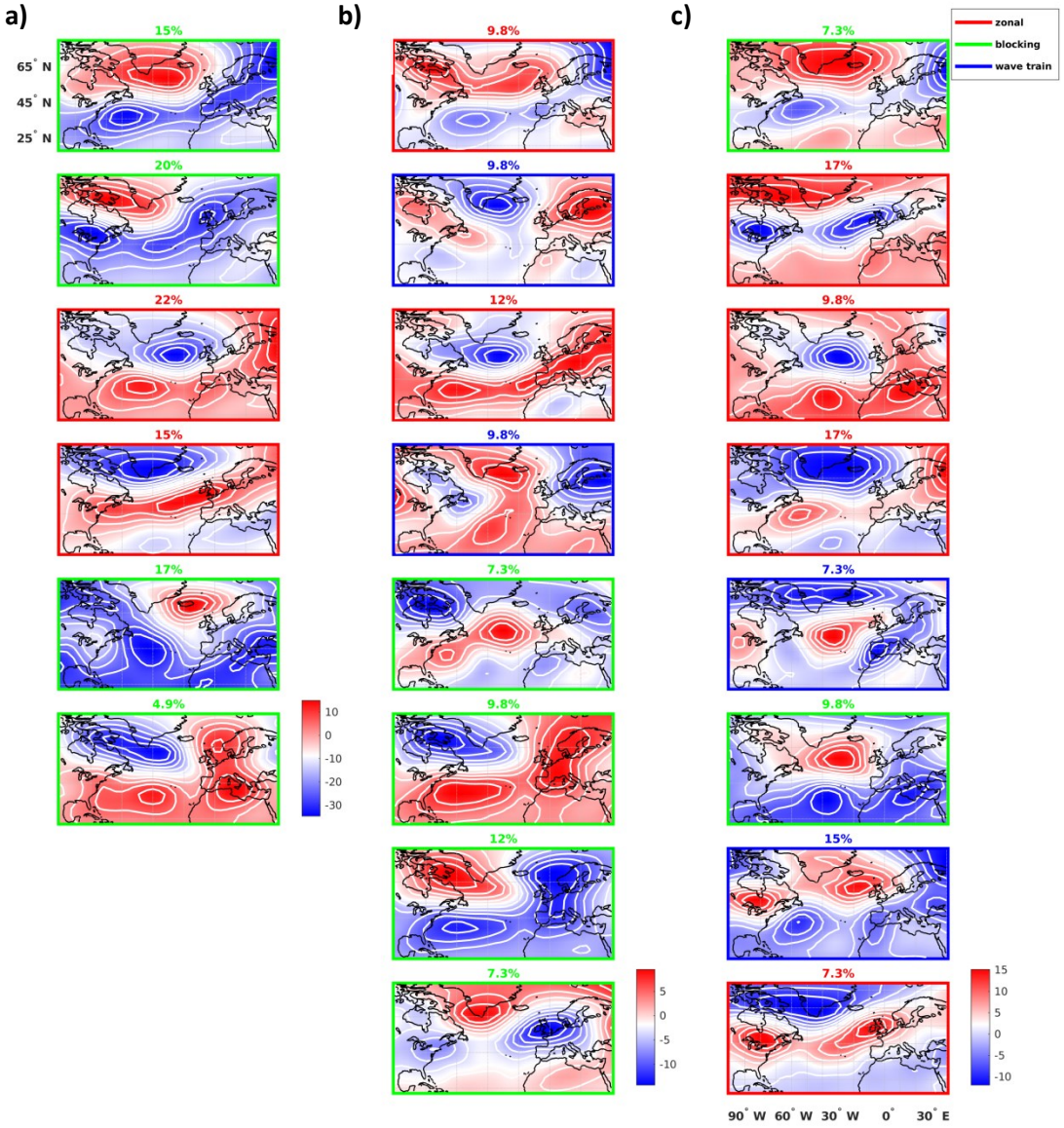

Figure 3.3. Statistically extracted weather patterns of z500. *a) Climatological time scales; b) 2-4yr' time scales; c) 5-8yr' time scales. Boxes' edges colours represent the type of weather pattern.*

3.1. Climatological patterns of z500

Figure 3.3a shows the weather patterns at the climatological time scales computed by fuzzy clustering. Six weather patterns are identified. Weather patterns 3 and 4 are of the zonal type;

patterns 1, 2, 5 and 6 are of the blocking type. There is no wave train pattern identified (Figure 3.3a). Pattern 2 (blocking) is the most recurrent pattern with probability 20%, while pattern 8 (blocking) is the least recurrent, with probability 8%. Blocking patterns are dominant with 57% of occurrence, followed by zonal patterns with 43%, leaving only 7% of the patterns not clearly identified with one weather pattern. Figure 3.4a shows that transitions between zonal and blocking patterns occur in both ways, but no hybrid pattern persists, *i.e.* zonal patterns quickly transition to blocking and reversely (Figure 3.4a).

3.2. 2-4 years' time scales

Figure 3.3b displays the 2-4yr' time scales pattern extracted from the fuzzy clustering. Eight weather patterns can be identified. Patterns 1 and 3 are of the zonal type, patterns 5-8 are of the blocking type, and patterns 2, and 4 are of the wave train type (Figure 3.3b). Patterns 4 (zonal) and 7 (blocking) are the most recurrent (12%), while patterns 5 and 8, only occur with probability 7%. Blocking patterns are dominant (37%), followed by zonal (23%), then wave train weather patterns (20%), leaving 20% of the patterns not clearly identified with one weather pattern.

3.2. 5-8 years' time scales

Figure 3.3c displays the 5-8yr' time scales pattern extracted from the fuzzy clustering. Eight weather patterns are identified. Patterns 2, 3, 4 and 8 are of the zonal type, patterns 1 and 6 are of the blocking type, and patterns 5 and 7 are of the wave train type (Figure 3.3c). The highest occurring weather pattern is pattern 2 (zonal, 17%), and the lowest are patterns 1, 5 and 8 (blocking, wave train, and zonal respectively, 7%). Zonal weather patterns are dominant (51%), followed by wave trains (22%), with blocking patterns occurring with probability 17%, leaving 10% of patterns not clearly associated to a single weather pattern (Figure 3.3c). Figure 3.4c shows that zonal patterns transition into wave trains, and blocking patterns also transition to such type, but blocking and zonal transitions are two-way (Figure 3.3c).

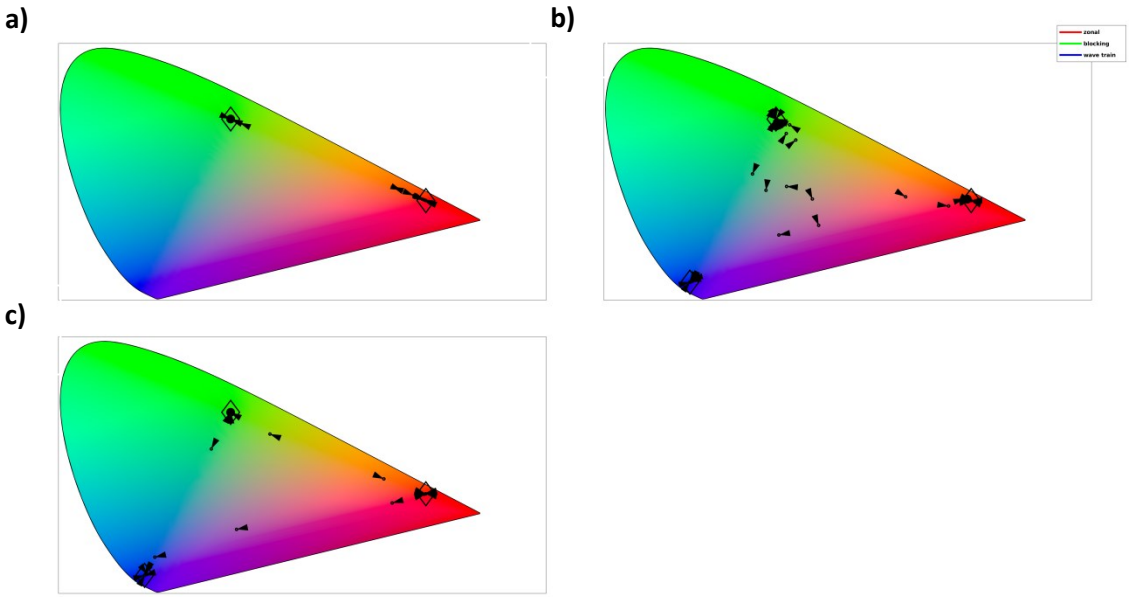

Figure 3.4. Transitions between weather patterns. *Each time step's pattern is attributed a coordinate in RGB colour space, based on its weighed membership to zonal (red), blocking (green), and wave train(blue) weather patterns. This allows discovering the transitions between patterns. a) Climatological time scales; b) 2-4yr' time scales; c) 5-8yr' time scales.*

Figure 3.4b shows that such mixed patterns are frequent, and that transitions occur between two weather patterns, but also between weather patterns and mixed patterns. Preferred directions of transition are from blocking to zonal, blocking to wave train and zonal-blocking-wave train hybrid patterns to any of the weather patterns (Figure 3.4b).

3.3 short summary

We have computed the fuzzy clustering of weather patterns for the North Atlantic atmospheric circulation, at climatological, 2-4yr and 5-8yr' time scales. For climatological time scales, only zonal and blocking weather patterns appear, however, at 2-4 and 5-8yr' time scales, wave train patterns are added to the classification. The number of different weather patterns is time scale dependent, as at climatological time scales, six weather patterns are

extracted, while eight patterns are found for both 2-4yr and 5-8yr' time scales (Figure 3.3). At climatological, and 2-4yr' time scales, blocking patterns are dominant, while it is the zonal type of weather patterns that dominates the 5-8yr' time scales (Figure 3.3). Transitions are also time scale dependent. At climatological time scales, the transitions between zonal and blocking patterns is two way, while, at other time scales, the transitions show preferred directions. For instance, at 2-4yr' time scales, blocking patterns mainly evolve into either zonal or wave train patterns, while at 5-8yr' time scales, zonal to wave train, and blocking to wave train are the preferred directions (Figure 3.4). At 2-4yr' time scales, several patterns are of a hybrid type, and transition to/from them occur (Figure 3.4b). This section has shown that, the type of weather patterns, their stationarity, and transitions are time scale dependent. It has also shown that the type of weather pattern, rather than the patterns themselves, is more important in terms of dynamics of the North Atlantic atmospheric circulation. In the next section, we will extend this class of patterns reasoning, to a more general setting.

4. The dynamics of the North Atlantic atmospheric circulation

In the previous section, we identified, statistically, weather patterns and their transitions at both climatological, 2-4yr and 5-8yr' time scales. The paradigm behind that identification is that a weather pattern represents a certain point in the phase space of the North Atlantic atmospheric circulation's dynamics, and that, locally, this point can only be visited by trajectories initiated by the same initial conditions or, with the same set of parameters. This is also equivalent to saying that the number of degrees of freedom of the z500 is sufficiently high so that only a specific set of control parameters can lead to that pattern. While we do not have a definite answer to that question, we decided to tackle the problem differently by stating that only the local geometry, a proxy of the stress energy tensor, spread homogeneously over the total z500 surface, can be a unique identifier of similar dynamics, *i.e.* only if two surfaces

have the same local geometry, extended to their total area, then they are the result of the same dynamics.

The object used to assess that local geometry, extended to the whole surface, is the extremal length (Lars V. ahlfors 1973). We computed the extremal length of each z500 surface of the time series, then reconstructed the phase space of extremal length to assert the stable and transitional states of the z500, this time, under an energy point of view, thus, not tied a type of weather pattern.

We compare this approach to that of statistical extraction by analysing to which dynamical state, weather patterns map to.

4.1. Climatological dynamics

Figure 3.5a shows the time series of climatological extremal length, with each weather pattern superimposed. The time series has one maximum in 1978, of blocking type, and one minimum in 1988, of zonal type (Figure 3.5a). The 1988 dip roughly divide the time series in two parts: the first one has more abrupt changes than the second. The weather patterns are not tied to extremal length, which can be explained by the difficulty of the statistical clustering to clearly identify patterns with weather patterns. That difficulty arises because patterns rarely show a complete similarity to the weather pattern(s) they are assigned to. In Figure 3.6a, climatological extremal length's phase space shows a large basin of attraction, crossed by all zero derivative lines in the 4-view of Figure 3.6a, which induces that, the dynamics at those time scales, for the most part, are constant (Figure 3.6a). Because the extremal length's derivative represents a set of solutions, for the atmospheric circulation phase space, that are constant (*i.e.* $\frac{d}{dt}x = 0$), we can consider the basin of attraction lying on the zero derivative line as critical point of the extremal length's phase space. We can see, in any of the four

views, that the vector field around that point, mostly converges to it, as red vectors point toward the critical point, suggesting that the climatological are mostly stable (Figure 3.6a).

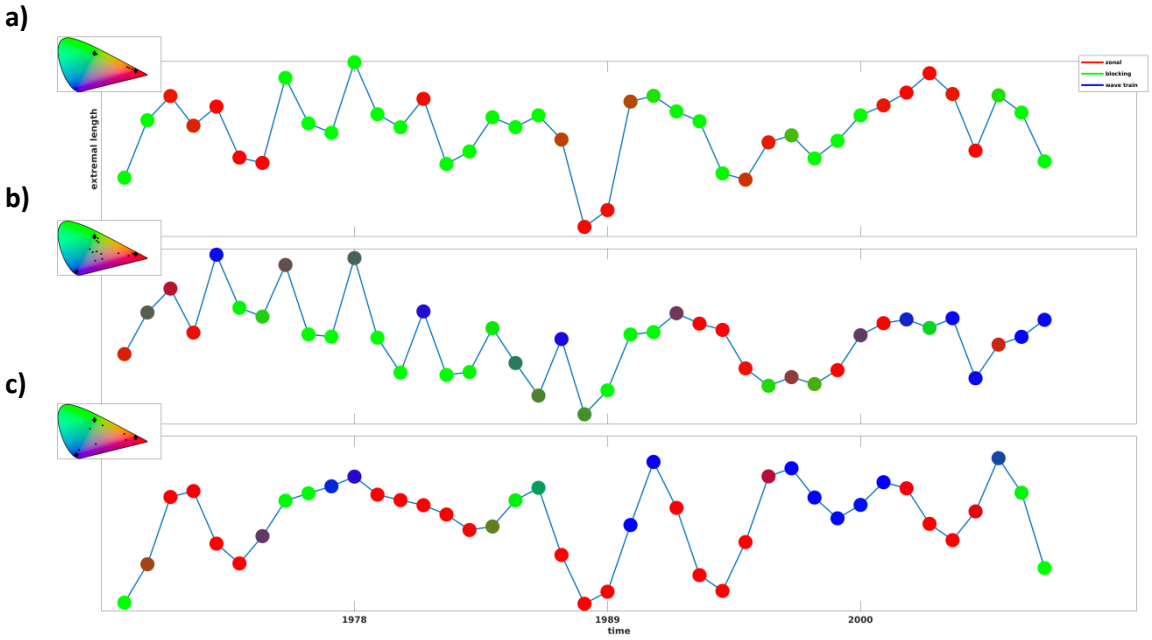

Figure 3.5: Extremal length (lines) and weather patterns (colours). *(a) Climatological time scales; (b) 2-4yr' time scales; (c) 5-8yr' time scales.*

Three other small basins of attraction exist, two of them concerned with blocking patterns, the other being composed of two zonal patterns (Figure 3.6a). With respect to the main basin of attraction, those small basins are all of lower extremal length, suggesting an influx of momentum when those states arose (Figure 3.6a). For all of them, the vectors point toward the main basin of attraction, which may indicate, that, while they represent changes of atmospheric circulation dynamics (as they are outside of the zero-derivative lines) some control parameter brings them back to the main basin of attraction (Figure 3.6a). Figure 3.6a shows that around the stable basin of the phase space, different weather patterns are identified with one location and one type of weather pattern can be at several locations. According to our extremal length hypotheses (cf. 1.3.2.2), a weather pattern is not necessarily representative of one dynamics *i.e.* different controls parameters can lead to the same weather pattern, and the same dynamics can lead to different weather patterns.

In Figure 3.7a, we explore the recurrence of trajectories in the phase space of extremal length. The succession of troughs and ridges in Figure 3.7a, both horizontally and vertically, in the recurrence plot indicates that the trajectory is trapped in different states, but highly non stationary until data point 21 (1988), before the trajectory starts to converge towards a point, being stationary (homogeneous recurrence, Figure 3.7a).

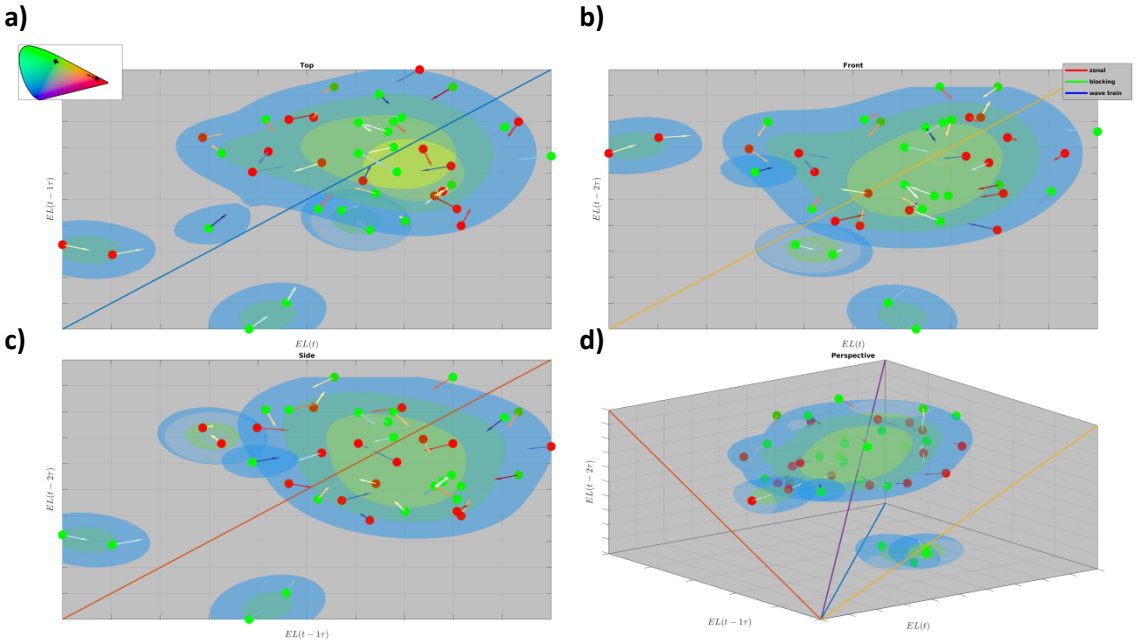

Figure 3.6a. 4-view phase space of climatological time scales' extremal length, and its relation to weather patterns. *(a) Top, (b) Front, (c) Side, (d) Isometric; Probability of an area of the phase space to be visited is represented by isosurfaces (from blue to yellow). Arrows point to the next time step, their colours represent their position in the time series (blue for early time steps towards red for late time steps), colors represent the weather pattern type, each time step belongs to.*

4.2. 2-4 years' time scales' dynamics

Figure 3.5b shows the time series of 2-4yr' time scales' extremal length, with each weather pattern superimposed. The time series has one maximum in 1972 (of wave train type), and one minimum in 1988, of a mixed blocking-zonal type (Figure 3.5b). We note that, as for climatological time scales, both 1975 and 1978 years are also among the highest extremal

length values, and 1988 is also a common minimum (Figure 3.5b). The 1988 dip roughly divide the time series in two parts: the first one has more variance than the second.

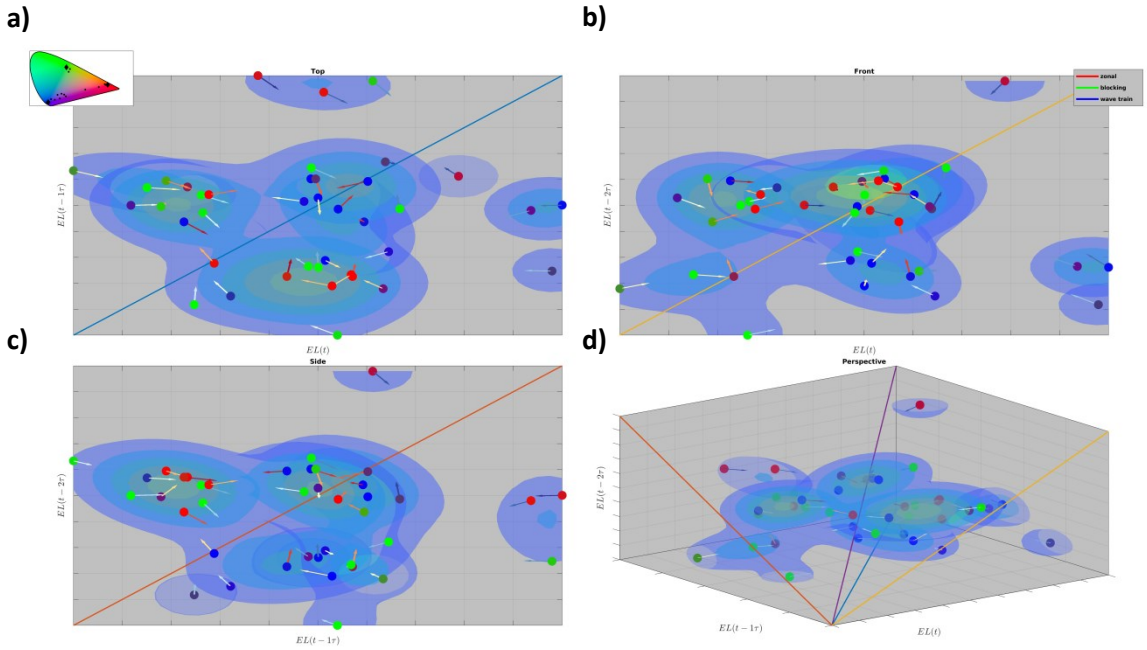

Figure 3.6b. 4-view phase space of 2-4yr' time scales' extremal length, and its relation to weather patterns.

Compared to climatological time scales, because of the higher degree of weather pattern blending, the correspondence between weather types and extremal length is harder to establish. Figure 3.6b shows the 4-view phase space reconstruction of 2-4 time scales of extremal length. Three main basins of attraction have been computed, each of them being on the zero derivative line of either top, front or side planes, and the two others, are symmetric about each plane zero-derivative line (Figure 3.6b). While both zonal and blocking patterns reside in the two of the basins, the third one is mainly populated by wave train patterns, those being the most constant at first order, *i.e.* they reside on the top plane's zero derivative line (Figure 3.6b). This basin, is associated with higher extremal length than the two others, suggesting that the 1τ-stable state of the atmospheric circulation is associated with heat release (Figure 3.6a). The vector field seems to point at constant exchanges between the three nodes, which indicate that each basin is unstable, even if, globally, the trajectories seem

periodic, which means they are stable (but no asymptotically stable, Figure 3.6b). Outlier basins can be found on the boundaries of the phase space domain, being either attracted to another outlier or one of the main basins of attraction (Figure 3.6b). The 2-4yr' time scales recurrence plot in Figure 3.7b, shows that the system is highly disrupted, thus non stationary, until data point 22 (1989), after which, it converges, as for the climatological scales.

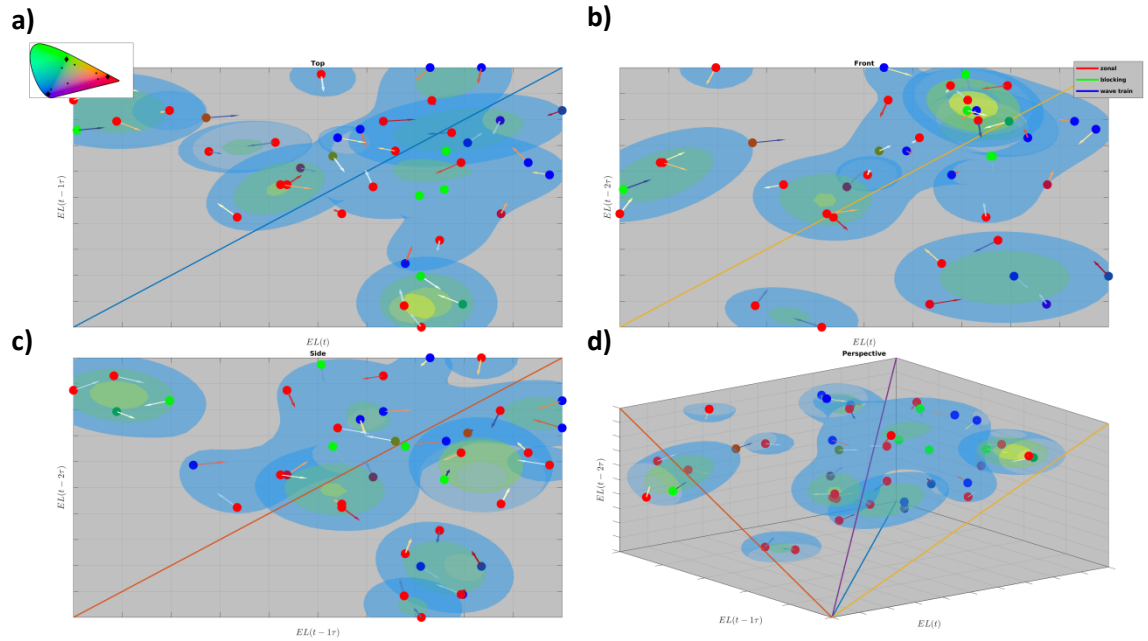

Figure 3.6c. 4-view phase space of 5-8yr' time scales' extremal length, and its relation to weather patterns.

4.3. 5-8 years' time scales' dynamics

Figure 3.5c shows the time series of 5-8yr' time scales' extremal length, with each weather pattern superimposed. The time series has two maxima in 1991 (of wave train type), and 2006 (mixed wave train-blocking type), and a minimum in 1988, of zonal type (Figure 3.5c). The 1988 dip roughly divides the time series in two parts: in contrary to both climatological and 2-4yr' time scales, the first part is the one with the lowest variability, while the second is especially variable (Figure 3.5c). Figure 3.6c shows the 4-view phase space reconstruction of 5-8yr' time scales of extremal length. A large cluster of basins of attraction appears along each plane zero-derivatives lines, however, the basin with the highest pdf is constant only in

second-order dynamics (front plane, Figure 3.6c). Wave train patterns are mostly confined around first (top), second (front) order, and lagged (side) constant dynamics, while zonal patterns show more variability (Figure 3.6b). Overall, the extremal length associated with most basins is fairly high, hinting at a system dominated by (relatively) higher heat release (Figure 3.6). The vector field displays trajectories that can wander far from constant states, and red arrows do not necessarily point towards the zero-derivative lines, indicating that the system is globally unstable (Figure 3.6c).Compared to previous time scales, the 5-8yr' time scales recurrence plot in Figure 3.7b, shows an even more disrupted phase-space, with very little convergence, that happens at data point 29(1996), 8 years after data point 22 (1989).

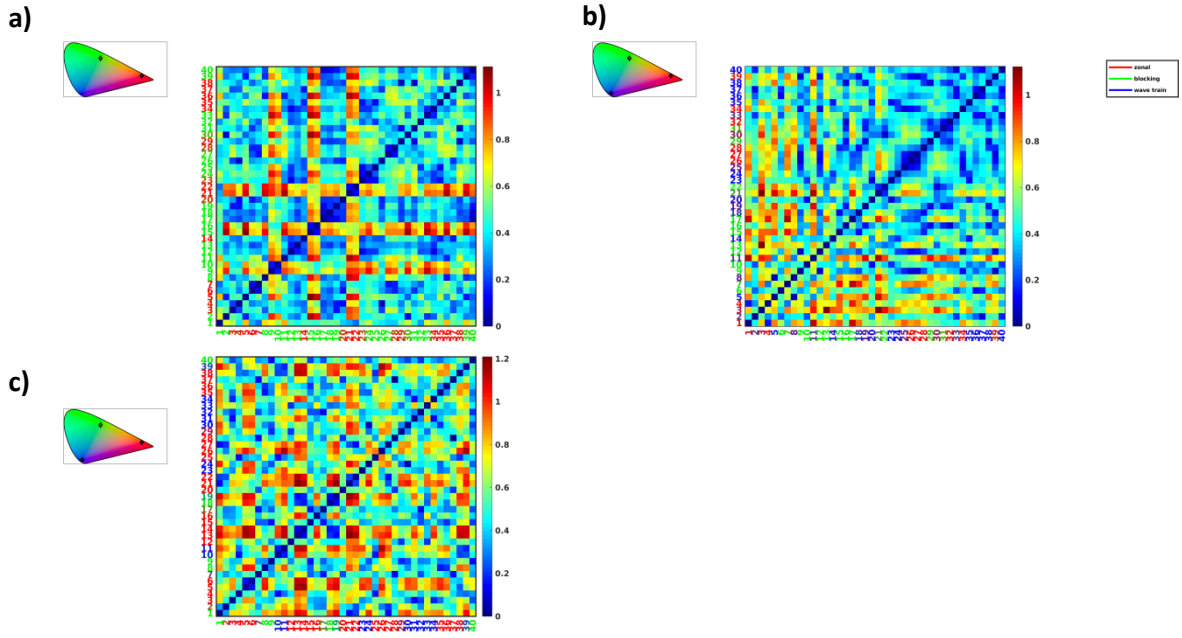

Figure 3.7. Recurrence plot of extremal length. *Weather Patterns are noted by the colours of the time indices (a) Climatological; (b) 2-4 years; (c) 5-8 years.*

4.4. Short summary

We reconstructed the phase space of extremal length at climatological, 2-4, and 5-8yr' time scales, and superimposed the statically extracted weather patterns. We have shown that at climatological time scales, the dynamics are mostly stable and globally constant (especially after 1989) and stable (Figure 3.6a), yet locally non-stationary (Figure 3.7a). No weather

pattern is tied to the constant basin of attraction, but outliers basins are tied to either zonal or blocking patterns (Figure 3.6a). At 2-4yr' time scales, the dynamics are shown to be split between three basins of attraction, one being of either first, second or lagged constant dynamics and the others being symmetrical to the zero-derivative lines (Figure 3.6b). Wave train patterns seem to be tied a particular type of dynamics, and to first-order, the most constant types (Figure 3.6b). Constant exchanges take place between the three basins, but overall, the system seems to be periodic, thus stable, but not asymptotically (Figure 3.6). As for the climatological time scales, the 2-4yr' time scales dynamics are highly disrupted until 1989, after which, they being to converge, which indicates that the dynamics become stationary (Figure 3.7c). At 5-8yr time scales, the dynamics are distributed over several basins, that are not necessarily close to the zero-derivative lines, *i.e.* not constant, however wave train patterns are the most constant, while zonal patterns show the highest deviation from the stationary state. In addition, the vector field points outward of each basin, indicating that the system is possibly unstable (Figure 3.6c). The recurrence plot shows that the system is disturbed throughout the time series, and only after 1996, does the intermittency decreases, but still stays very significant, compared to other time scales (Figure 3.7c). The 5-8 years' time scales dynamics seem to be mostly associated to heat release of the research area, yielding and atmospheric circulation with lesser momentum (Figure 3.6).

4. Links between the dynamics of North Atlantic atmospheric circulation and precipitation over France

In this section, we investigate the relationships between extremal length's phase space and precipitation over France, as characterized in Part I. For the sake of simplicity we only showcase the relationship between extremal length and the North-Eastern region, defined as the blue stations in Figure 3.1b. We compared the climatological, at 2-4yr and 5-8yr' time scales, the extremal length's phase spaces with dry and wet precipitation periods of

precipitation. The wet and dry data points are selected in the precipitation time series as points $mean(X) \pm 0.8sd(X)$, that is points below (wet) or above (dry) 80% of the standard deviation to the mean.

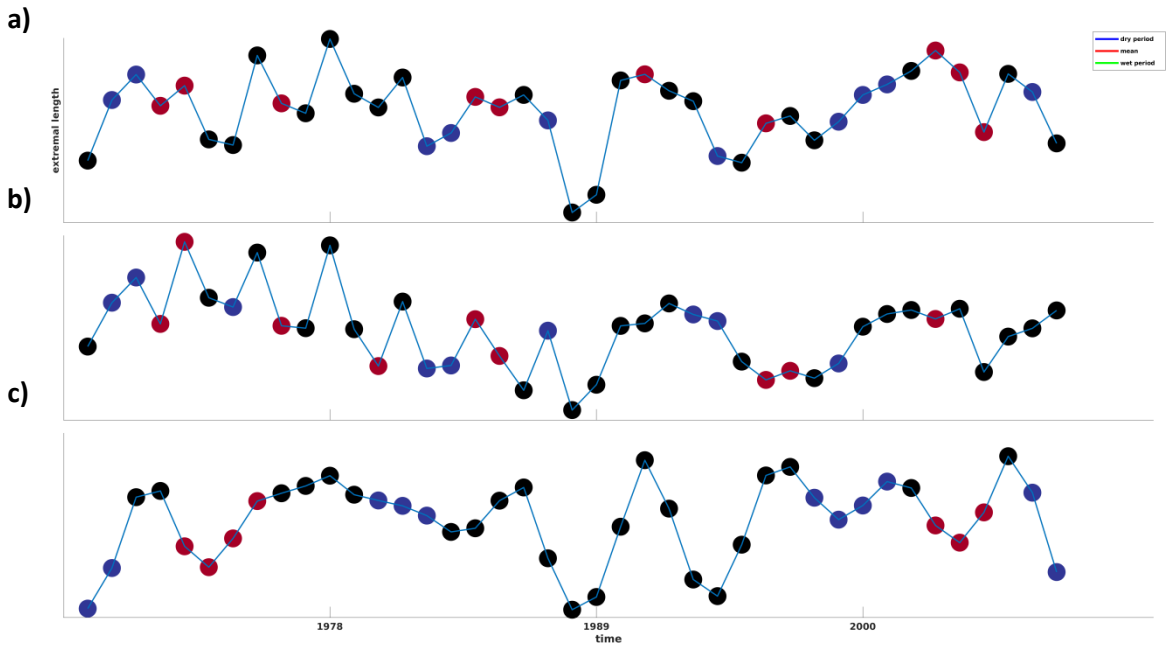

Figure 3.8. Extremal length (lines) and dry (red), mean(black), wet(blue) precipitation years. *(a) Climatological; (b) 2-4 years; (c) 5-8 years.*

5.1. Climatological extremal length and precipitation

Figure 3.8a displays the climatological extremal length time series, with dry and wet periods superimposed. Neither dry nor wet periods are associated with a specific value of extremal length, and the maxima and minimum of extremal length are associated to mean precipitation values. Figure 3.9a shows the 4-view of climatological extremal length's phase space and the superimposed wet and dry periods. While first-order (top) plane does not show any discriminating characteristic for dry and wet periods, both second-order (front) and lagged (side) planes display dry and wet periods as being separated by the zero-derivative lines (Figure 3.9). Taking both second order and lagged plane, we have a second-order difference equation solution space, and we can deduce that dry period are associated with positive

(forward) curvature of the extremal length variability, while wet periods are associated with decreased (forward) curvature of the extremal length variability (Figure 3.9).

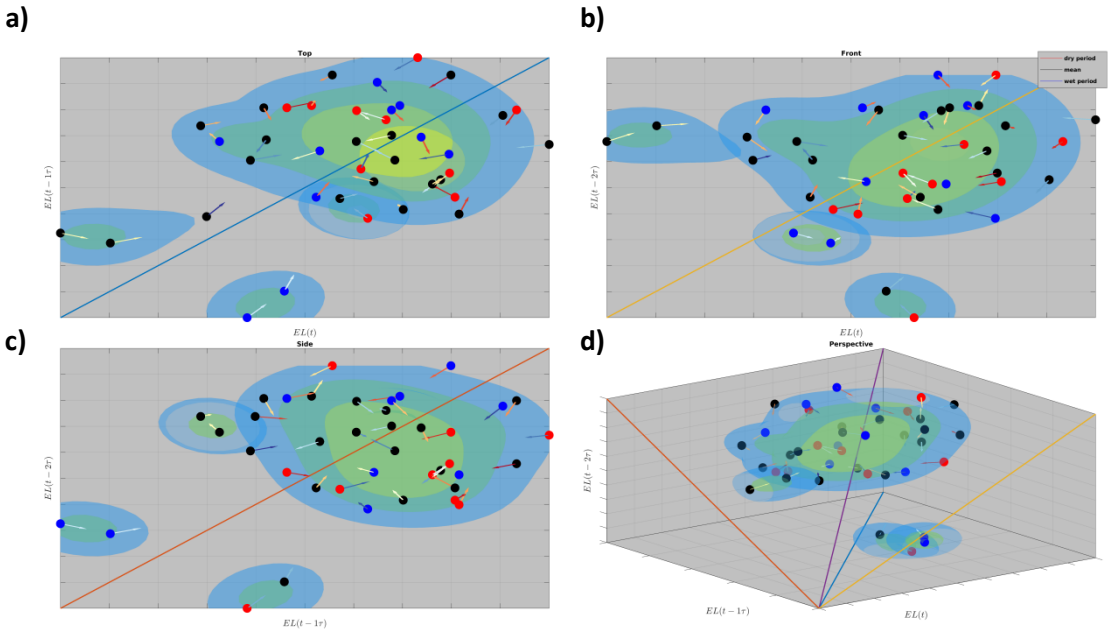

Figure 3.9a. 4-view phase space of the climatological time scales' extremal length in relation to precipitation in the North-eastern region. *(a) Top, (b) Front, (c) Side, (d) isometric; Probability of an area of the phase space to be visited is represented by the iso-surfaces (from blue to red). Numbers represent the time steps, colours represent wet (blue) and dry (red) precipitation years.*

5.2. 2-4 years extremal length and precipitation

As for climatological time scales, there is no clear association between extremal length values and either dry or wet periods (Figure 3.8b). Figure 3.9b shows the 4-view of 2-4yr' time scales extremal length's phase space and the superimposed wet and dry periods. Each of the three basin of attraction is associated with both wet and dry periods, however, in the second-order (front) plane, dry precipitation is absent from the basin of attraction concerned with increases in extremal length, at the 2τ scale, from a medium value (Figure 3.9b). It thus can

be concluded that each of the basin of attraction, that is, each set of dynamics, can produce wet or dry precipitation periods.

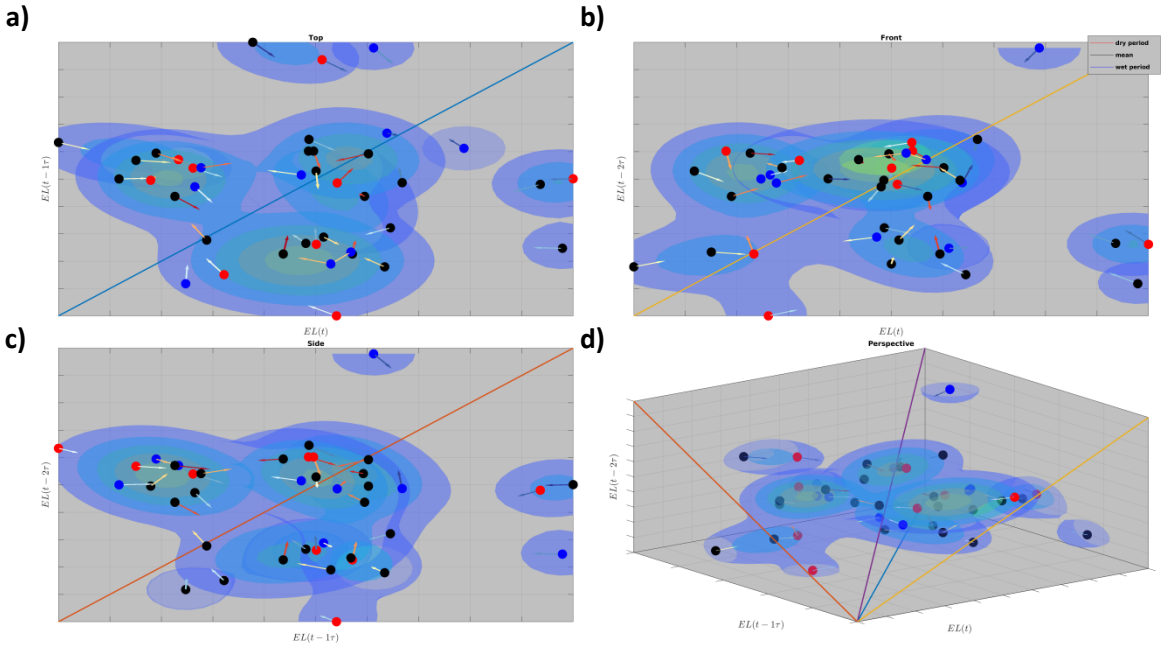

Figure 3.9b. Phase space of extremal length. Same as Figure 3.9a, but for 2-4yr' time scales.

5.3. 5-8 years extremal length and precipitation

Figure 3.8c shows that, dry precipitation periods are associated with a positive curvature of the extremal length, however, that pattern is not exclusive to dry periods as both mean and wet periods may be identified with that characteristic. In the extremal length's phase space, the distribution of both dry and wet periods is variable, however, each basin of attraction seems to contain mainly either dry or wet data points (Figure 3.9c). In the first-order plane, dry periods are closer to the zero derivative line than wet periods, which suggest that dry periods are associated with more constant dynamics, and wet periods to large changes (Figure 3.9c).

5.4. Short summary

We compared the climatological, 2-4, and 5-8yr time scales' extremal length's phase space, and dry and wet periods of precipitation for the North-eastern region (cf. Figure 3.1b, blue stations). At climatological time scales, dry periods are associated with positive (forward) curvature of extremal length variability, while wet periods are associated with a decrease in the (forward) curvature of extremal length variability (Figure 3.9a). At the 2-4yr' time scales, no definite relation could be established between extremal length and precipitation, except that each basin of attraction can be produce both dry and wet periods (Figure 3.9b). At the 5-8yr' time scales, each basin of attraction is associated with either dry or wet periods, and dry periods are more associated with basins that are close to the first-order zero-derivative line (Figure 3.9c).

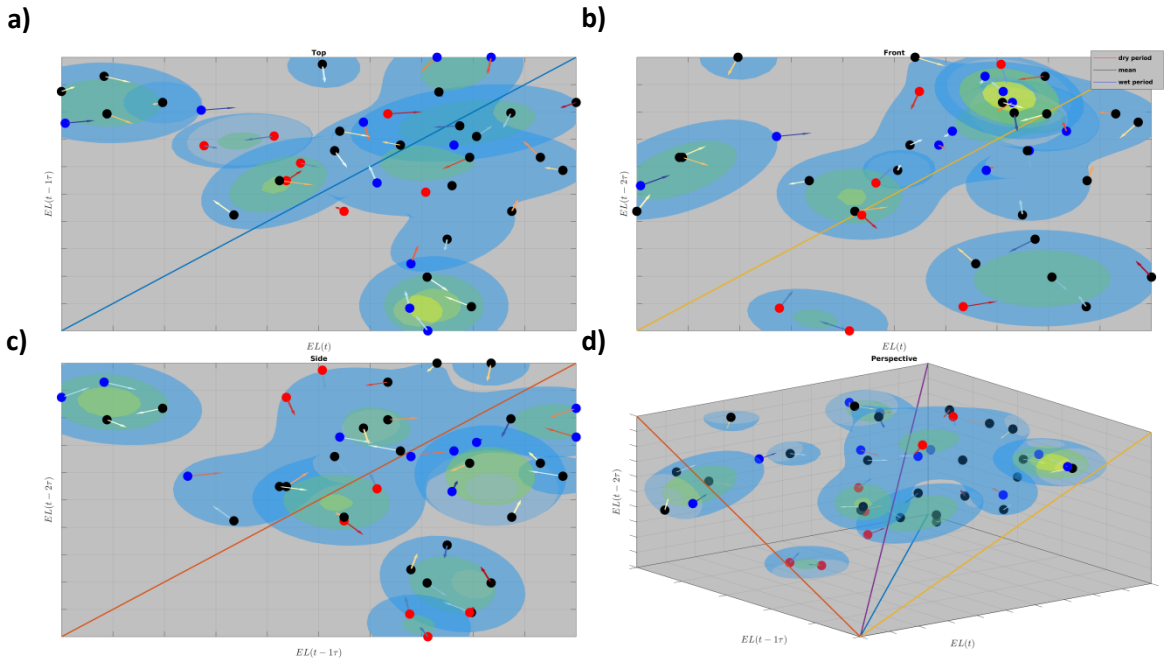

Figure 3.9c. Phase space of extremal length. Same as Figure 3.9a, but for 5-8yr' time scales.

5. Discussion

In this study, we investigated the dynamics of the North Atlantic atmospheric circulation, at different time scales, using both statistical and geometry-physics equivalence methodologies. Conformal geometry theory was explored to derive the dynamical properties of a conformal invariant, the extremal length (Lars V. ahlfors 1973), and the phase space of this invariant was studied to understand the stationarity, stability and equilibrium states of the North Atlantic atmospheric circulation, and how they related to statistically extracted weather patterns and their transitions. Additionally, we compared the extremal length phase space with dry and wet periods over a region of homogeneous precipitation variability, in France.

The theoretical investigation led to interesting results. First, relating extremal length to dynamics evolution, we found that a vanishing time derivative of extremal length implies conserved dynamics. Next, characterizing the solution space for dynamics, it appears an increase in extremal length is associated with a higher deformation of the physical domain with respect to its fixed boundary points, integral lines points towards the transversal boundaries, lower elastic energy, and the interior momentum being lost to thermal energy. Conversely, a decrease in the extremal length is associated with less deformation of the interior, integral lines going through the two boundaries considered for the definition of the extremal length, higher elastic energy, and an increase in the momentum to the expense of heat release. Thus, the extremal length represents the difference between the resting and unloaded length of a rubber band, translating into the resistance to displacement of elementary points, *i.e.* shear (as in an electrical network). In the context of point mechanics, we also found that an increasing extremal length meant an increase in the momentum needed to move the point a certain distance in a given time, or, equivalently, the total energy spent moving a point over that distance. Applied to the context of North Atlantic circulation, an increase in extremal length induces higher meridional flow, low zonal advection (possibly stalled) wave trains, with persistent ridges and troughs.

In the applied section, we found that for both statistical and extremal length methodologies, the atmospheric circulation dynamics are time scale dependent. At climatological time scales, only blocking and zonal patterns were statistically extracted, blocking weather patterns being the most recurrent, with two-way transitions between the two types of weather patterns. The climatological dynamics are mostly stable and constant, but no specific weather pattern is associated with constant dynamics. However, deviations from the stable state leads to basins of attractions associated with either zonal or blocking patterns. The wet and dry periods of climatological precipitation have been found to be tied to a decrease/increase in forward curvature of the extremal length variability. At the 2-4 years' time scales, blocking, wave train and zonal weather patterns were extracted, and blocking patterns were found to be the most recurrent type of weather patterns. The transitions between them show preferred directions, such as blocking patterns evolving into either zonal or wave train patterns, and hybrid patterns of those three types. The wave train weather patterns seem to be tied a particular type of dynamics, and to first-order, the most constant types. The stability of the system seems to be periodic, hence stable, but not asymptotically. Both dry and wet periods can be produced by either basin of attraction at those time scales, so no definite association between the type of period and a given basin of attraction have been found. At 5-8 years' time scales, zonal weather patterns are dominant, and zonal to wave train, blocking to wave train are the preferred directions of transitions. At 5-8yr time scales, the system is non-stationary, and unstable, however, wave train patterns were found to be the most stationary, with zonal being associated with large changes of dynamics. Wet and dry periods are associated with each basin of attraction of the extremal length' phase space, but no spatial segmentation appears.

Our statistical results are in good agreement with the generally accepted most recurrent weather patterns, that is, zonal, wave train and blocking such as Mo and Ghil (1988); Cassou et al. (2004); Hauser et al. (2015); Park et al. (2014). The computed transitions between are

however different than those highlighted in Ghil (1987). The authors focused on the atomic time scales of transition, that is, the minimum time scales for transitioning between patterns. On the one hand, our study, being yearly, may depict discrete transitions rather than continuous. Focusing on inter-annual time scales, Hauser et al. (2015), computed a fuzzy clustering over the same region as ours, and computed the dominant winter (djf) weather patterns (clusters). The fuzzy clustering of the authors has extracted two blocking and two zonal, but no wave train patterns. The authors considered inter-annual time scales as a whole, while we separated climatological, 2-4 and 5-8 years, additionally, we argue that, at least one blocking pattern, G+ (Figure 11 in Hauser et al. (2015)), may be interpreted as a wave train. The time series of dominant winter weather patterns (Figure 19 in Hauser et al. (2015)) is only partially in agreement with ours. The numerous differences in both methodologies, such as no inter-annual dependence, only winter months being selected, or the number of clusters, make pinpointing the reasons for this discrepancy difficult.

The study of the North Atlantic atmospheric circulation through the extremal length has produced very interesting results. We outlined that, for every time scale, stationary or non-stationary, stable or unstable dynamics, can yield either blocking, zonal or wave train weather patterns. Thus, our study has shown that a weather pattern can be the solution of different dynamics, and its stability, stationarity are not exclusive to some dynamics (some initial conditions). The dynamics of North Atlantic circulation are usually stable, except for the 5-8 years' time scales. We however must mention that the sample size, at that time scale, is low, since we only have 8 oscillations at a maximum, over the period of 41 years. It is thus debatable if the instability of the dynamics is real or not. Nevertheless, we have shown that when dynamics change, some specific types of weather patterns appear. We also have shown that weather patterns may be linked with up to second-order differences in the extremal length

variability, so that, even if weather patterns are not tied to one specific dynamics, they are influenced by the, up to second order, changes in dynamics.

Finally, our study has shown that dry and wet periods of precipitation in France, may be tied to those changes in dynamics, which is a departure from the traditional paradigm of associating a weather pattern to some precipitation (see Part II, and Fritier et al. 2012; Massei et al. 2017).

More work is needed to fully develop our methodology; yet, we think that with this first try, we already produced results that may be of interest for atmospheric sciences and hydrology as well.

PART IV: GENERAL DISCUSSIONS

The objective of this thesis was to provide a better understanding of non-linear and non-stationary characteristics in hydrological variability over France, and its relation to local and large-scale climate input. In particular, this dissertation aims at further understanding how complex interactions, within the climate system, shape the hydrological variability in France. Statistical, spectral and dynamical, approaches were used conjointly to provide a comprehensive spatiotemporal picture of the hydroclimate variability in the Euro-North Atlantic area. The key results and perspectives for further research are here discussed..

1. Spatiotemporal scales of hydroclimate variability in France

In the present context, water quantity and quality are stressed by climate change and diverse socioeconomical issues (IPCC 2014). In France, the OECD (2013) has noted that warming temperature are higher than the world-average, hence enhancing the stress on hydrological variability through different mechanisms at different scales (Gettelman and Rood 2016). Numerous studies therefore investigated the link between hydrological variability and large-scale climate (Kingston et al. 2006, 2007; Massei et al. 2007, 2017; Hannah et al. 2011; Massei and Fournier 2012; Lavers et al. 2013; Dieppois et al. 2014, 2015, 2016a; Lavers and Villarini 2015; Ionita et al. 2017; Laaha et al. 2017), highlighting the scale dependence of such a relationship in both time and space. However, those studies focused on identifying either spatial or temporal scales, and did not account for possible causal relationship between scales. These issues has been addressed in **Part I "Spatiotemporal scales of hydrological variability in France"** through developing a new clustering strategy accounting for temporal changes in the spectral characteristics (*i.e.* various frequencies, or timescales, defining a signal variability, and their relative magnitude), which was applied to different hydroclimate variable (precipitation, temperature and discharge) over 152 watersheds. For each homogenous regions of temporal variability, we then also examine causal relationship

between the timescales defining the signal using conditional mutual information based algorithm (Paluš 2014; Paluš et al. 2018).

Our results indicate that, in France, hydroclimate variability occurs at selected time scales from seasonal to interannual, consistently with the world's largest rivers (Labat 2006, 2008). We found that those time scales are seasonal, annual, 2-4 and 5-8 years respectively. Compared to previous studies (Champeaux and Tamburini 1996; Sauquet et al. 2008; Snelder et al. 2009; Joly et al. 2010), we have shown that Northern France, does not exhibit larger critical scales than southern France, *i.e.* northern France is not more homogenous than southern France in its hydroclimate variability. In addition, discharge variability was found much homogeneous over northern France. Importantly, examining cross-scales causal relationships, we also show that while regions share partly similar spectral patterns, causal interactions defining the spectral patterns are markedly different and complex. The phase-phase and phase-amplitude relationships between time scales can be of any direction (*i.e.* from smaller to larger timescale, and *vice-versa*), either uni-, bi-directional or self-interacting. Such a complexity was already found in El Nino Southern Oscillation (Jajcay et al. 2018), for instance, but has ever been explored on hydrological systems. Interestingly, while phase-phase relationships are transferred from precipitation and temperature to discharge, phase-amplitude relationships are not. We have hypothesized, that, similarly to recent works in neurosciences (Sotero 2016), this absence of phase-amplitude relationship in discharge variability results from heterogeneous filtering of the climatic signal (*i.e.* precipitation and temperature) amplitude by the watershed properties, breaking indirect spatial connections.

We then studied the links between discharge and climate variables at local- (e.g. precipitation and temperature) and large-scale (e.g. North Atlantic atmospheric circulation). There has been a very large amount of studies on the links between both local- and large-scale climate with hydrological variables in the Euro-Atlantic area (Labat 2006; Massei et al. 2007; Slimani et

al. 2009; Gudmundsson et al. 2011b; Boé and Habets 2014; Dieppois et al. 2016a). Recently, however, Massei et al. (2017) highlighted the need for multi-timescale approaches, as North Atlantic atmospheric circulation patterns linked to hydroclimate variability differ from one timescale to another over the Seine watershed (North-Western France). In **Part II "Spatiotemporal scales of large scale hydroclimate variability"**, we built on Massei et al. (2017) by studying the timescale dependence of statistical links between discharge and climate over all the homogeneous regions. Using spectral coherence analysis, we first highlighted that discharge variability is primarily linked to precipitation at inter-annual scales, and to temperature at annual time scales for all regions. Second, looking at the composite patterns of the North Atlantic circulation associated with precipitation and discharge variability, we highlighted differences depending on the timescale and on the region. For instance, south-eastern watersheds are linked to similar atmospheric circulation patterns at both 2-4 and 5-8 years' timescales, while for other regions atmospheric patterns differ largely according to the timescale. Southern watersheds are correlated with weaker meridional pressure gradients, and southward-shifted atmospheric circulation, compared to northern watersheds. At 2-4 years' time scales, northern regions' discharge is linked to a symmetric eastward shift of the Iceland low and Azores high, while, at 5-8 years' time scales, a similar eastward shift is only noted on the Iceland low. Using wavelet similarity and wavelet coherence, we further explored the relationships between discharge and large-scale climate variables. We found that discharge variability in the northern regions show similar spectral pattern than geopotential height at 500 hPa over very specific regions of the North Atlantic, such as the North Sea, but that the common scales of variability extended at much larger spatial scales. Southern watersheds show similar spectral patterns signature over much larger spatial scales, matching much better with the atmospheric circulation patterns identified on the composite analysis. We found that, for any given region, composite, spectral similarity,

and wavelet coherence z500 patterns do not necessarily match, showing the added information associated with each method.

It also highlights clear modulations of the large-scale climate variability by the watershed properties, as atmospheric patterns differ when considering either precipitation or discharge. Such modulations were already suggested by several studies focusing on different part of the world (Gudmundsson 2011; El Janyani et al. 2012; Szolgayova et al. 2014a; Sidibe et al. 2019), however, our study uncovered part of the spatiotemporal dependence of the watershed filter.

2. North Atlantic atmospheric circulation dynamics

Most hydroclimate studies focus on establishing links between the atmospheric circulation and hydrological variables, and assume that this link will be linear and stationary, *i.e.* a given atmospheric pattern will have the same impact on hydrological variability in a given location. For instance, it is generally accepted that the NAO phases are associated with either dry/wet winters over Western Europe. However, this has been put in doubt by studies that do not find any clear and significant relationship between the NAO and hydrological variability (e.g. Shorthouse and Arnell 1997; Massei and Fournier 2012; López et al. 2013; Woollings et al. 2015). In **Part III "Dynamics of the North Atlantic circulation, and hydroclimate variability"** we argued that these conflicting results could be due to relatively different dynamics (i.e. what happened before and after) associated with similar atmospheric circulation patterns (which would be considered as single patterns using most clustering techniques, for instance), leading to different impact on the continent. An important question, in atmospheric circulation dynamics, is to find the equilibrium points of a system's dynamics, as well as the properties of this system (*e.g.* stability or bifurcations) away from those equilibrium points (Hannachi et al. 2017; Ghil 2019). For the past decades, a large body of studies have been devoted to the topic, and early studies demonstrated that atmospheric

circulation have two equilibrium points(Michael Ghil and Childress 1987; Mo and Ghil 1988; Vautard 1990): zonal circulation and blocking circulation. However, the real number of equilibrium states in the North Atlantic atmospheric circulation, their characteristics, and how they transition from on to another still is not fully-understood, especially in the context of climate change (Ghil and Lucarini 2019; Mann 2019).

While many studies focus on the equilibria within prescribed dynamics, in **Part III "Dynamics of the North Atlantic circulation, and hydroclimate variability"**, we adopted a different approach through considering the equilibria and transitions of the system's dynamics themselves. We used the powerful theory of conformal geometry to investigate what conformal invariance in the evolution of atmospheric circulation patterns meant in terms of dynamics. A theoretical reflection yielded the hypothesis that the vanishing moments of a conformal invariant, i.e. the extremal length (Ahlfors 1973), led to conservation of the dynamics of a system. We also qualitatively characterized the dynamical properties of an atmospheric circulation pattern, under a change of extremal length, in terms of elastic energy and harmonic functions. We applied our theoretical results to the North Atlantic atmospheric circulation climatological anomalies, and to anomalies at 2-4 and 5-8 years' time scales, and we compared it to recurrent atmospheric patterns identified via statistical clustering. Three types of patterns, from which we then studied the potential transitions, were found: zonal, blocking and wave train. Our results indicate that using climatological anomalies, only blocking and zonal patterns occur, and transitions a two-way directions. At 2-4 and 5-8 years' timescale, zonal, blocking and wave train patterns were found. In addition, while blocking patterns are transitioning to wave train and especially to zonal patterns at 2-4years' timescale, blocking are primarily transitioning to wave train at 5-8 years's timescale. Similarly, at 5-8 years' timescale, zonal patterns preferentially transition toward wave train patterns. We then computed the extremal length time series for the North Atlantic atmospheric circulation, and

reconstructed the phase-space of extremal length to analyse the changes in the North Atlantic atmospheric circulation, and how they relate to recurrent climate patterns. In the North Atlantic regions, the climatological atmospheric dynamics appears quite stationary, with some intermittency however, and stable. The North Atlantic atmospheric dynamics are characterized by both zonal and blocking patterns forming a stationary basin of attraction, but short-term deviations from these stationary states, describing non-stationary states, are found even during the occurrence of both patterns as well. This suggests that statistical climatological recurrent patterns can result from different dynamics. At 2-4 years' timescales, three dynamical states were found: one being stationary and corresponding to wave train patterns, and two others being symmetrical about the stationary axis describing zonal and blocking patterns. At 2-4 years' timescales, the system of the North Atlantic atmospheric dynamics was found not to be asymptotically stable (*i.e.* not evolving towards stability, but being overall stable). Meanwhile, at 5-8 years' time scales, the same system dynamics are markedly different, and are essentially non-stationary, heavily intermittent and unstable. This might be due to a smaller sample size, affecting the stability of our results.

Finally, we investigated how the extremal length of the North Atlantic atmospheric circulation could relate to dry and wet periods in precipitation over the north-eastern France. The results indicate that, at climatological scales, the shift between dry and wet periods is, at least partly, associated with changes in the forward curvature of extremal length variability, which refers to sudden increases in extremal length. While, at 2-4 years' timescale, no obvious relationships were found, at 5-8 years' timescale, wet and dry periods both appear associated with one of the several basins of attraction of the extremal length phase-space. This suggests that rainfall variability is associated to certain states of the atmospheric circulation.

3. Conclusions and perspectives

Based on our study of hydroclimate variability over France and its link to the Euro-North Atlantic atmospheric variability, at multiple spatiotemporal scales, the following conclusions can be made:

- Both hydrological and climate variability, as well as the links between them, show combined spatial and timescale dependence, in their statistical, spectral and dynamical properties. This is just highlighting a high-degree of non-linearity and non-stationarity in these systems.
- Between 1968 and 2008, the main modes of variability are seasonal, annual, 2-4 years and 5-8 years' time scales. However, longer timescales were identified in Massei et al. (2007) and Dieppois et al. (2016a).
- Discharge in France is mainly driven by temperature at seasonal time scale, and by precipitation at longer time scales.
- Without groundwater support, the watershed properties modulate the inter-annual climate signal in amplitude, only.
- Six regions of homogeneous variability were identified in discharge, each one being characterized by different non-linear local and large-scale climate forcing.
- The North Atlantic atmospheric circulation is characterized by zonal, blocking and wave train patterns, which can however result from different dynamics, impacting precipitation over France.
- Further understanding the atmospheric dynamics is crucial to better understand the historical and future evolution of water resources (hydrological variability).

This study has this demonstrated the importance of accounting for non-linearity and non-stationarity using statistical, spectral or dynamical analysis. The results produced shed some

light on how this non-linearity/stationarity takes its roots in climate and is transferred to discharge. Nevertheless, several areas could be further explored to improve our understanding of the complex relationships between components of the Earth system. A non-exhaustive list of points that appeared as significant limitations during this study is summarized as follows:

- The length of the time series (41 years) was constrained by the need of consistency and good quality data, i.e. without missing values, for both local and large scale hydroclimate variables. For instance, this prevented us to look at decadal time scales. However, long-term hydrological reconstructions introduce their own bias (Caillouet et al. 2016) and hindcast models fail to reproduce several non-linear interactions (Meehl et al. 2014; Bellucci et al. 2015; Bracegirdle et al. 2016). Multi-disciplinary works reconciling climate model evaluation and hydrological reconstruction thus appear crucial to create long-term hydrological data sets and fill this gap.
- The spatial scale selected to study the atmospheric dynamic was sufficient for a climate-impact study, here on France hydrological variability. However, to better understand the climate dynamics at the global scale, this should be extended, as the climate dynamics are heavily constrained by shape, topology and rotation of the Earth.
- We tested several causality analyses (from the same theory as cross-scale interactions) in order to go past commonly used simple correlations, from which physical interpretations have to be done with caution. We think those causal methods demonstrated an important potential, for the characterization of both hydrological and climate analysis.
- The theory of extremal length, and more generally the geometry-physics equivalence, also demonstrated a great potential. Further works, both theoretically and analytically, are however needed to confirm the main results presented here. For instance, integrating constrains imposed by extremal length on the atmospheric dynamics into a

non-linear model could help better characterizing and predicting dynamical changes. Similarly, non-stationary behaviour of both climate and hydrological dynamics could be studied *via* critical phenomena, *i.e.* phase transitions, analysis, in order to understand when and how dynamics shift.

- This dissertation was strictly using observational or reanalysed datasets, using the various new methodologies we developed, future studies should however aim at assessing the performance of global climate models, such as currently provided *via* the Coupled Model Intercomparison Project, which is now entering in Phase 6 (CMIP6; Eyring et al. 2016), or *via* the COordinated Regional Downscaling Experiment (CORDEX; Vautard et al. 2013).

This thesis thus presents robust methodologies allowing studying complex interactions in both space and time at the interface between large-scale climate and hydrological systems. The results provided here are thus addressed to climate and hydrological scientists, which routinely look at complex interactions between different components of the Earth System. Our methodologies could also be systematically applied scientists from diverse background looking at complex interactions between different systems, or different component of a given system.

REFERENCES

Anctil F, Coulibaly P (2004) Wavelet Analysis of the Interannual Variability in Southern Québec Streamflow. J Clim 17:163–173

Anishchenko VS, Vadivasova TE, Strelkova GI (2014) Deterministic Nonlinear Systems. Springer

Anquetin S, Braud I, Vannier O, et al (2010) Sensitivity of the hydrological response to the variability of rainfall fields and soils for the Gard 2002 flash-flood event. J Hydrol 394:134–147. doi: 10.1016/j.jhydrol.2010.07.002

Bellucci A, Haarsma R, Gualdi S, et al (2015) An assessment of a multi-model ensemble of decadal climate predictions. Clim Dyn 44:2787–2806. doi: 10.1007/s00382-014-2164-y

Benestad RE, Førland EJ, Hanssen-Bauer I (2002) Empirically downscaled temperature scenarios for Svalbard. Atmos Sci Lett 3:0–22. doi: 10.1006/asle.2002.0051

Benzi R, Malguzzi P, Speranza A, Sutera A (1986) The statistical properties of general atmospheric circulation: Observational evidence and a minimal theory of bimodality. Q J R Meteorol Soc 112:661–674. doi: 10.1002/qj.49711247306

Bladé I, Liebmann B, Fortuny D, van Oldenborgh GJ (2012) Observed and simulated impacts of the summer NAO in Europe: Implications for projected drying in the Mediterranean region. Clim Dyn 39:709–727. doi: 10.1007/s00382-011-1195-x

Blöschl G, Bierkens MFP, Chambel A, et al (2019) Twenty-three Unsolved Problems in Hydrology (UPH) – a community perspective. Hydrol Sci J 0:1–33. doi: 10.1080/02626667.2019.1620507

Boccard N (2018) Natural disasters over France a 35 years assessment. Weather Clim Extrem 22:59–71. doi: 10.1016/j.wace.2018.07.005

Boé J (2013) Modulation of soil moisture-precipitation interactions over France by large scale circulation. Clim Dyn 40:875–892. doi: 10.1007/s00382-012-1380-6

Boé J, Habets F (2014) Multi-decadal river flow variations in France. Hydrol Earth Syst Sci 18:691–708. doi: 10.5194/hess-18-691-2014

Botev ZI, Grotowski JF, Kroese DP (2010) Kernel density estimation via diffusion. Ann Stat 38:2916–2957. doi: 10.1214/10-AOS799

Bourgin P, Lobligeois F, Peschard J, et al (2010a) Description des caractéristiques morphologiques, climatiques et hydrologiques de 4436 bassins versants français

Bourgin P, Lobligeois F, Peschard J, et al (2010b) Description des graphiques produits sur les fiches synthsese de 4436 bassins versant français

Bracegirdle TJ, Lu H, Eade R, et al (2016) Do CMIP5 Models Reproduce Observed Low-Frequency North Atlantic Jet Variability ? Geophys Res Lett 45:7204–7212. doi: 10.1029/2018GL078965

Cai M, Huang B (2013) A new look at the physics of rossby waves: A mechanical-coriolis oscillation. J Atmos Sci 70:303–316. doi: 10.1175/JAS-D-12-094.1

Caillouet L, Vidal JP, Sauquet E, Graff B (2016) Probabilistic precipitation and temperature downscaling of the Twentieth Century Reanalysis over France. Clim Past 12:635–662. doi: 10.5194/cp-12-635-2016

Cassou C (2004) Du changement climatique aux régimes de temps : l ' oscillation nord-atlantique. La Météorologie 45:21–32

Cassou C (2010) Euro-Atlantic regimes and their teleconnections Weather regimes : concept and definition North Atlantic-Europe weather regimes. In: ECMWF Seminar on Predictability in the European and Atlantic regions. ECMWF, pp 1–14

Cassou C, Terray L, Hurrell JW, Deser C (2004) North Atlantic winter climate regimes: Spatial asymmetry, stationarity with time, and oceanic forcing. J Clim 17:1055–1068. doi: 10.1175/1520-0442(2004)017<1055:NAWCRS>2.0.CO;2

Champeaux J, Tamburini A (1996) Zonage climatique de la France à partir des séries de précipitations (1971-1990) du réseau climatologique d'Etat. La météorologie 8:44–54

Charney JG, DeVore JG (1979) Multiple Flow Equilibra in the Atmosphere and Blocking. J Atmos Sci 36:1205–1216

Clark MP, Bierkens MFP, Samaniego L, et al (2017) The evolution of process-based hydrologic models: Historical challenges and the collective quest for physical realism. Hydrol Earth Syst Sci 21:3427–3440. doi: 10.5194/hess-21-3427-2017

Colon M, Richard S, Roche PA (2018) The evolution of water governance in France from the 1960s: disputes as major drivers for radical changes within a consensual framework. Water Int 43:109–132. doi: 10.1080/02508060.2018.1403013

Compo GP, Whitaker JS, Sardeshmukh PD, et al (2011) The Twentieth Century Reanalysis Project. Q J R Meteorol Soc 137:1–28. doi: 10.1002/qj.776

Coulibaly P, Burn DH (2004) Wavelet analysis of variability in annual Canadian streamflows. Water Resour Res 40:1–14. doi: 10.1029/2003WR002667

Czaja A, Frankignoul C (1999) Influence of the North Atlantic SST on the atmospheric circulation. Geophys Res Lett 26:2969–2972. doi: https://doi.org/10.1029/1999GL900613

Czaja A, Frankignoul C (2002) Observed impact of Atlantic SST anomalies on the North Atlantic oscillation. J Clim 15:606–623. doi: 10.1175/1520-0442(2002)015<0606:OIOASA>2.0.CO;2

Deser C, Hurrell JW, Phillips AS (2017) The role of the North Atlantic Oscillation in European climate projections. Clim Dyn 49:3141–3157. doi: 10.1007/s00382-016-3502-z

Deser C, Phillips A, Bourdette V (2012) Uncertainty in climate change projections : the role of internal variability. Clim Dyn 38:527–546. doi: 10.1007/s00382-010-0977-x

Dieppois B, Durand A, Fournier M, et al (2014) Low-frequency variability and zonal contrast in Sahel rainfall and Atlantic sea surface temperature teleconnections during the last century. Theor Appl Climatol 121:139–155. doi: 10.1007/s00704-014-1229-5

Dieppois B, Durand A, Fournier M, Massei N (2013) Links between multidecadal and interdecadal climatic oscillations in the North Atlantic and regional climate variability of northern France and England since the 17th century. J Geophys Res Atmos 118:4359–4372. doi: 10.1002/jgrd.50392

Dieppois B, Lawler DM, Slonosky V, et al (2016a) Multidecadal climate variability over northern France during the past 500 years and its relation to large-scale atmospheric circulation. Int J Climatol 36:4679–4696. doi: 10.1002/joc.4660

Dieppois B, Pohl B, Crétat J, et al (2019) Southern African summer-rainfall variability, and its teleconnections, on interannual to interdecadal timescales in CMIP5 models. Clim Dyn 53:3505–3527. doi: 10.1007/s00382-019-04720-5

Dieppois B, Pohl B, Rouault M, et al (2016b) Interannual to interdecadal variability of winter and summer southern African rainfall, and their teleconnections. J Geophys Res Atmos Res 121:6215–6239. doi: 10.1002/2015JD024576.Received

Dieppois B, Rouault M, New M (2015) The impact of ENSO on Southern African rainfall in CMIP5 ocean atmosphere coupled climate models. Clim Dyn 45:2425–2442. doi: 10.1007/s00382-015-2480-x

Dunn JC (1973) A Fuzzy Relative of the ISODATA Process and Its Use in Detecting Compact Well-Separated Clusters A Fuzzy Relative of the ISODATA Process and Its Use in Detecting Compact Well-Separated Clusters. J Cybern 3:37–57

Ebisuzaki W (1997) A Method to Estimate the Statistical Significance of a Correlation When the Data Are Serially Correlated. J Clim 10:2147–2153

Eckmann JP, Oliffson Kamphorst O, Ruelle D (1987) Recurrence plots of dynamical systems. Epl 4:973–977. doi: 10.1209/0295-5075/4/9/004

El Janyani S, Massei N, Dupont JP, et al (2012) Hydrological responses of the chalk aquifer to the regional climatic signal. J Hydrol 464–465:485–493. doi: 10.1016/j.jhydrol.2012.07.040

Emdat Natural disaster database. https://www.emdat.be/index.php

Exner FM, Volken E, Brönnimann S (1913) Über monatliche Witterungsanomalien auf der nördlichen Halbkugel im Winter (On monthly weather anomalies in the Northern Hemisphere in winter). Meteorol Zeitschrift 31:104–109. doi: 10.1127/metz/2015/0654

Feliks Y, Ghil M, Robertson AW (2010) Oscillatory climate modes in the eastern Mediterranean and their synchronization with the North Atlantic Oscillation. J Clim 23:4060–4079. doi: 10.1175/2010JCLI3181.1

Feliks Y, Robertson AW, Ghil M (2016) Interannual variability in north Atlantic weather: Data analysis and a quasigeostrophic model. J Atmos Sci 73:3227–3248. doi: 10.1175/JAS-D-15-0297.1

Folland CK, Knight J, Linderholm HW, et al (2009) The summer North Atlantic oscillation: Past, present, and future. J Clim 22:1082–1103. doi: 10.1175/2008JCLI2459.1

Fritier N, Massei N, Laignel B, et al (2012) Links between NAO fluctuations and inter-annual variability of winter-months precipitation in the Seine River watershed (north-western France). Comptes Rendus - Geosci 344:396–405. doi: 10.1016/j.crte.2012.07.004

Gastineau G, Frankignoul C (2014) Influence of the North Atlantic SST Variability on the Atmospheric Circulation during the Twentieth Century. J Clim 28:1396–1416. doi: 10.1175/JCLI-D-14-00424.1

Gastineau G, Frankignoul C (2012) Cold-season atmospheric response to the natural variability of the Atlantic meridional overturning circulation. Clim Dyn 39:37–57. doi: 10.1007/s00382-011-1109-y

Gentine P, Troy TJ, Lintner BR, Findell KL (2012) Scaling in Surface Hydrology: Progress and Challenges. J Contemp Water Res Educ 147:28–40. doi: 10.1111/j.1936-704x.2012.03105.x

Gettelman A, Rood RB (2016) Demystifying Climate Models. Springer

Ghil M (2019) A Century of Nonlinearity in the Geosciences. Earth Sp Sci 6:1007–1042. doi: 10.1029/2019EA000599

Ghil M (1987) Dynamics, Statistics And Predictability Of Planetary Flow Regimes. In: Irreversible Phenomena and Dynamical Systems Analysis in Geosciences. pp 241–283

Ghil M, Groth A, Kondrashov D, Robertson AW (2018) Extratropical Sub-seasonal to Seasonal Oscillations and Multiple Regimes: The Dynamical Systems View. In: Sub-Seasonal to Seasonal Prediction. Elsevier Inc., pp 119–142

Ghil M, Lucarini V (2019) The Physics of Climate Variability and Climate Change. Arxiv

Giuntoli I, Renard B, Vidal JP, Bard A (2013) Low flows in France and their relationship to large-scale climate indices. J Hydrol 482:105–118. doi: 10.1016/j.jhydrol.2012.12.038

Goodkin NF, Hughen KA, Doney SC, Curry WB (2008) Increased multidecadal variability of the North Atlantic Oscillation since 1781. Nat Geosci 1:844–848. doi: 10.1038/ngeo352

Granger CWJ (1969) Investigating Causal Relations by Econometric Models and Cross-spectral Methods. Econometrica 37:424–438

Grinsted A, Moore JC, Jevrejeva S (2004) Nonlinear Processes in Geophysics Application of the cross wavelet transform and wavelet coherence to geophysical time series. 561–566

Gudmundsson L (2011) Large-Scale Hydrology in Europe. University of Oslo

Gudmundsson L, Tallaksen LM, Stahl K (2011a) Spatial cross-correlation patterns of European low, mean and high flows. Hydrol Process 25:1034–1045. doi: 10.1002/hyp.7807

Gudmundsson L, Tallaksen LM, Stahl K, Fleig AK (2011b) Low-frequency variability of European runoff. Hydrol Earth Syst Sci 15:2853–2869. doi: 10.5194/hess-15-2853-2011

Hannachi A, Straus DM, Franzke CLE, et al (2017) Low-frequency nonlinearity and regime behavior in the Northern Hemisphere extratropical atmosphere. Rev Geophys 55:199–234. doi: 10.1002/2015RG000509

Hannaford J, Buys G, Stahl K, Tallaksen LM (2013) The influence of decadal-scale variability on trends in long European streamflow records. Hydrol Earth Syst Sci 17:2717–2733. doi: 10.5194/hess-17-2717-2013

Hannah DM, Demuth S, van Lanen HAJ, et al (2011) Large-scale river flow archives: Importance, current status and future needs. Hydrol Process 25:1191–1200. doi: 10.1002/hyp.7794

Hauser T, Demirov E, Zhu J, Yashayaev I (2015) North Atlantic atmospheric and ocean inter-annual variability over the past fifty years - Dominant patterns and decadal shifts. Prog Oceanogr 132:197–219. doi: 10.1016/j.pocean.2014.10.008

Hawkins E, Sutton R (2009) The Potential to Narrow Uncertainty in Regional Climate Predictions. Bull Am Meteorol Soc 1095–1107. doi: 10.1175/2009BAMS2607.1

Hermida L, López L, Merino A, et al (2015) Hailfall in southwest France : Relationship with precipitation , trends and wavelet analysis. Atmos Res 156:174–188. doi: 10.1016/j.atmosres.2015.01.005

Hingray B, Blanchet J, Evin G, Vidal JP (2019) Uncertainty component estimates in transient climate projections: Precision of estimators in a single time or time series approach. Clim Dyn 53:2501–2516. doi: 10.1007/s00382-019-04635-1

Hubert P (2001) Les multifractals, un outil pour surmonter les problèmes d'échelle en hydrologie. Hydrol Sci J 46:897–905. doi: 10.1080/02626660109492884

Hubert P, Carbonnel JP, Chaouche A (1989) Segmentation Des Series Hydrometeorologiques - Application a des Series de Precipitations et de Debits de L'Afrique de l'Ouest. J Hydrol 110:349–367

Hurrell JW (1995) Decadal Trends in the North Atlantic Oscillation: Regional Temperatures and Precipitation. Science (80-) 269:676–679

Hurrell JW, Deser C (2014) Northern Hemisphere climate variability during winter: Looking back on the work of Felix Exner. Meteorol Zeitschrift 24:113–118. doi: 10.1127/metz/2015/0578

Hurrell JW, Deser C (2009) North Atlantic climate variability: The role of the North Atlantic Oscillation. J Mar Syst 79:231–244. doi: 10.1016/j.jmarsys.2009.11.002

Hurrell JW, Kushnir Y, Ottersen G, Visbeck MH (2003) The North Atlantic Oscillation: Climatic Significance and Environment Impact. American Geophysical Union, Washington, DC

Hurrell JW, Van Loon H (1997) Decadal variations in climate associated with the North Atlantic oscillation. Clim Change 36:301–326. doi: 10.1007/978-94-015-8905-5_4

Ionita M, Tallaksen LM, Kingston DG, et al (2017) The European 2015 drought from a climatological perspective. Hydrol Earth Syst Sci Discuss 0:1–32. doi: 10.5194/HESS-2016-218

IPCC (2007) Climate Change 2007: The Physical Science Basis

IPCC (2014) Climate change 2014. Synthesis report.

Joly D, Brossard T, Cardot H, et al (2010) Les types de climats en France , une construction spatiale. Cybergeo Eur J Geogr 501. doi: 10.4000/cybergeo.23155

Kaufman L, Rousseeuw PJ (1990) Finding Groups in Data: An Introduction to Cluster Analysis (Wiley Series in Probability and Statistics)

Kavvada A, Ruiz-Barradas A, Nigam S (2013) AMO's structure and climate footprint in observations and IPCC AR5 climate simulations. Clim Dyn 41:1345–1364. doi: 10.1007/s00382-013-1712-1

Kennel MB, Brown R, Abarbanel HDI (1992) Determining embedding dimension for phase-space reconstruction using a geometrical construction. Phys Rev A 45:3404–3413. doi: 10.1103/physreva.45.3403

Kingston D, Hannah D (2006) Interactions between large-scale climate and river flow across the northern North Atlantic margin. Clim Var … 350–355

Kingston DG, Massei N, Dieppois B, et al (2020) Moving beyond the catchment scale: value and opportunities in large-scale hydrology to understand our changing world. Hydrol Process

Kingston DG, McGregor GR, Hannah DM, Lawler DM (2007) Large-Scale Climatic Controls on New England River Flow. J Hydrometeorol 8:367–379. doi: 10.1175/JHM584.1

Kingston DG, McGregor GR, Hannah DM, Lawler DM (2006) River flow teleconnections across the northern North Atlantic region. Geophys Res Lett 33:1–5. doi: 10.1029/2006GL026574

Kondrashov D, Ide K, Ghil M (2004) Weather regimes and preferred transition paths in a three-level quasigeostrophic model. J Atmos Sci 61:568–587. doi: 10.1175/1520-0469(2004)061<0568:WRAPTP>2.0.CO;2

Kushnir Y, Robinson WA, Bladé I, et al (2002) Atmospheric Gcm Response To Extratropical Sst Anomalies : Synthesis and Evaluation. Am Meteorol Soc 15:2233–2256

Laaha G, Gauster T, Tallaksen LM, et al (2017) The European 2015 drought from a hydrological perspective. Hydrol Earth Syst Sci 21:3001–3024. doi: 10.5194/hess-21-3001-2017

Labat D (2006) Oscillations in land surface hydrological cycle. Earth Planet Sci Lett 242:143–154. doi: 10.1016/j.epsl.2005.11.057

Labat D (2000) Non-Linéarité et Non-Stationnarité en Hydrologie Karstique. INP Toulouse

Labat D (2008) Wavelet analysis of the annual discharge records of the world's largest rivers. Adv Water Resour 31:109–117. doi: 10.1016/j.advwatres.2007.07.004

Labat D, Ababou R, Mangin A (2000) Rainfall-runoff relations for karstic springs. Part I: Convolution and spectral analyses. J Hydrol 238:123–148. doi: 10.1016/S0022-1694(00)00321-8

Lars V. ahlfors (1973) Conformal invariants. McGraw-Hill

Lavers D, Prudhomme C, Hannah DM (2010) Large-scale climate, precipitation and British river flows: Identifying hydroclimatological connections and dynamics. J Hydrol 395:242–255. doi: 10.1016/j.jhydrol.2010.10.036

Lavers D, Prudhomme C, Hannah DM (2013) European precipitation connections with large-scale mean sea-level pressure (MSLP) fields. Hydrol Sci J 58:310–327. doi: 10.1080/02626667.2012.754545

Lavers DA, Villarini G (2015) The contribution of atmospheric rivers to precipitation in Europe and the United States. J Hydrol 522:382–390. doi: 10.1016/j.jhydrol.2014.12.010

Legras B, Ghil M (1985) Persistent Anomalies, Blocking and Variations in Atmosphere Predictability. J Atmos Sci 42:433–471

Lionello P, P.Malanotte-rizzoli, R.Boscolo (2006) Mediterranean climate Variability. Elsevier

Liu D, Graham J (2018) Simple Measures of Individual Cluster-Membership Certainty for Hard Partitional Clustering. Am Stat 1–10. doi: 10.1080/00031305.2018.1459315

Lloyd-Hughes B, Prudhomme C, Hannaford J, et al (2009) The Spatial Coherence of European Droughts – Final Report protecting and improving the environment in England and Wales. Sci Rep SC070079/S:Enviroment Agency, Bristol

López J, Francés F, L??pez J, et al (2013) Non-stationary flood frequency analysis in continental Spanish rivers, using climate and reservoir indices as external covariates. Hydrol Earth Syst Sci 17:3189–3203. doi: 10.5194/hess-17-3189-2013

Lorenz EN (1963) Deterministic Nonperiodic Flow. J Atmos Sci 20:130–141. doi: https://doi.org/10.1175/1520-0469(1963)020<0130:DNF>2.0.CO;2

Mann ME (2019) The Weather Amplifier. Sci Am 320:42–49. doi: 10.1038/scientificamerican0319-42

Mann ME, Rahmstorf S, Kornhuber K, et al (2018) Projected changes in persistent extreme summer weather events: The role of quasi-resonant amplification. Sci Adv 4:1–10. doi: 10.1126/sciadv.aat3272

Maraun D, Kurths J, Holschneider M (2007) Nonstationary Gaussian processes in wavelet domain: Synthesis, estimation, and significance testing. Phys Rev E - Stat Nonlinear, Soft Matter Phys 75:1–14. doi: 10.1103/PhysRevE.75.016707

Mares I, Mares C, Mihailescu M (2002) NAO impact on the summer moisture variability across Europe. Phys Chem Earth 27:1013–1017. doi: 10.1016/S1474-7065(02)00135-3

Massei N, Dieppois B, Hannah DM, et al (2017) Multi-time-scale hydroclimate dynamics of a regional watershed and links to large-scale atmospheric circulation: Application to the Seine river catchment, France. J Hydrol 546:262–275. doi: 10.1016/j.jhydrol.2017.01.008

Massei N, Durand A, Deloffre J, et al (2007) Investigating possible links between the North Atlantic Oscillation and rainfall variability in Northwestern France over the past 35 years. J Geophys Res Atmos 112:1–10. doi: 10.1029/2005JD007000

Massei N, Fournier M (2012) Assessing the expression of large-scale climatic fluctuations in the hydrological variability of daily Seine river flow (France) between 1950 and 2008 using Hilbert-Huang Transform. J Hydrol 448–449:119–128. doi: 10.1016/j.jhydrol.2012.04.052

Massei N, Laignel B, Deloffre J, et al (2010) Long-term hydrological changes of the Seine River flow (France) and their relation to the North Atlantic Oscillation over the period 1950-2008. Int J Climatol 30:2146–2154. doi: 10.1002/joc.2022

Maurice Pardé (1933) Fleuves et rivières, Armand Col. Armand Colin

McGregor G (2017) Hydroclimatology, modes of climatic variability and stream flow, lake and groundwater level variability: A progress report. Prog Phys Geogr 41:496–512. doi: 10.1177/0309133317726537

Mediero L, Kjeldsen TR, Macdonald N, et al (2015) Identification of coherent flood regions across Europe by using the longest streamflow records. J Hydrol 528:341–360. doi: 10.1016/j.jhydrol.2015.06.016

Meehl GA, Goddard L, Boer G, et al (2014) Decadal climate prediction an update from the trenches. Bull Am Meteorol Soc 95:243–267. doi: 10.1175/BAMS-D-12-00241.1

Michael Ghil, Childress S (1987) Topics in Geophysical Fluid Dynamics: Atmospheric Dynamics, Dynamo Theory, and Climate Dynamics. Springer

Mo KC, Ghil M (1987) Statistics and dynamics of persistent anomalies. J. Atmos. Sci. 44:877–901

Mo KK, Ghil M (1988) Cluster Analysis of Multiple Planetary Flow Regimes. J Geophys Res 93:10927–10952

Monti S, Tamayo P, Mesirov J, Golub T (2003) Consensus clustering: A resampling-based method for class discovery and visualization of gene expression microarray data. Mach Learn 52:91–118. doi: 10.1023/A:1023949509487

Moron V, Robertson AW, Ward MN, Camberlin P (2007) Spatial coherence of tropical rainfall at the regional scale. J Clim 20:5244–5263. doi: 10.1175/2007JCLI1623.1

Nakamura H, Nakamura M, Anderson JL (1997) The role of high- and low-frequency dynamics in blocking formation. Mon Weather Rev 125:2074–2093. doi: 10.1175/1520-0493(1997)125<2074:TROHAL>2.0.CO;2

Noether E (1971) Invariant Variation Problems. Transp Theory Stat Phys 1:186–207. doi: 10.1080/00411457108231446

Norbury J, Roulstone I (2002) Large-Scale Atmosphere – Ocean Dynamics , Volume I. 400

OECD (2013) Water and Climate Change Adaptation: Policies to Navigate Uncharted Waters

Paluš M (2014) Cross-scale interactions and information transfer. Entropy 16:5263–5289. doi: 10.3390/e16105263

Paluš M, Kravtsov S, Sugihara G, et al (2018) Synchronization and causality across time scales in El Niño Southern Oscillation. npj Clim Atmos Sci 1:33. doi: 10.1038/s41612-018-0043-7

Park TW, Ho CH, Deng Y (2014) A synoptic and dynamical characterization of wave-train and blocking cold surge over East Asia. Clim Dyn 43:753–770. doi: 10.1007/s00382-013-1817-6

Percival DB, Walden AT (2000) Wavelet methods for time series analysis. Cambridge university press, London

Petoukhov V, Rahmstorf S, Petri S, Schellnhuber HJ (2013) Quasiresonant amplification of planetary waves and recent Northern Hemisphere weather extremes. Proc Natl Acad Sci U S A 110:5336–5341. doi: 10.1073/pnas.1222000110

Pikovsky A, Rosenblum M, Kurths J (2001) Synchronization. A Universal Concept in Nonlinear Sciences. Cambridge University Press: Cambridge

Polo I, Schiemann R (2013) Characterization of Euro-Atlantic Weather Regimes : understanding variability at different timescales

Rahiz M, New M (2012) Spatial coherence of meteorological droughts in the UK since 1914. Area 44:400–410. doi: 10.1111/j.1475-4762.2012.01131.x

Rand D, Young L-S (1980) Dynamical systems and turbulence. Springer

Richard S, Bouleau G, Barone S (2010) Water governance in France: institutional framework, stakeholders, arrangements and process. Water Gov public policies Lat Am Eur Jacobi P Sinisgali P(Eds) 137–178

Robertson AW, Vitart F (2019) Sub-seasonal to Seasonal prediction: The Gap between Weather and Climate Forecasting. Elsevier, Amsterdam,Oxford,Cambridge

Sauquet E, Gottschalk L, Krasovskaia I (2008) Estimating mean monthly runoff at ungauged locations: an application to France. Hydrol Res 39:403–423. doi: 10.2166/nh

Schaefli B, Maraun D, Holschneider M (2007) What drives high flow events in the Swiss Alps? Recent developments in wavelet spectral analysis and their application to hydrology. Adv Water Resour 30:2511–2525. doi: 10.1016/j.advwatres.2007.06.004

Şenbabaoğlu Y, Michailidis G, Li JZ (2014) Critical limitations of consensus clustering in class discovery. Sci Rep 4:. doi: 10.1038/srep06207

Shorthouse CA, Arnell NH (1997) Spatial and temporal variability in European river flows and the North Atlantic Oscillation. FRIEND 97 - Reg Hydrol Concepts Model Sustain Water Resour Manag IAHS Publ 246:

Shutts G j. (1983) The propagation of eddies in diffluent jetstreams: eddy vorticity forcing of "blocking" flow fields. Q J R Meteorol Soc 109:737–761. doi: 10.1256/smsqj.46203

Sidibe M, Dieppois B, Eden J, et al (2019) Interannual to Multi-decadal streamflow variability in West and Central Africa: Interactions with catchment properties and large-scale climate variability. Glob Planet Change 177:141–156. doi: 10.1016/j.gloplacha.2019.04.003

Slimani S, Massei N, Mesquita J, et al (2009) Combined climatic and geological forcings on the spatio-temporal variability of piezometric levels in the chalk aquifer of Upper Normandy (France) at pluridecennal scale. Hydrogeol J 17:1823–1832. doi: 10.1007/s10040-009-0488-1

Smith L, Turcotte D, Isacks B (1998) Stream flow characterization and feature detection using a discrete wavelet transform. Hydrol Process 12:233–249. doi: 10.1002/(SICI)1099-1085(199802)12:2<233::AID-HYP573>3.0.CO;2-3

Snelder TH, Lamouroux N, Leathwick JR, et al (2009) Predictive mapping of the natural flow regimes of France. J Hydrol 373:57–67. doi: 10.1016/j.jhydrol.2009.04.011

Sotero RC (2016) Topology, Cross-Frequency, and Same-Frequency Band Interactions Shape the Generation of Phase-Amplitude Coupling in a Neural Mass Model of a Cortical Column. PLoS Comput Biol 12:1–29. doi: 10.1371/journal.pcbi.1005180

Stahl K, Hisdal H, Hannaford J, et al (2010) Streamflow trends in Europe: Evidence from a dataset of near-natural catchments. Hydrol Earth Syst Sci 14:2367–2382. doi: 10.5194/hess-14-2367-2010

Stephenson DB, Hannachi A, Gate E (2004) On the existence of multiple climate regimes. Q J R Meteorol Soc 130:583–605. doi: 10.1256/qj.02.146

Stephenson K (2007) Random Triangulations and Emergent Conformal Structure. In: Computational Conformal Geometry Conference, Stony Brook

Sun C, Li J, Fei F (2015) A delayed oscillator model for the quasi‐periodic multidecadal variability of the NAO. Clim Dyn 2083–2099. doi: 10.1007/s00382-014-2459-z

Sutton R, Dong B (2012) Atlantic Ocean influence on a shift in European climate in the 1990s. Nat Geosci 5:788–792. doi: 10.1038/ngeo1595

Sutton RT, Hodson DLR (2005) Atlantic Ocean Forcing of North American and European Summer Climate. Science (80-) 309:115–118. doi: 10.1126/science.1109496

Szolgayova E, Laaha G, Blöschl G, Bucher C (2014a) Factors influencing long range dependence in streamflow of European rivers. Hydrol Process 28:1573–1586. doi: 10.1002/hyp.9694

Szolgayova E, Parajka J, Blo¨schl G, et al (2014b) Long term variability of the Danube River flow and its relation to precipitation and air temperature. J Hydrol 519:871–880. doi: 10.1016/j.jhydrol.2014.07.047

Torrence C, Compo G ~P. (1998) A Practical Guide to Wavelet Analysis. Bull Am Meteorol Soc 79:61–78. doi: 10.1175/1520-0477(1998)079<0061:APGTWA>2.0.CO;2

Ullmann A, Fontaine B, Roucou P (2014) Euro-Atlantic weather regimes and Mediterranean rainfall patterns: Present-day variability and expected changes under CMIP5 projections. Int J Climatol 34:2634–2650. doi: 10.1002/joc.3864

van der Wiel K, Bloomfield HC, Lee RW, et al (2019) The influence of weather regimes on European renewable energy production and demand. Environ Res Lett 14:094010. doi: 10.1088/1748-9326/ab38d3

Vautard R (1990) Multiple Weather Regimes over the North Atlantic: Analysis of Precursors and Successors. Mon Weather Rev 118:2056–2081

Vautard R, Gobiet A, Jacob D, et al (2013) The simulation of European heat waves from an ensemble of regional climate models within the EURO-CORDEX project. Clim Dyn 41:2555–2575. doi: 10.1007/s00382-013-1714-z

Vidal JP, Martin E, Franchistéguy L, et al (2010) A 50-year high-resolution atmospheric reanalysis over France with the Safran system. Int J Climatol 30:1627–1644. doi: 10.1002/joc.2003

Visbeck MH, Hurrell JW, Polvani L, Cullen HM (2001) The North Atlantic Oscillation: past, present, and future. Proc Natl Acad Sci U S A 98:12876–12877. doi: 10.1073/pnas.231391598

Wang L, Zhang Y, Feng J (2005) On the Euclidean distance of images. IEEE Trans Pattern Anal Mach Intell 27:1334–1339. doi: 10.1109/TPAMI.2005.165

Weeks ER, Tian Y, Urbach JS, et al (1997) Transitions between blocked and zonal flows in a rotating annulus with topography. Science (80-) 278:1598–1601. doi: 10.1126/science.278.5343.1598

Wills RC, Schneider T, Wallace JM, et al (2018) Disentangling Global Warming, Multidecadal Variability, and El Niño in Pacific Temperatures. Geophys Res Lett 45:2487–2496. doi: 10.1002/2017GL076327

Woollings T, Franzke C, Hodson DLR, et al (2015) Contrasting interannual and multidecadal NAO variability. Clim Dyn 45:539–556. doi: 10.1007/s00382-014-2237-y

Yang H (2011) Multiscale recurrence quantification analysis of spatial cardiac vectorcardiogram signals. IEEE Trans Biomed Eng 58:339–347. doi: 10.1109/TBME.2010.2063704

List of Figures & Tables

SUPPLEMENTARY MATERIAL

S1: Theoretical reflexion on extremal length and dynamics of a physical system

Introduction

Emmy Noether (1971) in her pioneering works has shown that the conservation laws of physics are analogue to geometrical symmetries. Since the Lagrangian and Hamiltonian formalisms allow for the representation of a system's dynamics under a purely geometrical point of view, by the configuration and phase spaces of the system, it is possible, from geometry, to gather some insight into the equations of motions of the system. The comes in handy when one wants to decreases the number of degrees of freedom of the system, but applying constraints on the equations of motion, or equivalently, forcing some symmetries in the geometrical setting. Conformal constraints have led to the development of Conformal Field Theories, which are of great importance for quantum gravitation, string theory or critical phenomena. Except for Conformal Field Theories, most of the conformal constraints considered in those fields concern infinitesimal conformal transformations, and thus, do not force the conformal symmetry to be global. In this study, we use a global conformal invariant, the extremal length.

The extremal length concept has been introduced in the continuous setting by [2], and is the extension of the concept of length invariance in $SO(3)$ to the angle-preserving conformal group ($Conf(3)$). The theory was later expanded to the discrete setting by [3]. The correspondence of the extremal length with physical laws have been investigated in potential theory [4], critical phenomena [5], knot theory or hydrodynamics [6]. In fluid mechanics, extremal length in the context of conformal, quasi-conformal mappings is used to simplify computations. The physical domain is mapped into a conformal domain (disk or rectangle), and the extremal length becomes a parameter of the equations of motions in the canonical domain [7]. Outside of physics, the conformal invariance of extremal length has been used for registration in medical sciences [8],

[9]. The works of [2] have allowed to give the extremal length, a physical analogue: electrical resistivity. The latter analogy is often quoted in studies using extremal length to give it a more intuitive interpretation. However, there have been very few studies that take the extremal length concept [2] and associate it with the spatiotemporal dynamics of a physical system. A large body of studies in statistical physics has linked the extremal length to Brownian motion at criticality [10]–[12]. Those studies concentrate on critical phenomena, i.e. dynamics of a physical system between phase's transitions. In the present study, we present, for the lack of rigorous demonstration, a set of theoretical reflections, on how the extremal length constraint can be enforced on the dynamics of a system, and what are the consequences of those constraints. This part will be organized as follows. In section 1, we will present the concept of extremal length. In section 2, we present our reflections on the link between extremal length and a system's dynamics, *i.e.* its equations of motion. We then present what are the spatial and dynamical changes corresponding to some extremal length levels, in Section 3. In section 4, we discuss the consequences of the constraints imposed by extremal length on the quasi-geostrophic equation for atmospheric circulation. Section 5 presents the algorithm for approximating the extremal length of a discrete surface, as well as the conjecture by Kenneth Stephenson, on which the algorithm is based.

1. The notion of extremal length

Ahlfors (1973) introduced a number of conformal invariants, that is, measures which do not change under a conformal map. Any surface in $\mathbb{R}^3$ whose local angles are independent of the local coordinate system (called a chart) chosen is said to be equipped with a conformal structure. If one create two different charts of the same region of a surface with a conformal structure, the angle of two curves intersecting at one point will be measured the same. A surface with a conformal structure embedded in $R^3$is called a Riemannian surface (Figure S1.1).

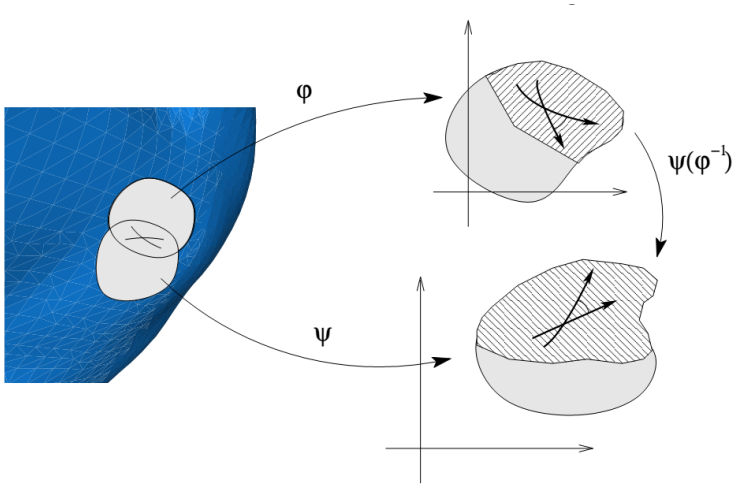

Figure S1.1. Two charts covering a subset of a surface equipped with a conformal structure. *Two charts* $\boldsymbol{\phi}$ *and* $\boldsymbol{\Psi}$ *give two different coordinates for the same region of the surface. However, the angle measured at the intersection of the two lines is equal in both charts albeit the orientation and length of the curves is not necessarily the same. (Courtesy of Kenneth Stephenson)*

A surface with a conformal structure can be transformed by a map that will preserve, locally, the orientation of the angles. A conformal map $f: S \to S'$ from a surface S to a surface S' is a local angle preserving map. By local we mean that at a point $x \in S$ and a point $x' \in S'$ any two curves intersecting at x will have the same angle at x'. Thus "local" here means the S^n ball around x (resp. x') .In the discrete setting, this neighbourhood is limited to the angles of edges that are connected to x (resp. x'); neighbouring points are not part of that neighbourhood. As a consequence, there is no restriction to keep the length of edges or angles between nodes invariant under such map. Thus, two surfaces S and S' may have very different global shapes, yet have identical local structure. In that case we say that S and S' are conformal equivalent.

Each geopotential height time step is a Riemannian surface. The Uniformization theorem [14], [15] states any two Riemannian surfaces of the same genus can be locally conformally mapped onto each other. This means that any Riemannian surface is a conformal equivalent of another. An global constraint is thus needed to restrict the number of conformal equivalent surfaces within our time series. The "extremal length" [13] is such a constraint that brings additional information about the global structure of a Riemannian surface. The extremal length is a conformal invariant, i.e. if $f: S \to S'$ is a conformal map then $el(S) = el(S')$. Thus, two surfaces having the same extremal length are also conformal equivalent (globally). The following presentation of the extremal length is based on [13].

Definition 1.1 Let Q be a topological quadrilateral with its four ordered corners $\{q1, q2, q3, q4\}$ identified (Figure S1.2). Let $\{q1, q4\}$ and $\{q2, q3\}$ be the opposite edges L, R respectively. By exclusion, this defines T, B as the orthogonal edges to L and R respectively. Let $\Gamma: \{\gamma_1 \dots \gamma_2\}$ be a collection of curves joining sides L and R. We are interested in finding curves whose length will not change under a conformal map. The Euclidean length is not invariant under conformal maps so another length must be found. In order to find such length we search for conformal metrics that are conformal equivalent to the Euclidean one i.e. $ds = \rho|dz|$, ds is the conformal metric, $|dz|$ the absolute value of the Euclidean metric (which is δ_j^i) and ρ the conformal factor. A metric tensor, or "metric" is a function that take two vectors as inputs and outputs a scalar. The metric generalizes the notion of scalar product and allows the computation of angles and distances on any surface that admits such a metric. The easiest and most common one is the Euclidean metric. For a 2-dimensional space with coordinates x, y, the metric is of the form $g = \begin{bmatrix} 1 & 0 \\ 0 & 1 \end{bmatrix}$. The length of a curve is then $L = \int_a^b \sqrt{dx^2 + dy^2}$. We are searching for the family of metrics that are conformal to g that is, metrics that do not change the measure of angles (i.e. doesn't change the $[x, y] = [y, x]; x \neq$

y that is, the symmetry of the Euclidean metric). The only possible change is the conformal factor ρ.

We define the following quantities:

The ρ-length of curve γ_i: $L(\gamma,\rho)=\int_\gamma \rho|dz|$

The ρ-area of Q: $A(Q,\rho)=\iint_Q \rho dxdy$

The ρ-minimum length $L(\Gamma,\rho)=inf.L(\gamma,\rho)$

The extremal length between L and R (hereinafter: extremal length) of a topological quadrilateral is defined as:

$$\lambda(Q)=\frac{sup.\{\rho\}L(\Gamma,\rho)}{A(Q,\rho)} \quad (1.1)$$

The numerator means that one select the ρ that give the largest minimum length $L(\Gamma,\rho)$. The denominator is simply the area in the selected ρ.

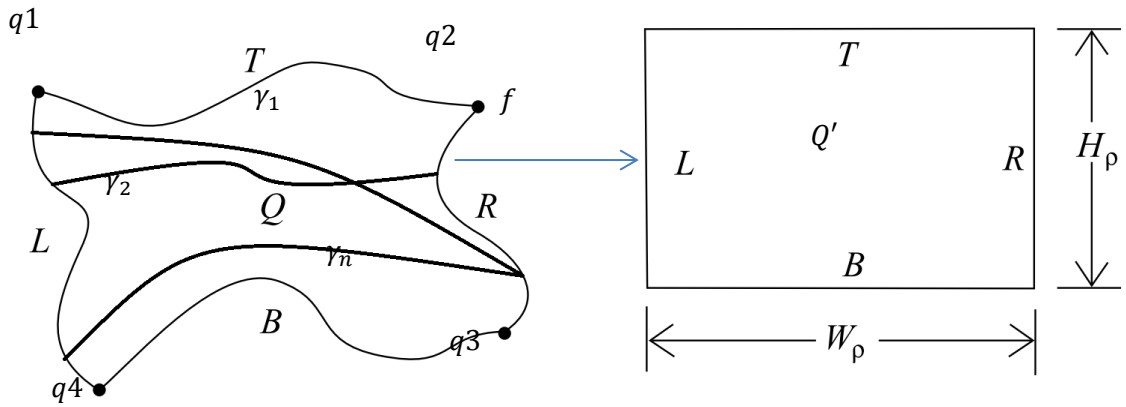

Figure S1.2. *The conformal mapping* $\boldsymbol{f}(\{\boldsymbol{Q},\boldsymbol{q1},\boldsymbol{q2},\boldsymbol{q3},\boldsymbol{q4}\}):\boldsymbol{Q}\rightarrow\boldsymbol{Q'}$ *. The conformal map* $\boldsymbol{f}:\boldsymbol{Q}\rightarrow\boldsymbol{Q'}$ *conserves the extremal length of* $\boldsymbol{Q}$*. The curves* $\boldsymbol{\gamma_{i..n}}$ *are straight lines from* $\boldsymbol{L}$ *to* $\boldsymbol{R}$*. The extremal length in* $\boldsymbol{Q'}$ *is* $\boldsymbol{W_\rho/H_\rho}$*. (Adapted from Cannon et al. (1996))*

Let's note that $\lambda(L,R)=\frac{1}{\lambda(T,B)}$. The extremal length between T,B is thus the inverse of the one between L,R. The former is referenced to as "conformal modulus" in the literature and

several important properties about extremal length were discovered studying either the extremal length or the conformal modulus.

2. Extremal length constraints on the dynamics of a system

2.1.Geometric and complex analysis generalities

We briefly introduce the objects used in this section as well as their notations. We denote by S a surface, which here correspond to a z500 snapshot. A surface is a manifold M that is orientable, 2-dimensional, and on which a metric can be defined. S is the image of a 2-dimensional scalar field function $\Phi(x, y) = z500_{x,y}$ where x, y are latitude on longitude, respectively. This makes S, a surface embedded in the three dimensional space $\mathbb{R}^3$. We also call S a hypersurface. The local geometry of a point $x \in S$, is included into an $\mathbb{R}^3$ ball of radius r centred on x. The radius r is made as small as possible and we call the volume contained in the ball, the neighbourhood of x. If x is surrounded by n other identified points $x'_{i..n}$, the neighbourhood usually excludes those points and thus, the study of the neighbourhood of x is that of the transition between x and the surrounding points. Because a hypersurface can have local curvature, the Euclidean metric may locally fail to compute angles and distances in the neighbourhood of x. In order to deal with that limitation, we project x and its neighbourhood to a flat vector space TS_x tangent to x. Being a vector space, the Euclidean metric is admissible, as well as all linear algebra operations associated with any vector space, so that computation of angles and distances is possible. To each point $x_{i..N} \in S$, is associated a tangent vector space TS_{x_i}. For example, on the unit disk, the tangent vector spaces to each point are simply the tangents to those points.A local, (conformal) transformation at point $x \in S$ is a transformation of its neighbourhood. The point x itself is not transformed, and we say that this point is the identity Id. For example, in the set of natural numbers $\mathbb{N}$, the number 1 is identity because, for any number $a \in \mathbb{N} \rightarrow a * 1 = a$. Many transformations share similar characteristics. For example, rigid motion transformation keep

angles and distance unchanged and are composed of rotations and translations only. Conformal transformations are those that keep angles unchanged. Thus, instead of speaking a precise transformation, we usually regroup all transformations that share the same characteristics into a group G. That group G "acts" on S by transforming the neighbourhood of either a part of all points of $x_{i\dots N} \in S$. The group G is composed of mathematical objects that actually transform the coordinates of the neighbourhood. For conformal transformations on hypersurfaces, G is composed of $n * n$ matrices. The group of conformal transformations is called the conformal group and has several notations, one of them being $Conf(2)$. The number 2 is for the number of independent dimensions the group is acting on. The group G is a manifold in its own right, thus, the same problem as with S arises: Computing angles and distance in the neighbourhood of a transformation matrix may not be possible and so a map to a tangent vector space (just as the vector space TS_x) at a point $q \in G$ is needed. The tangent vector space at q is called the Lie algebra of G at q and denoted $\mathfrak{g}(q)$. Each basis vector $\boldsymbol{q}_{i..d} \in \mathfrak{g}(q); d = 1,2$ represents a fundamental transformation, that is, a transformation that cannot be composed of others. We call those fundamental transformations, the generator of $G(q)$. Thus, each transformation matrix at a point $q \in G$is represented by a linear combination of the generators. For example, in the conformal group $conf(2)$, the generators are those of translations, dilations, rotations and special conformal transformations. At each point in the neighbourhood of $\mathfrak{g}(q)$ is associated a vector, being a linear combination of the basis vectors $\boldsymbol{q}$. This collection of vectors is called the vector field $\boldsymbol{V}_q$. Since a point $q \in G$ acts on the point $x \in S$, thus the vector field $\boldsymbol{V}_q$can be seen as a map $\boldsymbol{V}_q(x): x \in S \mapsto G_q(x), q \in G$ that transforms the neighbourhood of $x \in S$.

For the sake of simplicity, let's say the map $\boldsymbol{V}_q(x)$ acts directly on x and results in a single vector instead of a vector field. Then, all $\boldsymbol{V}$ maps form a vector field on S. The collection of all possible maps $\{\boldsymbol{V}\}$ is called the tangent bundle TS of S. A set of Mobius transformations

occurring at all points of S can be seen as one realization of the tangent bundle TS_G. We call that realization a bundle section.

Any vector space V can be described equally by its dual $V*$. A dual is the space of vector-valued functions that output a scalar. An intuitive way of seeing a dual space is by visualizing a vector that goes through surface orthogonal to V basis. The number of surfaces that the vector goes through is the output of the vector-valued function on the dual space $V*$. The vector space generalizes the idea of the derivative, while its dual generalizes the idea of differential (*i.e.*the gradient of a vector). The dual of a vector space is the co-vector space and that of a tangent bundle, a co-tangent bundle.

While the coordinates of any point on the hypersurface S can be identified by its scalar field function $\Phi(x, y)$, the local coordinates of a tangent space TS_x cannot be compared to those of a tangent space $TS_{x'}$ without properly defining a map between them, that is, a derivative and the associated differential. This is because tangent spaces may not be parallel to each other (think about the unit disk example, the tangents are not parallel to each other). If there is curvature, then the usual derivative $\frac{f(x+h)-f(x)}{h}; h \to 0$ is not possible, and a more sophisticated derivative is needed. The covariant derivative $\nabla \boldsymbol{u} \boldsymbol{V}_q$takes the vector field $\boldsymbol{V}_q$ along the vector $\boldsymbol{u}$ (*i.e.* along a direction and distance) but satisfying some requirements that the tangent vector field $\boldsymbol{V}_q$ always stays parallel to $\boldsymbol{u}$.

We end up this short introduction by speaking of complex analysis. The tangent spaces of our surface S will be treated as complex spaces, in two flavours: The most recurrent, will be the upper half plane $\mathbb{C}^+$ where the coordinates of a point are of the form $z = x + iy$; The latter will be the extended complex plane; The is the complex plane $\mathbb{C}$ with a point at infinity added. The latter is important for conformal transformations that need to be defined relative to more than one fixed point (hence the addition of a point to infinity). It can be pictured as the Riemann sphere (the $\mathbb{S}^2$ sphere) where the poles are either 0 or ∞.

The study of (conformal) transformations is akin to the study of (conformal) maps.

We recall that maps can be broken down in both functions and morphisms. Morphisms are usually seen as a more general type of maps, while functions usually have their codomain (the domain of their image) as a set of numbers (c.f. $\mathbb{R}, \mathbb{C}$). We will use both functions and morphisms as maps through the following sections. The maps have to satisfy certain requirements, most notably concerning their differentiability. We give some examples of (complex) maps and their properties.

A holomorphic function is a complex-valued function that is, at every point of its domain, continuously complex differentiable. A meromorphic function is an holomorphic function except at some isolated points, which are called the poles of the functions. The poles of a function are the inverses of its zeros. A Harmonic function, is a twice differentiable function satisfying at every point of the domain, the Laplace equation, *i.e.*$\Delta f = 0$ with $\Delta = \frac{\partial^2 f}{\partial x_1^2} + \frac{\partial^2 f}{\partial x_2^2} \ldots + \frac{\partial^2 f}{\partial x_d^2}$, or equivalently, the Euler-Lagrange equation $L_q - \frac{d}{dt} L_{\dot{q}} = 0$, $L: L(t, q, \dot{q})$ being the Lagrangian, with $L = T - V$; T the total kinetic energy of the system, and V, the potential energy of the system.

A homorphism is a map between two identical structures (such as vector spaces, groups, and so on…) that preserve the structures. Several types of morphisms exist such as isomorphisms, which are smooth maps between manifolds both in the direct and inverse directions, or automorphisms which are isomorphisms with the added property that the target domain of the map is the same as the domain of the source.

2.2. Conformal transformations and dynamics

2.2.1. Definition of dynamics and their change

In the following, we refer to "dynamics" as the time evolution of a system, the latter being, for the purpose of our study, being defined as a set of N independent generic particles. The evolution in time of the system is described by its equations of motion, which are composed of parameters (dependent on time or not), coordinates, and can have various forms, such as linear or non-linear, first order or higher, ordinary differential or partial differential and so on. The evolution in time of the d-dimensional coordinates of the system's particles is represented in a configuration space, a dN-dimensional manifold. The phase space adds to the configuration space, the velocities associated with each particle at each point in the configuration space. Thus, the evolution in time of the system, its dynamics, can be represented by a function (a trajectory) function of position, velocity, and, implicitly, time. Under this formalism, the equations of motion are described in a purely geometric way, and a bridge between physical laws and geometrical objects is created, a bridge pioneered by the works of Noether (1971). In a N particles system, the degrees of freedom equals the number of particles, *i.e.* there are N degrees of freedom, which makes description of the dynamics very complex, with the necessity to resort to statistical techniques to describe them. However, if m constraints are applied on the equations of motion, the number of degrees of freedom is reduced to $N - m$ degrees of freedom. A powerful constraint applied on dynamics is that of conserved quantities such as total energy, momentum, angular momentum and so on. When such constraint is enforced on the equation of motion, we get conservation laws. In the geometrical setting, conservation laws are analogue to geometrical symmetries, *i.e.* geometrical transformations that leave a geometrical object invariant (up to some parameter).

The consequence is that when the equations of motion are conservations laws, the dynamics are invariant, *i.e.* they do not change in time. The term "change of dynamics" is usually

employed ambiguously, so a clarification is needed. We may distinguish "dynamics of change" and "change in dynamics", both are of relevance in our context. The phase-space of a system enables to identify each expression with a precise characteristic [17]. The dynamics of change refer to the successive positions, in the phase space, of observation points. For instance, the observation of student's marks over the years may reveal that average marks decrease as years have passed. Change in dynamics refers to the evolution of marks' distribution between matters as years have passed. For instance, science related matters may have had the highest marks at the beginning of the observations, but later, social sciences may become the ones with the highest marks. In this case, the mechanisms of control, *i.e.* the equations of "motion", have changed, in their parameters.

Both measures are interesting, because studying dynamics of change may allow for prediction of future changes, while changes in dynamics indicate a major change in the relative contribution of each variable in the equations of motion.

We will use the Lagrangian formalism to explore dynamics and their links with extremal length. Note that since the extended Lagrangian allows for the existence of conservation laws in non-conservative systems, we will not distinguish between conservative and non-conservative dynamical systems.

Namely, we wish to show that the successive configurations $S_t = z500(x, y)$, with x, y, t the longitude, latitude and time, respectively, are coordinates of the phase space of the atmospheric circulation dynamics. The following reflection aims at showing that when the extremal length of a surface $S_t \rightarrow S_{t+1}$ doesn't change, the action is conserved, the total energy spent in the transformation is conserved as well and the equations of motion behind the change $S_t \rightarrow S_{t+1}$ are conservation laws. In short, when the extremal length doesn't change, the dynamics are the same.

The following reflection is based on [3], [13], [18]–[20],[21], [22].

2.2.2. Conformal invariants, dynamics of change and change of dynamics.

Let $u\colon(\Omega,\mathrm{g})\to(\Omega',h)$ be a smooth map from $\Omega\in\mathbb{R}^2$ to the space of $\Omega'\in\mathbb{R}^2$. The energy associated with the transformation, is called the Dirichlet energy and is defined as:

$$E(u)=\int_\Omega e(u)\,dxdy=\int_\Omega\left||\nabla u|\right|^2dxdy=\int_\Omega\frac{1}{2}|du|^2dxdy=\int_\Omega\left|\frac{\partial u}{\partial x}\right|^2+\left|\frac{\partial u}{\partial y}\right|^2dxdy \quad (2.1)$$

The Dirichlet energy $E(u)$ is the integral of the energy density $e(u)$ over the domain Ω. The Dirichlet energy can be thought as the potential elastic energy built when someone takes a rubber band, and stretches it over a rigid material, over some length. When the rubber is allowed to go back to its, possibly new, resting length, the potential energy will be converted into kinetic energy. The potential elastic energy is proportional to the Dirichlet energy.

The energy formulation of the transformation u can be related to the local metric $g(x)$ for each point $x\in\Omega$ by introducing the stress-energy tensor S.

$$S_{\alpha\beta}=\frac{1}{2}|du|^2g_{\alpha\beta}-\langle\frac{\partial u}{\partial x^\alpha},\frac{\partial u}{\partial x^\beta}\rangle=\frac{1}{2}g^{ij}\,\langle\frac{\partial u}{\partial x^i},\frac{\partial u}{\partial x^j}\rangle\,g_{\alpha\beta}-\langle\frac{\partial u}{\partial x^\alpha},\frac{\partial u}{\partial x^\beta}\rangle=e(u)g-u^*h_{ij} \quad (2.2)$$

With $S_{\alpha\beta}$, g^{ij} and $g_{\alpha\beta}$ the coefficients of the stress-energy and metric tensors respectively. The lower and upper indices are the covariant (lower) and contra-variant (upper) coordinates. $\langle\,,\rangle$ denotes the inner product, u^*h is the pull-back (inverse image) of the coefficients of the metric h by u.

(2.2) shows that the energy density $e(u)$ depends on the metric coefficients g^{ij} and that the stress energy tensor S depends on the energy density.

For any transformation u, we can define the action functional

$$A=\int_\Omega L\big(x,u(x),du(x)\big)dxdy \quad (2.3)$$

With, the Lagrangian L, defined as:

$$L\big(x, u(x), du(x)\big) = \frac{1}{2} g^{ij} \langle \frac{\partial u}{\partial x^i}, \frac{\partial u}{\partial x^j} \rangle = e(u)(x) = S_{\alpha\beta} + u^* h_{ij} \text{ (2.4)}$$

Hence,

$$A = E(u) \text{ (2.5)}$$

We now have the well-known result that, if u is harmonic and X is a vector field acting on Ω for every $t = 1 \ldots T$ then

$$E(tuX) = E(u) \text{ (2.6)}$$

Which results in

$$\delta E = \delta A = 0 \text{ (2.7)}$$

And we also have

$$\nabla S_{\alpha\beta} = 0 \text{ (2.8)}$$

Proposition 1: From (2.3-8), we get that both the Dirichlet Energy $E(u)$, and the action A are invariant under harmonic transformations, and the stress-energy tensor S is divergence free, *i.e.* it is covariant with the metric g.

Since for $m = 2$, all harmonic functions are conformal, then we get that any conformal transformation leaves the action invariant, and thus, preserves the equations of motion (in the harmonic case, the Euler-Lagrange equations).

We want to stress that, for $m = 2$, all local transformations can be harmonic and thus conformal. However, globally, the transformation of a domain Ω into another Ω' is not always conformal. This allows tracking changes of dynamics.

2.2.3. Extremal length and dynamics

Proposition 2: We have the remarkable result from Ahlfors that the extremal length is simply the reciprocal of the Dirichlet energy. The present results naturally follow:

- If the Dirichlet energy is the potential elastic energy, then the extremal length is the difference between the initial resting length, and the unloaded resting length of the rubber band due to heat loss.

- If the total energy of the system on the path ab (*i.e.* the action A) is proportional to the Dirichlet energy, it is inversely proportional to extremal length.

- For the dynamics to hold, both Dirichlet energy and Extremal length time derivatives should vanish.

3. Dependence of conformal transformations on extremal length

In this section, we aim at characterizing what are the geometrical characteristics of a conformal transformation constrained by a given extremal length. We want to investigate if the extremal length of a class of surfaces induces a specific topology or geometrical shape, and if it has specific dynamical properties. We first study how the integral lines of a conformal transformation are constrained by the extremal length, *i.e.* if any class of shapes is associated with a given extremal length. Then, we study the meaning of extremal length from a dynamical point of view, which will eventually help us giving physical dimensions to the concept.

3.1. Mobius transformations

Any tangent space of Riemann surface TS_x (all hypersurfaces in $\mathbb{R}^3$ are Riemannian) is equipped with the Euclidean metric $\boldsymbol{g}$. A metric generalizes the inner product on a vector space and allows for computation of distance and angles. The conformal structure of the surface is expressed in local coordinates as $\boldsymbol{g} = e^2(dx^2 + dy^2)$. Those coordinates can be parameterized to give the, so called, isothermal complex coordinates $z = x + iy$. The conformal group G is the group of angle preserving transformations. The group must satisfy the so-called group axioms: closure, associativity, identity and invertibility. Closure requires that the product of two members of the group must also be a member of the group, *i.e.* for

$a, b \in G$, $a \cdot b \in G$. Associativity refers to the classical term *i.e.* for $a, b, c \in G$, $a \cdot (b \cdot c) = (a \cdot b) \cdot c$. Identity is the requirement that there exists one member$e \in G$ that maps a member of the group to itself, *i.e.* $a \cdot e = a \cdot e = a$. Finally, invertibility is the requirement that there exists a member $a^{-1} \in G$ such that $a \cdot a^{-1} = e$. In other words, if $a(e)$ maps e to $e + de$, then $a^{-1}(e + de)$ maps it back to e. An important note is that $a \cdot a^{-1} = a^{-1} \cdot a$ does not always holds, which means the order of the transformations matters.

When a group satisfies the group axioms, it is said to be defined. In two dimensions, as in our context, the conformal group (and its associated Lie algebra) is infinite dimensional (i.e. any arbitrary holomorphic function on S is a conformal transformation and thus every surface is locally conformally equivalent to another). However, there is no guarantee that a collection of locally conformal transformations yields a global conformal one. Additionally, depending on its generating set, the infinite-dimensional group may not be defined at every point of a surface. In our study, the generating set of the conformal transformations is $\mathbb{R}^2$, which makes only translations, rotations, dilations and inversions defined globally. This subgroup of conformal transformations is finite-dimensional, and thus restricts the number of surfaces that can be conformally equivalent.

In two dimensions, at a point $x \in S$, with the tangent space TS_x parameterized with isothermal coordinates, a conformal transformation of the neighbourhood of x is a coordinate transformation f defined as:

$$f(z) = \frac{az+b}{cz+d} \quad (3.1)$$

With a, b, c, d complex numbers that satisfy $ad - bc = 1$.

The subgroup of such conformal transformations is called the extended Mobius group $\boldsymbol{Aut\ \widehat{C}}$. We thus have the following transformations (3.2)

Translation : $f(z) = z + b; a = 0, c = 0, d = 0$

Rotation : $f(z) = az; |a| = 1, b = 0, c = 0, d = 1$

Dilation: $f(z) = az; a \in \mathbb{R}, b = 0, c = 0, d = 1$

Inversion : $f(z) = \frac{1}{z}; a = 0, b = 1, c = 1, d = 0$

Mobius transformations in (3.2) can be classified in four groups depending on their multiplier μ.

Let $f(z)$ in (2.9) be expressed in matrix form:

$$M_f = \frac{1}{\sqrt{ad-bc}}\begin{pmatrix} a & b \\ c & d \end{pmatrix} \text{ (2.11)}$$

[23]: A Mobius transformation f has one and only one conjugate matrix g if there exists a continuous bijection h such that $g = h^{-1}fh$, $i.e.$ if the diagram of those three functions commutes.

Then, g is equal to:

$$\mu z; (\mu \neq \{0,1\}) \text{ or } z + 1; (\mu = 1) \text{ (3.3)}$$

Where μ is called the multiplier of the Mobius transformation. The first case when $\mu \neq \{0,1\}$ is when there are two fixed points, *i.e.* for rotations and dilations. The case with $\mu = 1$ is for translations, with only one fixed point.

Multipliers are defined at the fixed points of the Mobius transformation and can be computed as follows:

$$\mu_i = \begin{cases} f'(z_i); (z_i \neq \infty) \\ \lim_{z_i \to \infty} \left(\frac{1}{f'(z_i)}\right); (z_i = \infty) \end{cases} \quad i = 1,2 \text{ (3.4)}$$

Computing the singular value decomposition of M_g, we find the eigenvalues of M_f to be $\sqrt{\mu}$ and $-\sqrt{\mu}$

For a Mobius transformation M_f in Ω, the multipliers μ will generate level lines, *i.e.* lines where $f = const$, *i.e.* the coefficients of the Mobius transformation are constant (see Figure S1.3). The four groups of Mobius transformations are defined by the type of level lines, depending on the multiplier value.

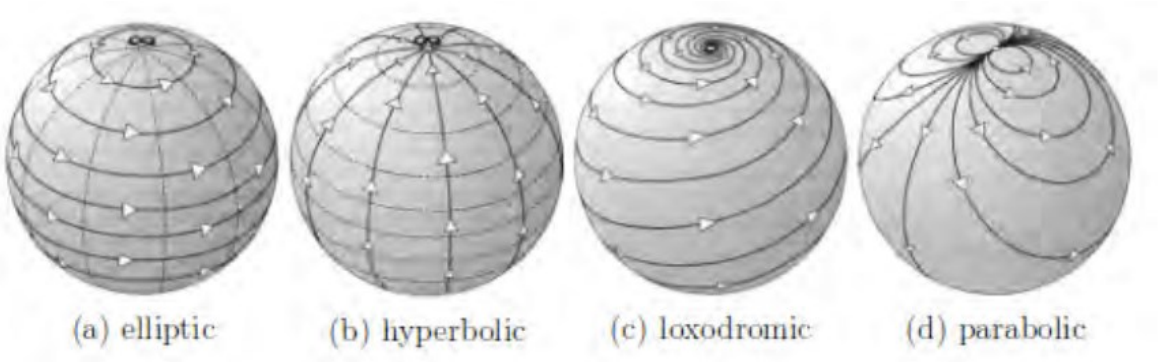

Figure S1.3: *The four canonical Mobius Transformations and their associated level lines on the extended complex plane.*

- If the multiplier μ is complex but of absolute value 1, then the transformation is elliptic, and points move along a rotation. (Figure S1.3a)
- If the multiplier μ is real, then the transformation is hyperbolic: points are moved radially (*i.e.* it a dilation), repelled from 0 and attracted by ∞ if $\mu > 1$, or reversely if $\mu < 1$. (Figure S1.3b)
- If the multiplier μ is a general complex number (without restriction on its absolute value), then the transformation is loxodromic: points move in a combination of rotation and dilations. (Figure S1.3c)
- If the $\mu = 1$ but the M_g is not diagonal, that is, of the form $\begin{pmatrix} 1 & a \\ 0 & 1 \end{pmatrix}$, then the transformation is parabolic and corresponds to a translation of the form $z = z + a$. (Figure S1.3d).

3.2. Integral lines of a Mobius transformation constrained by extremal length

Let's define Ω be a section of the tangent bundle TS and f is a set of Mobius transformations on Ω . The metric $\bar{g}$ over a tangent bundle TS is said to be natural if it can be represented as projection over some basis vector fields (*c.f.* horizontal and vertical lifts of the vector fields of TS) of the Euclidean metric of the surface S. That is to say that at a point $x \in S$, the metric of S has a smooth correspondence with that of TS at the same point. Unfortunately, for hypersurfaces, this often not the case [24]. For conformal transformations however, it has been shown that conformal metrics of the tangent bundle TS are smoothly related to that of the surface S by homeomorphisms [25].

We will thus identify Ω, a section of the tangent bundle TS, with the complex plane $\mathbb{C}$.

Note that since we are dealing with conformal transformations, the domain Ω is defined up to conformal morphisms.

The Dirichlet energy of a transformation from the open set $\Omega \in \mathbb{C}$ to $\mathbb{R}^2$, $f: \Omega \to \mathbb{R}$, is defined as follows:

$$E(f) = \frac{1}{2}\int_{\Omega} \|\nabla f\|^2 dxdy = \int_{\Omega} e(f)dxdy \quad (3.5)$$

$e(f) = \frac{1}{2}\|\nabla f\|^2$ is the energy density, ∇ is the covariant derivate on Ω.

The Dirichlet energy measures how smooth the function f is over the set Ω.

We aim at characterizing the type of Mobius transformations that are allowed in a domain Ω of a given extremal length.

The domain Ω being a section of the tangent bundle TS, there is a vector associated with each point in Ω and thus, Ω is a vector field.

The domain $\in \mathbb{C}$ is bounded and a vector field is defined on both the interior Ω and its boundary $\partial\Omega$. The vector field gives rise to line integrals, that is, imaginary paths a particle submitted to the action of each vector would follow from a starting point A to its ending point

B. Because they are harmonic (*i.e.* they satisfy Laplace's equation), knowing how they behave on the boundary Ω is sufficient to know how they behave inside Ω [13].

In particular, let's define a harmonic measure $u(z)$ on $\Omega \cup \partial\Omega$ as the length (normalized to be a probability) of line integrals, resulting from Mobius transformations on Ω, starting from edge L and ending to edge R. The function u satisfies the following properties:

- It is harmonic and bounded
- $u(L) = 0; u(R) = 1$
- The derivative $\frac{\partial u}{\partial n}$ on $\partial\Omega$ vanishes.

Definition 2.1 [13]**:** The Dirichlet energy of u is the reciprocal of the extremal distance between L and R:

$$\text{E(u)}=\lambda(L,R)^{-1} \quad (3.6)$$

Let level lines μ_i be lines of $u = cst$, each level line starts somewhere on the boundary $\partial\Omega$ and ends at another point on this same boundary. Now, by the reflection argument, u has an harmonic conjugate v, and the level lines η_i of v cross those of u at right angle. Figure S1.4 shows an example of level lines for both u and v .

Definition 2.2 [13]: An increase $\eta_i \rightarrow \eta_{i+1}$ on a portion of the boundary $\partial\Omega$ is equivalent to the gradient of u along the outer normal vector $\boldsymbol{n}$. If that portion is noted E_1, then :

$$dv = \int_{E_1} \frac{\partial u}{\partial n} |dz| \qquad (3.7)$$

And by Green's theorem, *i.e.* $\int_{\partial\Omega} \frac{\partial u}{\partial n} = 0$, we get :

$$\int_{\partial\Omega} u dv|dz| = E(u) = \int_{\Omega} (u_x^2 + u_y^2)\, dxdy \quad (3.8)$$

With u_x^2, u_y^2 being the square of the derivatives of u in the x and y directions respectively.

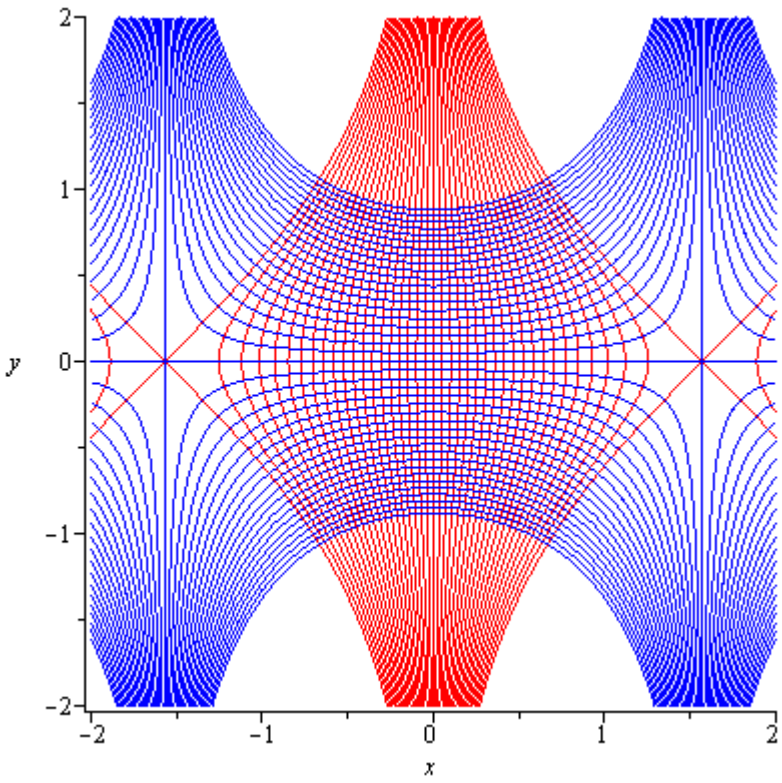

Figure S1.4: *Example of level lines of a harmonic function u (blue) and level lines from its conjugate v (red). The two sets of lines intersect at right angles.*

Equation (3.8) means that the Dirichlet energy of a transformation u in the interior Ω is equal to the sum of those transformations on the boundary. The latter measures how much $u$is "outflowing" of $\partial\Omega$. Because the boundary is counted counter-clockwise, the outflowing is through$R$. The more the line integrals are flowing through R, the higher the "outflow".

Note that in the following, when talking about "high" and "low" extremal length, we mean "higher" and "lower", that is, a map which increases or decreases the extremal length.

Proposition 3 Following (3.6) and (3.8), we see that line integrals producing a net outward flux will be associated with high Dirichlet energy and, consequently, low extremal length. Due to Green's theorem, this means that in Ω (*i.e.* the interior of the domain), the line

integrals will have tendency to be parallel and oriented towards R. The converse is true for high extremal length: the line integrals will diverge, so that if one project them onto horizontal lines, only few line integrals will reach R. In our context, we are dealing with hypersurfaces, *i.e.* surface embedded in $\mathbb{R}^3$, so any lift of some point and its neighbourhood will increase the divergence and thus induce and increase in extremal length. We can here make reference of [3] electrical analogy. The author noted that if Ω is an electrical network under a potential difference at L and R, where u is the electrical current flowing from L to R , low extremal length was associated with numerous and shorter wires, and conversely for high extremal length. This makes our divergence criteria compatible with results from [3].

In the next section, we follow the ideas of Thurston (2019).

2.3.3 The dynamical concept of extremal length

The previous section highlighted that a class of deformations is associated with each value of extremal length. We now want to explore if there is some intrinsic characteristic of the medium were the transformation occurs associated with extremal length. One way to investigate this question is the use of elastic graphs [20].

Definition 2.3 Let's define a *marked graph* as a pair $(\Gamma, M)$with Γ a graph, and $M \in \Gamma$ a set of market points. If $f: (\Gamma_1, M_1) \mapsto \Gamma_2, M_2)$, any marked point maps to a marked point (*i.e.* $f(M_1) \in M_2$).

A $length\ graph$ K(Γ, ℓ) is a graph Γ where each edge e has a fixed, positive length ℓ.

An *elastic graph* $G(\Gamma, \alpha)$is a graph Γ where each edge e is given an elastic measure α akin to the inverse of the spring constant k in Hooke's Law.

The marked graph can be thought as the triangulation of our surface S.Each of the vertices represents our data points, and edges represent the shortest path between them. The market points of our graph lie on the boundary of S. Since the base of our surface S is a rectangle, the

typical market points would be its four corners. The length graph K will thus represent the lengths between each vertex. The elastic graph G will represent the potential elastic energy of a vertex v_i if it was stretched to the vertex v_{i+1} along the edge e with elastic weight α_e. The elastic weight, α_e, is analogue to the spring constant in Hooke's energy law. One way to think about the length graph is a network of pipes (pipes being the edges), and the elastic graph as a rubber band network (the rubber band being the edges).

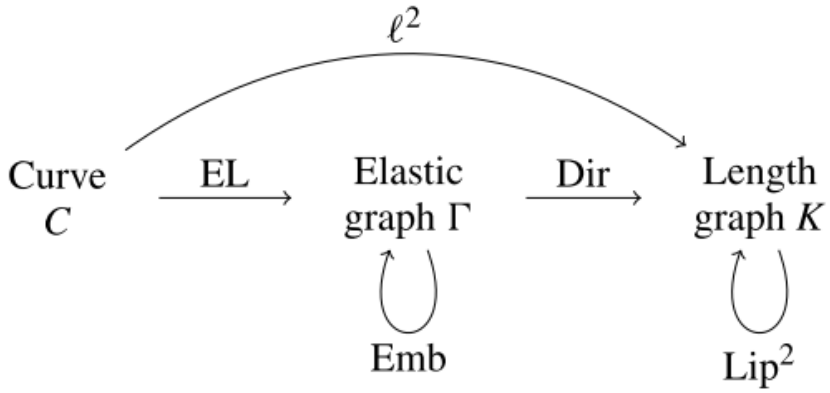

Figure S1.5: *The diagram of the association of a norm to a curve* $\boldsymbol{C}$*: We want to give a curve in the complex plane a norm. The curve* $\boldsymbol{C}$ *is first mapped to an elastic graph* $\boldsymbol{G(\Gamma, \alpha)}$*, then mapped to a length graph* $\boldsymbol{K(\Gamma, \ell)}$*. The notations above the arrows are the different energies associated with each map:* $\boldsymbol{EL}$ *is the extremal length;* $\boldsymbol{Emb}$*, the embedding energy;* $\boldsymbol{Dir}$*, the Dirichlet energy;* $\boldsymbol{Lip^2}$ *the Lipschitz energy;* $\boldsymbol{\ell^2}$ *is the squared norm. Straight arrows as well as the large curved arrow, denote maps from one space to another. Loops denote maps from one space to itself (e.g. a map from an elastic graph to another).* [26]

We are interested in the energies involved when the rubber band are stretched to the pipes, that is, when $G \mapsto K$ and how those energies evolve when going from one rubber band network G_1 to another G_2.

The diagram in Figure S1.5 sums the process of taking a curve C in the complex plane, mapping if to an elastic graph $G(\Gamma, \alpha)$, then mapping the elastic graph to the length graph $K(\Gamma, \ell)$.

The elastic graph G is considered a spine for S with the marked points a_1, a_2, a_3, a_4 (the four corners of our surface boundary) if any deformation of S with respect to its marked points, snaps back to G under the inverse of the map that deforms S. Since extremal length is the energy of the map from the curve C to the elastic graph G it is evident that extremal length will determine the elasticity of the curve C. Basically, the first part of the diagram in Figure S1.5, is a projection of the curve C onto the elastic graph G.

On G, the extremal length is determined as

$$EL_{\alpha}[G] = \sum_{e_{i..n}} n_c(e)\alpha(e) \quad (3.9)$$

Where $n_c(e)$ is the number of times the curve C crosses the edge e, and α is the spring constant of the edge e.

Proposition 4 It follows immediately from (3.9) than a high extremal length is associated with either a large number of crossing of the edge e or high α for that edge.

Let $\phi: G_1 \mapsto G_2$, $f: G_1 \mapsto K_1$, $f': G_2 \mapsto K_2$, and $C \in G_1$ we have:

$$SF[\phi] = \sup \frac{EL[\phi C]}{EL[C]} = \sup \frac{Dir[\phi o f']}{Dir[f]} \quad (3.10)$$

With SF being the stretch factor of ϕ, $Dir[..]$ the minimizer of the Dirichlet energy for the map.

If $SF[\phi] < 1$, we have G_1 looser (*i.e.* with less potential elastic energy) than G_2. We also have the relationship between extremal length and the minimizer of Dirichlet energy:

$$\ell[f, C]^2 \leq Dir[f]EL[G] \quad (3.11)$$

Using (3.9-11), we can say that extremal length is the analogue of the potential energy lost during the stretch of the rubber band, due to heat build-up and loss, and that loss is directly proportional to extremal length, which is akin to a resistance.

2.3.4 Extremal length in point mechanics

Friedman and Scarr (2019) have shown that the action A as defined in our context is equivalent to Newton's second law. Using the analogy between extremal length and electrical resistance in an electrical network [3], we can give physical units to extremal length.

Definition 2.4 [3]: The linear form of Ohm's law,between two nodes a, b is defined as:

$$\lambda = \rho = \sum_1^n r_j w_j{}^2 = EI \text{ (3.12)}$$

With ρ the electrical resistance, r_j the specific resistivity on the sub-arc j and w_j the current density vector on that same sub-arc. E is the electromotive force resulting from the potential U between nodes a, b and I the strength of the flow W.

Definition 2.5 [28]: Consider the electrical charge as a wave amplitude, then, Coulomb units are analogue to distance. Then, due to wave interference property, those units can be added and subtracted. It follows that Ohm's Law can be expressed with the following U', R', I' (respectively potential, resistance and current), whose dimensions are :

$$U' = \frac{kgm}{s^2} = Newtons$$

$$R' = \frac{kg}{s} = Mass\ moved\ in\ a\ given\ time$$

$$I = \frac{m}{s} = Velocity$$

It follows

$$ma = -\nabla \mathrm{U} = m\frac{d^2x}{dt^2} = -\nabla U' = R'I'. \text{ (3.13)}$$

Proposition 5: From (3.13), the extremal length between two sides of a topological quadrilateral has units of $[momentum].[time]^{-1}$ or $[energy].[length]^{-1}$. It can be understood as total energy spent in moving the particle along its trajectory or the total momentum needed to cover a certain length in a given time.

4. Extremal length and conserved quantities

We have shown in previous sections that the invariance of extremal length meant conserved dynamics. Thus, this implies the existence of conservation laws, that is, conserved quantities.

Both in the case of conservative and non-conservative systems of N particles, conserved dynamics admit N independent quadratic conservation laws. In the conservative case, the conservation of mechanical energy is the linear combination of all independent conservation laws. In the case of non-conservative, conservation laws equate to a constant, thus the linear combination of them represents the total mechanical energy, up to a constant.

Following Proposition 5, it is easy to see that changes in extremal length will represent non-conservative shifts in the conservation laws, with loss of total momentum to the profit of thermal energy for increasing extremal length, and the opposite for decreasing extremal length.

References

[1] E. Noether, "Invariant Variation Problems," *Transp. Theory Stat. Phys.*, vol. 1, no. 3, pp. 186–207, 1971.

[2] L. Ahlfors and A. Beurling, "Conformal invariants and function-theoretic null-sets," *Acta Math.*, vol. 83, no. 1, pp. 101–129, 1950.

[3] R. J. Duffin, "The Extremal Length of a Network," *J. Math. Anal. Appl.*, vol. 215, pp. 200–215, 1962.

[4] D. Chelkak, “Robust discrete complex analysis: A toolbox,” *Ann. Probab.*, vol. 44, no. 1, pp. 628–683, 2016.

[5] I. Giordanelli, N. Posé, M. Mendoza, and H. J. Herrmann, “Conformal Invariance of Graphene Sheets,” *Sci. Rep.*, vol. 6, no. February, pp. 1–7, 2016.

[6] B. F. Schutz, *Geometrical Methods of Mathematical Physics*. Cambridge: Cambridge university press, 1980.

[7] M. R. Turner, T. J. Bridges, and H. Alemi Ardakani, “The pendulum-slosh problem: Simulation using a time-dependent conformal mapping,” *J. Fluids Struct.*, vol. 59, pp. 202–223, 2015.

[8] E. Saucan, E. Appleboim, E. Barak-Shimron, R. Lev, and Y. Y. Zeevi, “Local versus global in quasi-conformal mapping for medical imaging,” *J. Math. Imaging Vis.*, vol. 32, no. 3, pp. 293–311, 2008.

[9] C. Kambhamettu and D. B. Goldgof, “Curvature-based approach to point correspondence recovery in conformal nonrigid motion,” *Computer Vision and Image Understanding*, vol. 60, no. 1. pp. 26–43, 1994.

[10] D. Chelkak and S. Smirnov, “Universality in the 2D Ising model and conformal invariance of fermionic observables,” *Inven. math*, vol. 189, pp. 515–580, 2012.

[11] S. Benoist and C. Hongler, “The scaling limit of critical Ising interfaces is CLE(3),” *Arxiv*, pp. 1–27, 2016.

[12] D. Chelkak and C. Hongler, “Crossing probabilities in topological rectangles for the critical planar FK-Ising model,” pp. 1–30, 2012.

[13] Lars V. ahlfors, *Conformal invariants*. McGraw-Hill, 1973.

[14] F. Klein, “Neue Beiträge zur Riemann’schen Functionentheorie,” *Math. Ann.*, vol. 21, no. 2, pp. 141–218, 1883.

[15] H. Poincaré, “Sur l’uniformisation des fonctions analytiques,” *Acta Math.*, vol. 31, no. 1, pp. 1–63, 1908.

[16] J. W. Cannon, W. J. Floyd, and W. R. Parry, “Conformal modulus: the graph paper invariant or The conformal shape of an algorithm,” pp. 1–6, 1996.

[17] S. M. Boker, A. D. Staples, and Y. Hu, “Dynamics of Change and Change in Dynamics,” *Physiol. Behav.*, vol. 176, no. 1, pp. 139–148, 2017.

[18] F. Helein, *Harmonic Maps, Conservation Laws and Moving Frames*. Cambridge university press, 2002.

[19] W. Thurston, “The finite Riemann mapping theorem, Invited talk at the International Symposium at Purdue University on the occasion of the proof of the Bieberbach conjecture.,” 1985.

[20] D. P. Thurston, “Elastic graphs,” *Arxiv*, 2019.

[21] B. Vujanovic, “A study of conservation laws of dynamical systems by means of the differential variational principles of Jourdain and Gauss,” *Acta Mech.*, vol. 65, no. 1–4, pp. 63–80, 1987.

[22] P. Mann, *Lagrangian and Hamiltonian Dynamics*. Oxford University Press, 2018.

[23] T. Rybalkina and V. V. Sergeichuk, “Topological classification of Mobius transformations,” *Arxiv*, no. 3, pp. 1–11, 2013.

[24] S. Deshmukh and S. B. Al-Shaikh, “Tangent bundle of a hypersurface of a Euclidean space,” *Beitrage zur Algebr. und Geom.*, vol. 52, no. 1, pp. 29–44, 2011.

[25] E. Peyghan and A. Heydari, “Conformal vector fields on tangent bundle of a Riemannian manifold,” *J. Math. Anal. Appl.*, vol. 347, no. 1, pp. 136–142, 2008.

[26] D. P. Thurston, *From rubber bands to rational maps: a research report*, vol. 3, no. 1. Springer International Publishing, 2016.

[27] Y. Friedman and T. Scarr, “Geometrization of Newtonian Dynamics,” *J. Phys. Conf. Ser.*, vol. 1239, p. 012011, 2019.

[28] J. Yee, “The Relation of Ohm ’ s Law to Newton ’ s 2 nd Law,” pp. 1–6, 2019.

S2: Extremal length and geopotential height

We now make the connection with dynamics, *i.e.* the equations of motion. There are two kind of equations of motion that are of interest to us. First, we have the dynamics of the geopotential themselves, that is how they evolve in time. But we are also interested is linking extremal length to the geostrophic winds. Hopefully, because of the geostrophic approximation, *i.e.* the forces derive from potential energy, applying Newton's second law of motion should be possible (we will nevertheless show that it is compatible with extremal length).

1. Extremal length in the quasi-geostrophic tendency equation

The geopotential tendency equation, gives the evolution of geopotential height under the shallow layer and quasi-geostrophic approximations.

The geopotential tendency equation can be stated in its simplified form as:

$$\chi \propto G_v + Tp_v + K + Q \quad (1.1)$$

With χ the geopotential height, G_v the geostrophic vorticity advection, Tp_v the potential temperature advection, K the friction resulting from advection of air parcels, and Q diabatic warming of the air parcel at the given pressure level resulting in different thicknesses of the air parcel at a given pressure level.

Since we are assuming the geostrophic condition, $K = 0$. At mid altitude (i.e. around 500hPa), Tp_v is small and hence will be neglected thus becomes:

$$\chi \propto G_v + Q \quad (1.2)$$

The geostrophic vorticity advection term is responsible for the horizontal transport of absolute vorticity, while the diabatic heating is responsible for the amplification high/low pressure systems.

Since vorticity advection G_v is a kinetic term, and diabatic heating Q a source of potential energy, we can write eq. 14 in the Hamiltonian formalism:

$$\frac{d\chi}{dt} = \frac{\partial \chi}{\partial x}\frac{\partial H}{\partial p} - \frac{\partial \chi}{\partial p}\frac{\partial H}{\partial x} \quad (1.3)$$

with

$$H = \frac{((\nabla \times p).v)^2}{2m} + V(x) \quad (1.4)$$

the Hamiltonian, $G_v = (\nabla \times p).v$, p the linear momentum of the air parcel, and $V(x)$, the potential energy of the air parcel at x due to diabatic heating Q.

Proposition 6 Following Propositions 2-4 and (1.3-1.4), extremal length has an inverse relation with momentum p, thus, high extremal length geopotential height are characterized by slow (or even stalled) horizontal advection of vorticity, and high curl.

2. Extremal length and the geostrophic winds.

The correspondence between extremal length, outflow, vorticity, momentum, and resistance makes prediction of geostrophic winds in the North Atlantic area intuitive. High extremal length geopotential height will lead to deformed westerlies, with geopotential height gradients. On the other hand, low extremal length geopotential with be represented by zonal winds, with centres of pressure parallel to each other.

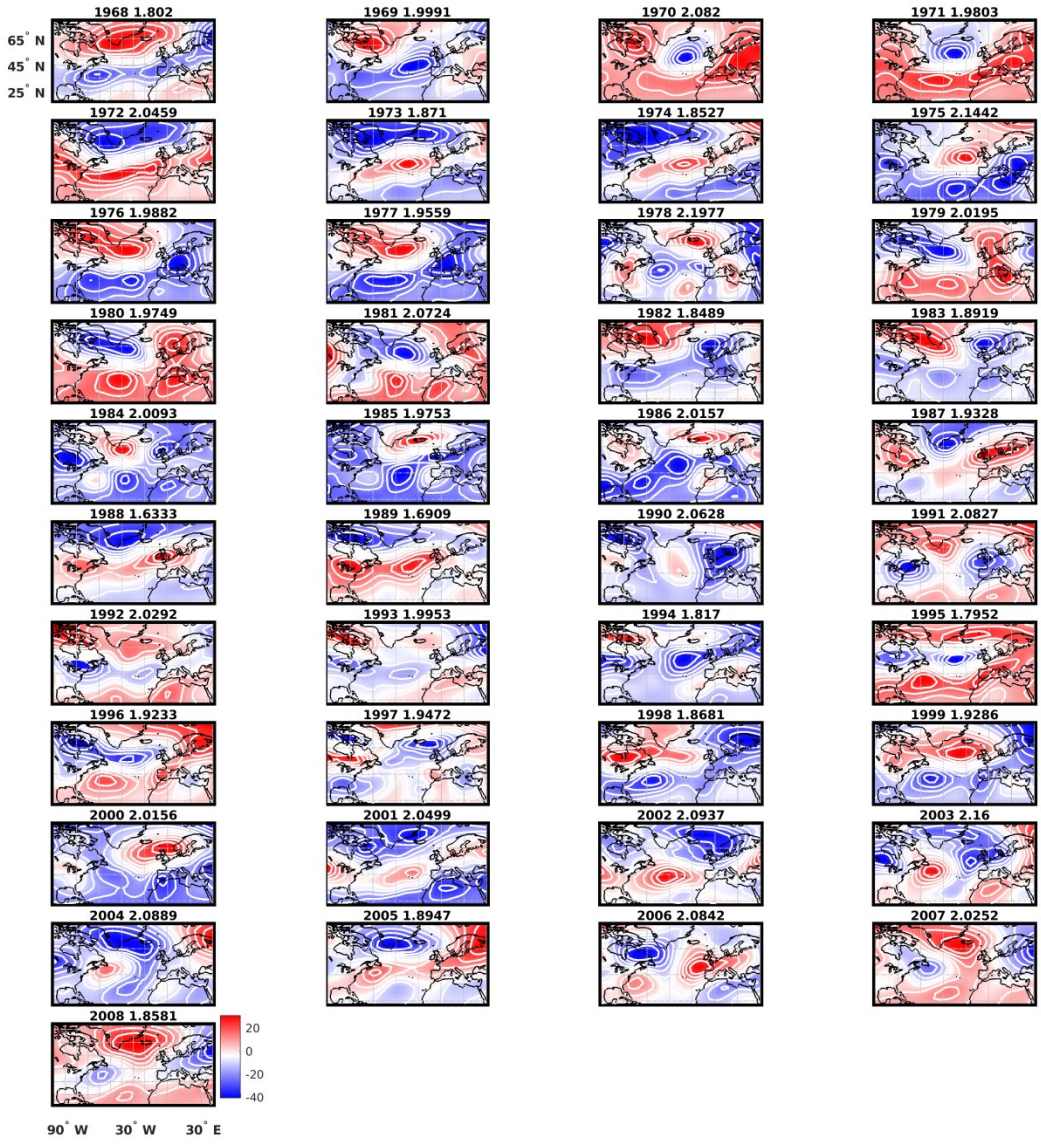

Figure S2.1. z500 snapshots and their corresponding climatological extremal length.

3. Experiments

We ran two experiments in order to compare the predictions of our theoretical reflexions on extremal length, to actual cases. First, we computed the extremal length for the yearly 500hPa geopotential height from 1968 to 2008 and discuss how each computed extremal length matches the shape of the z500. Next, we computed the extremal length of meridional wind and 300hPa geopotential height for four heat waves events, June 1997, August 2003, July 2010 and July 2011. We discuss the links between extremal length and the theory of Quasi-

resonant amplification, which has been thought as being one major driver of those heat waves [1], [2].

3.1. Extremal length of 500hPa geopotential height

Figure S2.1 shows the time series of 500hPa geopotential height over the North Atlantic area. According to the predictions, the range of extremal length will be differentiated by how the surface is deformed relative to the four corners of the boundary. For instance, low extremal length geopotential height should feature deviations from flatness with Eigen vectors aligned on the West-East direction, *i.e.* centres of pressure should have a West-East extension, be parallel to each other, placed in a mirror position with respect to each other, and have the largest West-East extension. On the other hand, high extremal length z500 should have several poles not parallel to each other; each having different direction of extension, with small West-East extension, and the geostrophic winds should describe a wave-like trajectory.

The examination of the time series in Figure 1 shows that our predictions are well matched with observations. For instance, the largest extremal lengths are associated blocking patterns, while low extremal lengths are associated with mostly zonal patterns (*e.g.* 2003 versus 1988 for high and low extremal lengths). The West-East extension is well matched with extremal length, lower extremal length z500 have centres of pressure that are spread from West-East, while higher extremal length z500 have their centres of pressure with low West-East extension (*e.g.*1968 versus 1969). The parallelism and symmetry of the different centres of pressure is also are good criteria when the sinuosity of the patterns fails to discriminate between surfaces. For instance, 1998 and 1999 years are very similar, however, 1999 has centres of pressure that are less parallel and not placed in face of each other, but more like a succession from West to East. As a consequence 1999 has higher extremal length than 1998. Those features match with Propositions 2-3, which predict that surfaces of high extremal length have been deformed by forces whose integral lines' net outflux is small and conversely

for low extremal length surfaces. Proposition 4 hints that z500 with high extremal length have been associated with "thermal" losses during the bending of the iso-height, that is, when relaxed, they may not come back to their original state, unless a new, opposite, force acts onto them.

3.2.Quasi-resonant amplification and extremal length

We wanted to confront our theoretical results to an emergent field of research in climate science, that is, quasi-resonant amplification of Rossby waves (QRA, [29]). This phenomenon is a particular state of the atmosphere at mid-latitudes, and has been presented as one of the main driver of large heat waves during the last decades, possibly due to anthropogenic warming [3]. The principle derives from quantum physics and can be described this way (for an illustration, we refer the reader to [30]): At mid-latitudes in the Northern Hemisphere, Rossby waves flow from West to East together with the sub-polar jet-stream. Between each ridge and trough of those waves, low and high pressure systems develop. As the Rossby waves travel, so do those systems. Additionally, the energy of those Rossby waves is progressively lost North and Southward when those interact with both polar and tropical masses so that Rossby waves and their accompanying pressure systems weaken as one progresses North/Southward. However, in summer, the jet stream usually split in those "veins". The Rossby waves get trapped between those veins that become a waveguide. In classical mechanics, this waveguide would be like two impenetrable walls, and air particles within the Rossby waves would reflect on the walls and interfere with each other. In the quantum paradigm, there is some probability that the particles leak out of the walls, even if very low, so there is no interference. Instead, if the Rossby waves stall, that is, they stop their progression towards the East, they become stationary and amplification occurs, even though the modality is still unclear ([1], [2]). This happens when the jet stream is anomalously bent, with ridges and troughs extending North/Southwardly more than usual. Severe heat waves,

over Europe and United states, have been associated with those stalled Rossby waves and their complicated mechanism [3], [4]. The trigger for the waveguide development is a reduced temperature gradient between polar and tropical air masses.

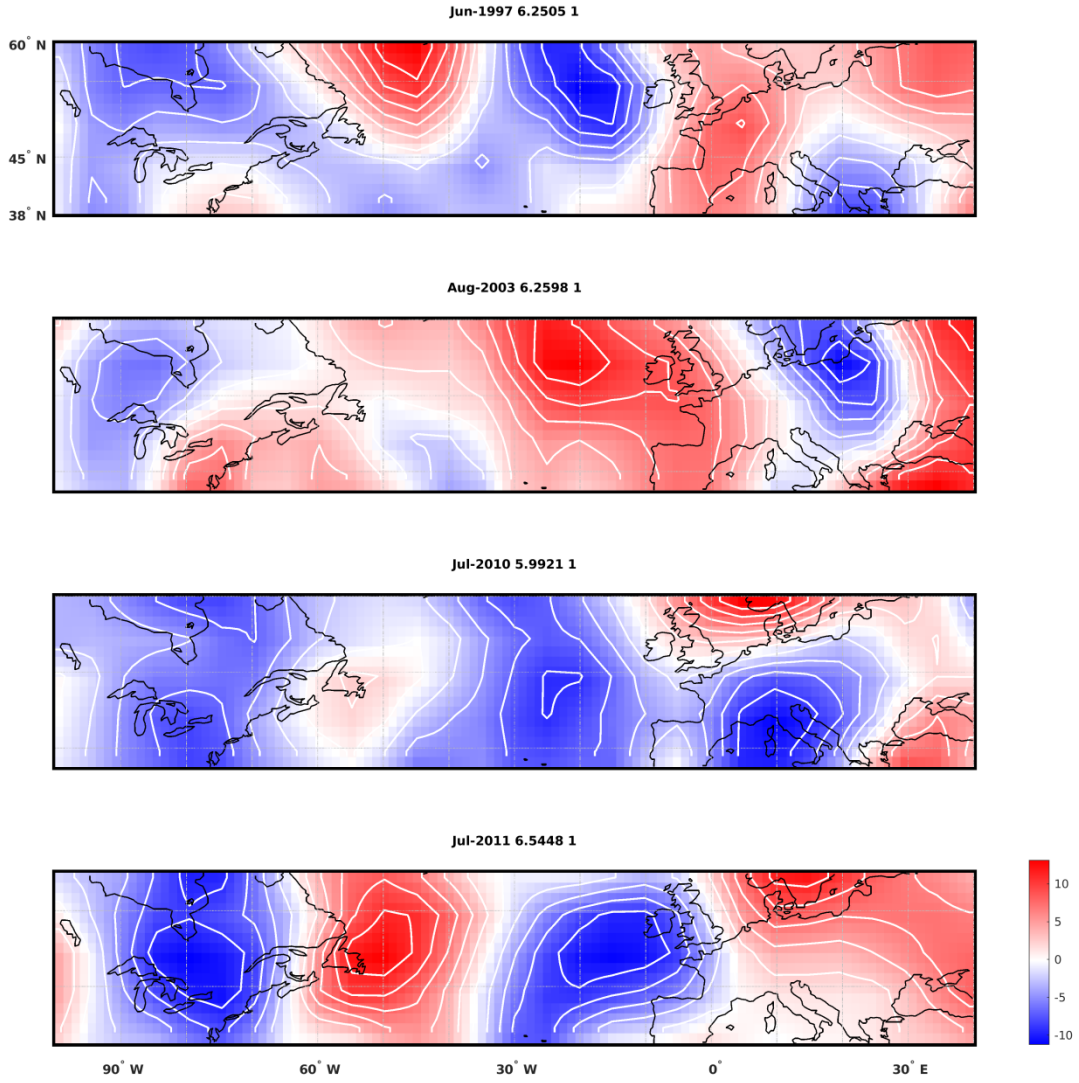

Figure S2.2. Meridional wind for each QRA events. *Blue meridional winds flow southward, red meridional winds flow northward. Next to the data is the extremal length associated with the pattern.*

Because those events represent clear shifts in dynamics, and are related to the local geometry of the atmosphere, comparison with our extremal length theoretical hypothesis can be

interesting. We thus study four heat waves events, June 1997, August 2003, July 2010 and 2011, as depicted in [29] and [30], under the umbrella of extremal length. Figure S2.2 shows the situation for each event, in terms of meridional wind.

The two most severe events were those of 2003 (Major heat wave over Europe), and 2011 (Major heat wave over the United States). Both feature the most severe extremal length of the four events. The event of July 2011 is especially representative of the high extremal length surfaces: wave like structure, with several pressure centres blocking each other. Note that the stalled state of the Rossby waves is predicted by the extremal length as it is the momentum needed to move a particle over a distance, hence, high extremal length induce more likeliness for stalled situations and thus permanent pressure systems.

Figure S2.3 shows the time series of extremal length of summer meridional winds (JJA) from 1995 to 2012.

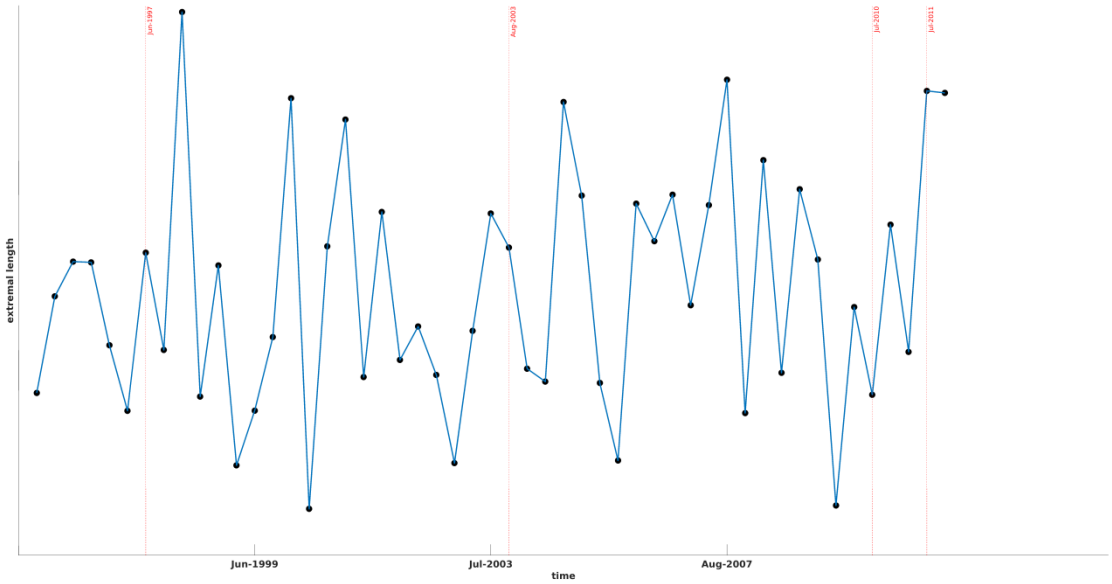

Figure S2.3. E**xtremal length time series of summer meridional winds**. *Dashed line show the location of each event.*

Apart from July 2011, not all events' months match with the highest extremal lengths. However, each events' year does, and, as a matter of fact, all high extremal length peaks match with recorded heat waves over the North Atlantic area [5].This suggests that there is a link between extremal length, QRA and the heat waves over the North Atlantic area. This relationship will be treated in future work.

References

[1] V. Petoukhov, S. Rahmstorf, S. Petri, and H. J. Schellnhuber, "Quasiresonant amplification of planetary waves and recent Northern Hemisphere weather extremes," *Proc. Natl. Acad. Sci. U. S. A.*, vol. 110, no. 14, pp. 5336–5341, 2013.

[2] M. E. Mann, "The Weather Amplifier," *Sci. Am.*, vol. 320, no. 3, pp. 42–49, 2019.

[3] M. E. Mann, S. Rahmstorf, K. Kornhuber, B. A. Steinman, S. K. Miller, and D. Coumou, "Influence of Anthropogenic Climate Change on Planetary Wave Resonance and Extreme Weather Events," *Sci. Rep.*, vol. 7, no. February, pp. 1–10, 2017.

[4] M. E. Mann *et al.*, "Projected changes in persistent extreme summer weather events: The role of quasi-resonant amplification," *Sci. Adv.*, vol. 4, no. 10, pp. 1–10, 2018.

[5] World Meteorological Organization Global, "Weather extremes archive," 2019. [Online]. Available: https://wmo.asu.edu/content/world-meteorological-organization-global-weather-climate-extremes-archivehttps://wmo.asu.edu/content/world-meteorological-organization-global-weather-climate-extremes-archive. [Accessed: 12-Sep-2019].

S3: Approximating the extremal length of a surface

The theory described above lies in the continuous setting. For a discrete setting, the extremal length has similar properties that were demonstrated by [1]. The curves in the continuum are replaced by path along edges connecting nodes.

Finding ρ that satisfies the supremum condition in (S1, 1.1) on an arbitrarily Riemannian surface is sometimes impossible for the lack of any explicit solution. However, one can exploit the conformal invariance of the extremal length. Any conformal equivalent topological space will give the same extremal length if the corners of the Riemannian surface are identified. This reduces the number of possible conformal maps from Q as only the maps $f(\lambda_Q): Q \to Q'$ are allowed. It follows from [2] that the Euclidean rectangle is one candidate for such a map. If one can map Q to Q' with the latter being a conformal rectangle then all extremal curves are straight lines going from L to R and thus the extremal length is just the width/height ratio of the rectangle. Figure S1.2 illustrates the idea.

The computation of the extremal length once mapped to a conformal rectangle is trivial. However, the conformal map preserving the conformal structure of Q is much more difficult. The reason is that it is impossible to flatten a curve in the discrete setting. Thus a conformal map will always be approximately conformal with some distortion. This distortion is usually located at some points, most notably the corners $\{q1, q2, q3, q4\}$. There is an additional source of distortion which is purely computational. Since a conformal map preserves local angles, it is needed to have a discrete measure of those angles. Delaunay triangulations [3] are commonly used for their conditions are easily satisfied for a variety of surfaces. However, when the surface lives in R^3 (i.e. has $\{x, y, z\}$ coordinates), the triangulation is based on the {x,y} base only. The vertices of the triangles are then lifted orthogonally to their respective z

coordinates. During this process, the angles of the triangulation are not preserved and thus the conformal structure degraded. Figure S3.1 shows an example with a snapshot of geopotential height represented in $\{x, y, z\}$ coordinates.

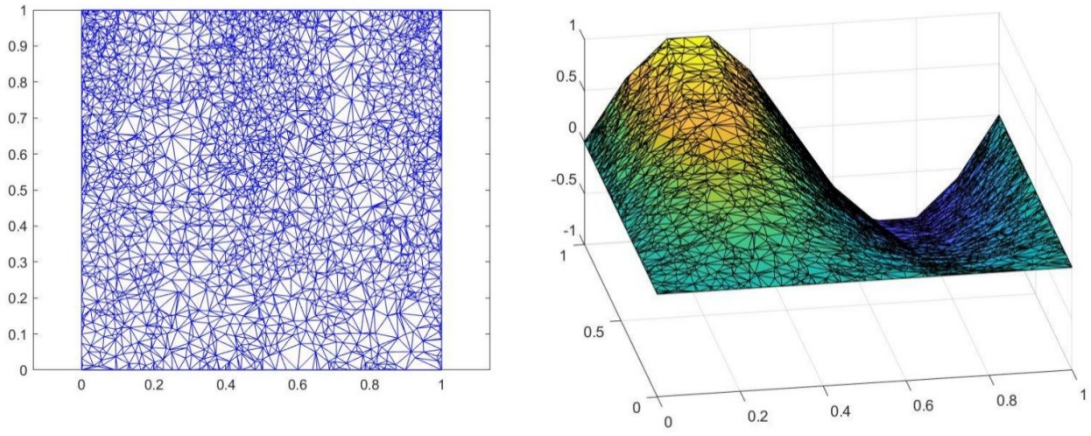

Figure S3.1 The Delaunay triangulation of a surface in R^3: *The triangulation is based on the* $\{\boldsymbol{x}, \boldsymbol{y}\}$ *subspace then lifted to the* $\boldsymbol{z}$ *coordinate. The angles are thus not preserved and the conformal structure is then distorted.*

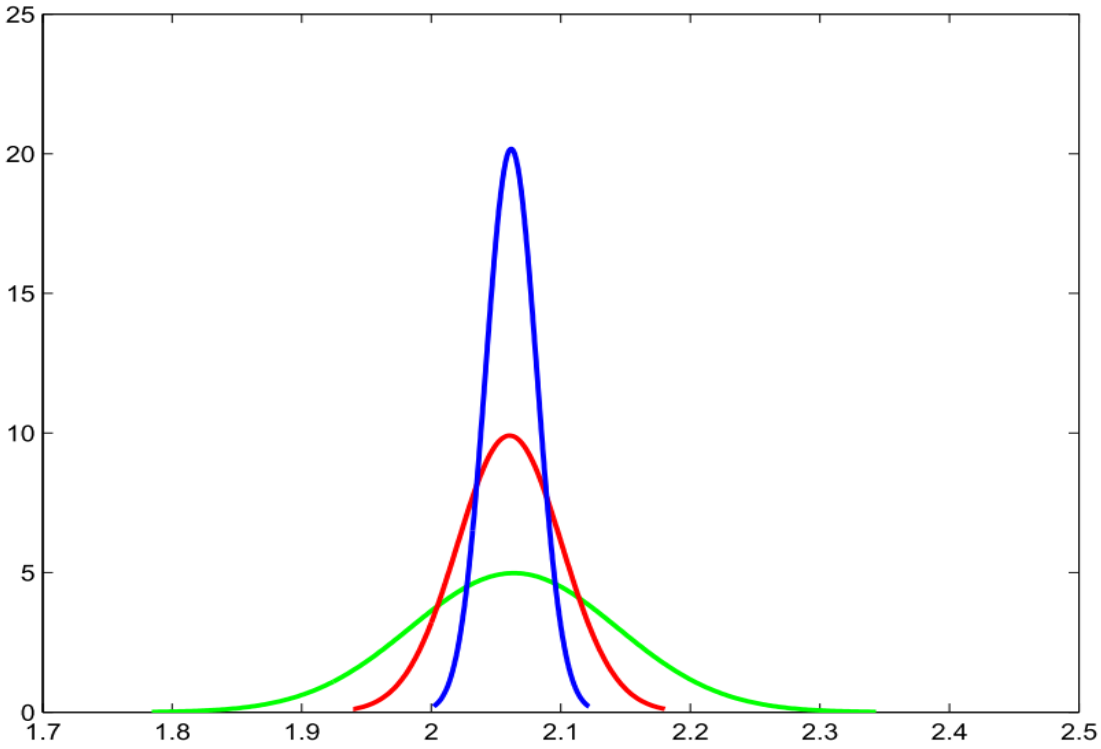

5000 trials with various N for torus of modulus (1+4i)/2:

N	mean (true=2.0616)	variance
200	2.0638	.00642
800	2.0605	.00162
3200	2.0617	.00039

Figure S3.2 Approximation of the extremal length of a torus with increasing *N*: *As N is increased the extremal length approximation converges towards the theoretical value (2.0616) and the variance of trials (upper plot and right column) is reduced.*

While it is impossible to flatten a curve in one map, a theoretical conjecture brought forward by Kenneth Stephenson from University of Tennessee [4] argues that by triangulating the surface randomly a sufficiently high number of times, the conformal structure will emerge from the average triangulation. More specifically, if the surface in R^3 is randomly triangulated N times as $N \to \infty$, the surface is mapped to the conformal rectangle whose extremal length is computed for each $n; n = 1..N$, then the average of the N extremal lengths will converge to

the theoretical continuous case extremal length. Figure S3.2 shows how the computation of extremal length of a torus converges toward the theoretical value as N is increased.

At the time of writing this manuscript, results have only been published in conferences, we refer the reader to the presentation made by [4]. In order to correct the lifting distortion, edge flipping is used. For the conformal structure being conserved during the lifting, the angles of the faces around a node must sum up to $n2\pi$. If that condition is not met, flipping and edge to its dual can correct the problem. For example if $K:\{v1, v2, v3, v4; w_{12}, w_{13}, w_{24}, w_{23}, w_{34}\}$ is a polyhedron with faces $F:\{(v1, v2, v3); (v2, v3, v4)\}$ does not satisfy the $n2\pi$ condition, then flipping edge $w_{23} \rightarrow w_{14}$ will make the new edge a geodesic (thus not contributing to the angle sum) and the surface will stay unchanged. In the present algorithm, the edge flipping is done randomly. For more information on edge flipping we refer the reader to Fisher *et al.*, (2005).

After the random triangulation process is done, we use the circle packing algorithm [6]–[8] to conformally map our surface to the conformal rectangle. Figure S3.3 illustrates the circle packing algorithm. The main principle is the following: If circles of radius $r_i; i \in V:\{v_1..v_n\}$ centered on vertex v_i, with tangency to circles centred on the leaf of v_i (i.e. the vertices connected to v_i by edges), and that the flower of v_i (the triangles that have as common vertex v_i) sums up to $2n\pi$, then there exists a unique collection of radiuses $R:\{r_i..r_n\}$ up to conformal mapping. Thus, by finding a map that preserves R, one can conformal map a Riemannian surface to the conformal rectangle.

In order to assess the performance of our random triangulations→circle packing extremal length approximation, we tested the performance of 3 algorithms on surfaces whose exact extremal length can be computed. The following steps are used for each:

1) Random triangulations → Edge flipping → Circle Packing

2) Regular triangulation → Edge Flipping → Circle Packing

3) Regular triangulation → Edge Flipping → Discrete Natural Conformal Map → Schwarz-Christoffel map.

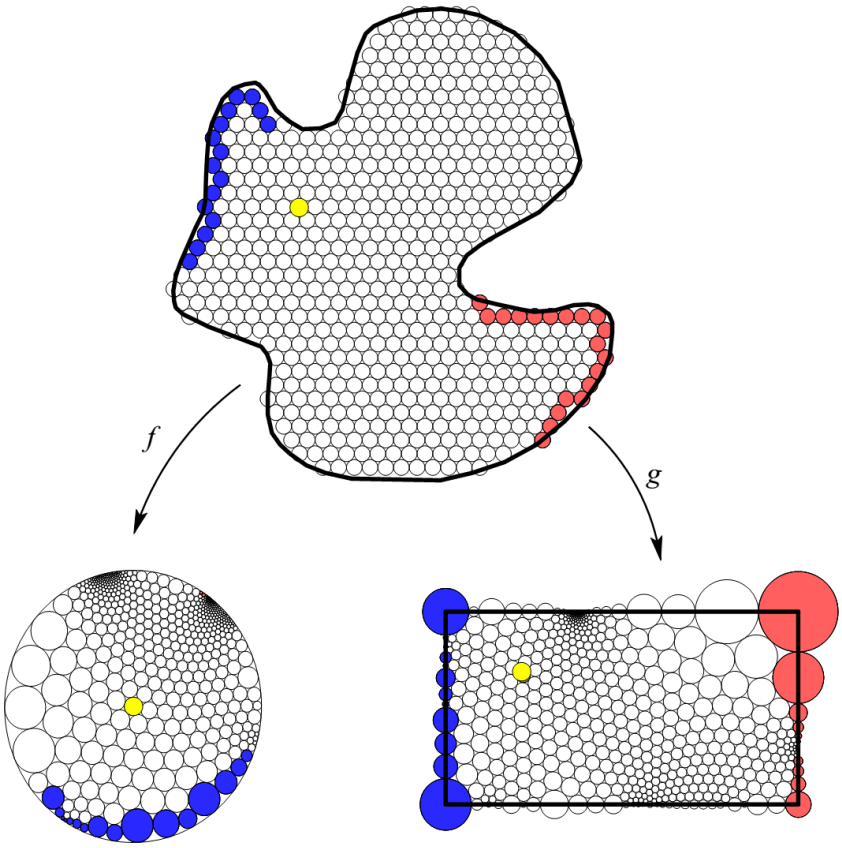

Figure S3.3 The circle packing algorithm: *If a collection of circles of radiuses* $\boldsymbol{R}: \{\boldsymbol{r_i}..\boldsymbol{r_n}\}; \boldsymbol{i} \in \boldsymbol{V}: \{\boldsymbol{v_1}..\boldsymbol{v_n}\}$*, centred on each vertex of the triangulation satisfies that (1) each circle is tangent with circles of neighbouring vertices, (2) the sum of the triangles having a common vertices is* $\boldsymbol{2n\pi}$*, then the collection of circles is unique to conformal mapping. A function* $\boldsymbol{f}, \boldsymbol{g}$ *is a conformal map if it preserves the collection* $\boldsymbol{R}$*.*

The Discrete Natural Conformal Map [9] is variational conformal map from $S \in R^3 \rightarrow S' \in R^2$ that tries to minimize distortion by minimizing the Dirichlet energy necessary to flatten the surface. The resulting S' is of free boundary save for two points whose coordinates in S' are

predetermined prior to the mapping. In order to map S' to the conformal rectangle, we use the Schwarz-Christoffel map [10] that maps the boundary of S' to the conformal rectangle.

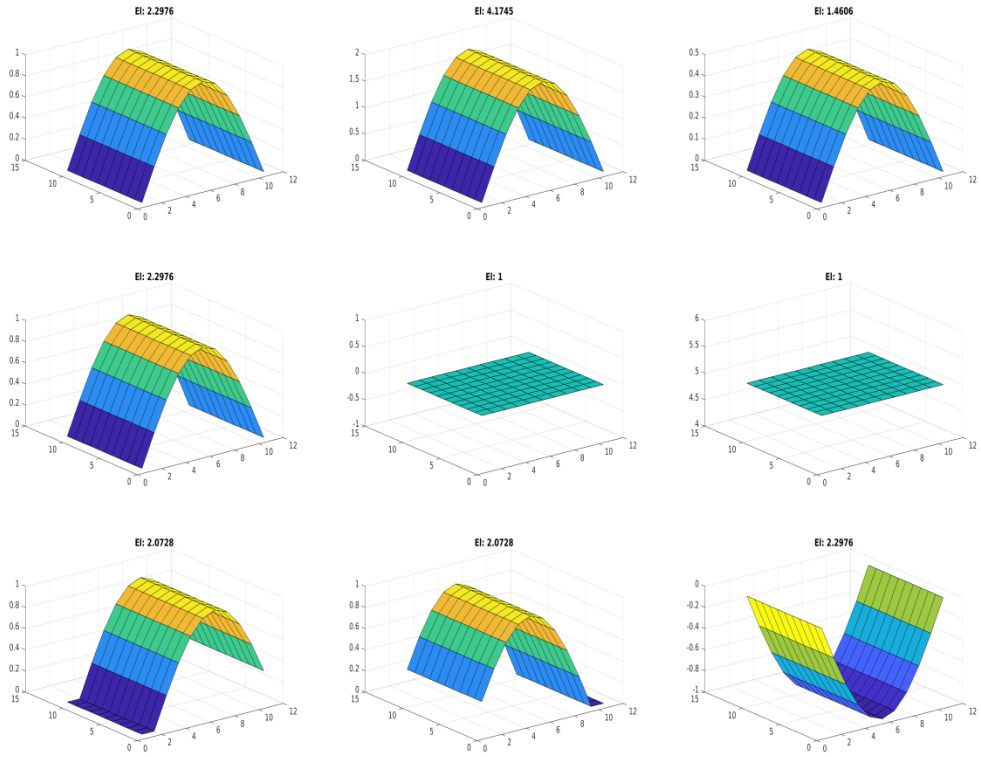

Figure S3.4 Synthetic surfaces used for the performance test of conformal maps: *The theoretical extremal length is displayed on top of each subplot. From top-left to right bottom: (1) Reference surface (RS);(2) RS scaled up;(3) RS scaled down;(4)RS rotated* $\mathbf{180}°$*;(5)Flat surface;(6) Flat surface rotated;(7) RS cropped right;(8) RS cropped left;(9) RS inverted.*

The surfaces tested all have their z coordinates constant along the y dimension. The extremal length of such surfaces is then $\lambda(S) = \frac{\int_L^R ds}{T-B}$ with ds the arc length along x and L, R, T, B as in S1 Figure S3.2. The surfaces are built according to the following: A reference surface has been generated from a sinusoidal function restricted to a single hump. Then several transformations corresponding to conformal automorphisms (i.e. transformations that preserve

the conformal structure) and other that are not conformal are applied and each transformation constitutes a new surface. Figure S3.4 shows the corresponding surfaces.

Global rotations, translations, reflections preserve the extremal length. Figure S3.5 shows the results of the comparative test between the three methods. The figure highlights that only the combination of random triangulations and circle packing gives a correct approximation of the theoretical value for the extremal length of each surface.

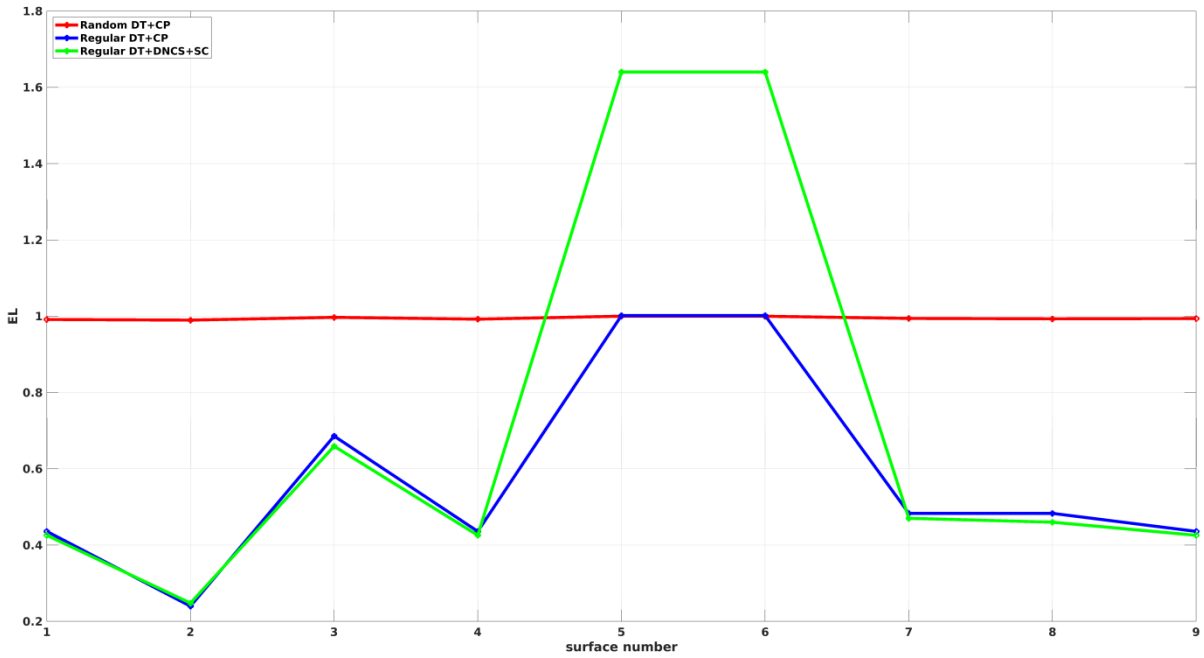

Figure S3.5 Ratio of the synthetic surfaces extremal length approximation using the three methods: *The red curve (our method) is the only one to approximate correctly the theoretical value of extremal length for each surface (i.e.* $\frac{\lambda_{approx}}{\lambda_{theo}} \sim \mathbf{1}$*)*

5. Spatial and temporal filtering of the geopotential height field and extremal length

Climate variability happens on different time and spatial scales. It is common to filter either the time or spatial dimensions to isolate the desired scales. Numerous filtering techniques exist for singling out both spatial and temporal scales (e.g. Lancoz, Fourier, EMD, wavelets and so on). Imagine one can decompose the geopotential height time series into two sub time

series: one has only variability from monthly to annual scales, the other has multi annual to decadal scales. If one sums those two time series, it recovers the original one. A natural question related to extremal length then arises: for each snapshot of both the original and sub time series, does the sum of the sub snapshots extremal length equals the extremal length of the original snapshot?

Question 1 For a surface $S1 = \sum_1^N S_n$, is $\lambda_{S1} = \sum_1^N \lambda_n$ true?

Lemma 4 : the composition principle [2] For a quadrilateral Ω and $\Omega 1..\Omega N \in \Omega$, $\lambda_\Omega \geq \sum_1^N \lambda_{\Omega n}$. Figure S3.6 shows two domains Ω', Ω'' forming the larger $\Omega \cup \mathrm{E}$ with $\Omega' \coloneqq \{w_{E'}; w_E\}, \Omega'' \coloneqq \{w_E; w_{E''}\}$, w_i representing the opposite boundary arcs containing i. The family of curves $\Gamma_{E'E}, \Gamma_{EE''} \in \Gamma_{E'E''}$, hence

$$\lambda_\Omega \geq \sum_1^{N=2} \lambda_{\Omega n} \text{ (1.1)}$$

In order to show whether (1.1) holds, we need to show the proof of the composition principle.

Lemma 5 [2] Choose $\rho = \rho_1 \in \Omega', \rho = \rho_2 \in \Omega'', \rho = \rho \in \Omega \cup E$. Since $\Omega \cup E - \Omega' - \Omega'' = \emptyset$, then $\rho_1 - \rho_2 - \rho = 0$. If in (1.1) we normalize $L(\Gamma_\mathrm{i}, \rho_i) = A(\Omega_i, \rho_i); i = 1..2$, then $L(\Gamma, \rho) \geq L(\Gamma_1, \rho_1) + L(\Gamma_2, \rho_2)$ and $A(\Omega, \rho) = A(\Omega_1, \rho_1) + A(\Omega_2, \rho_2) = L(\Gamma_1, \rho_1) + L(\Gamma_2, \rho_2)$ hence $\lambda_\Omega \geq L(\Gamma_1, \rho_1) + L(\Gamma_2, \rho_2)$ and then

$$\lambda_\Omega \geq \lambda_{\Omega'} + \lambda_{\Omega''} \text{ (1.2)}$$

Lemma 6 It follows from (1.2) that the necessary condition for (1.1) to possibly hold is that $\rho_1 - \rho_2 - \rho = 0$. In the context of the decomposition of a time series (with or without spatial extension), it means all dimensions must be decomposed, the subspaces must be disjoint sets, and their sum must be strictly equal to the original time series. This condition holds for 1-dimensional time series. If a time series of extremal lengths is decomposed into orthogonal time series then, the sum of their extremal length will be equal to the extremal length of the original time series. However, we then time series has a spatial extension, this is

almost never the case. In the context of climate sciences, the spatial time series are decomposed only on the time dimension, the other staying unchanged. Even when decomposing all dimensions, the spatial dimensions usually stay the same, that is, parts of the surface that show no variability are affected a zero value. This breaks the condition that $\rho_1 - \rho_2 - \rho = 0$.

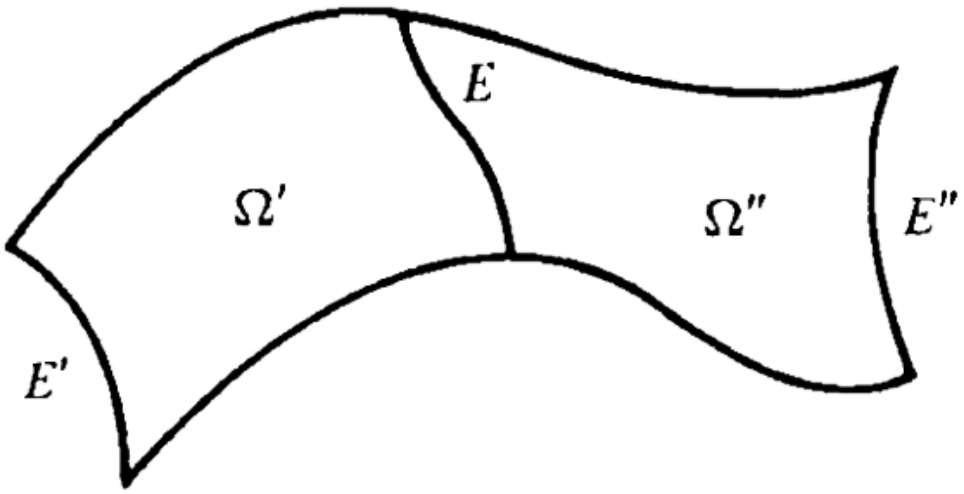

Figure S3.6 The composition principle: The two domains $\boldsymbol{\Omega', \Omega'' \in \Omega \cup E}$ *and disjoint sets. The family of curves in* $\boldsymbol{\Omega', \Gamma_{\Omega'} = \Gamma_{E'E}}$ *is necessarily contained in the family of curves in* $\boldsymbol{\Omega \cup E, \Gamma_{\Omega} = \Gamma_{E'E''}}$. *The same is true for* $\boldsymbol{\Gamma_{\Omega''}}$. *In this context the composition principle states that* $\boldsymbol{\lambda_{\Omega} \geq \lambda_{\Omega'} + \lambda_{\Omega''}}$.

Proposition 7 The computation of the extremal length of an original time series followed by a time decomposition will tell how the dynamics of the original time series change with respect to a given time scale.

Proposition 8 The computation of the extremal length of a time decomposed time series will tell how the decomposed time series dynamics change with respect to that decomposed time series.

References

[1] R. J. Duffin, "The Extremal Length of a Network," *J. Math. Anal. Appl.*, vol. 215, pp. 200–215, 1962.

[2] Lars V. ahlfors, *Conformal invariants*. McGraw-Hill, 1973.

[3] B.Delaunay, "Sur La Sphère Vide," *Bull. l'académie des Sci. l'URSS*, no. 6, pp. 793–800, 1934.

[4] K. Stephenson, "Random Triangulations and Emergent Conformal Structure," in *Computational Conformal Geometry Conference, Stony Brook*, 2007, no. July.

[5] M. Fisher, B. Springborn, P. Schr, and A. I. Bobenko, "An Algorithm for the Construction of Intrinsic Delaunay Triangulations with Applications to Digital Geometry Processing," 2005.

[6] W. Thurston, "The finite Riemann mapping theorem, Invited talk at the International Symposium at Purdue University on the occasion of the proof of the Bieberbach conjecture.," 1985.

[7] B. Rodin and D. Sullivan, "The convergence of circle packings to the Riemann mapping," *J. Differ. Geom.*, vol. 26, no. 2, pp. 349–360, 1987.

[8] K. Stephenson, *Introduction to Circle Packing: The Theory of Discrete Analytic Functions*. Cambridge university press, 2005.

[9] M. Desbrun, M. Meyer, and P. Alliez, "Intrinsic parameterizations of surface meshes," *Comput. Graph. Forum*, vol. 21, no. 3, pp. 209–218, 2002.

[10] T. A. Driscoll and L. N. Trefethen, “Schwarz-Christoffel mapping,” *Comput. Math. with Appl.*, vol. 46, no. 2–3, p. 513, 2003.